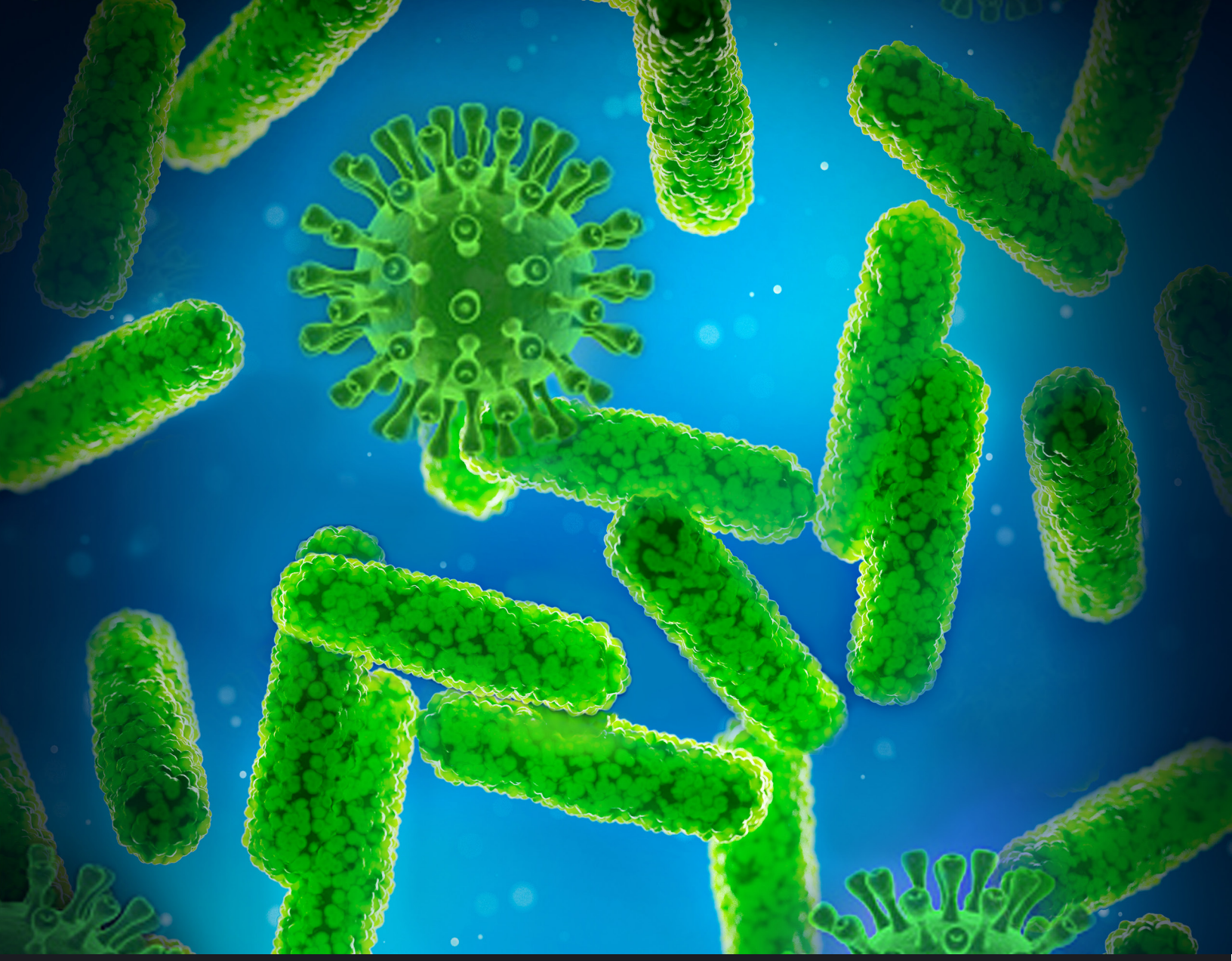

Advanced Flow Cytometry for Infectious Diseases

ARTICLE COLLECTION

WILEY

CURRENT PROTOCOLS
A Wiley Brand

Cytometry PART A
ISAC
Journal of Quantitative Cell Science

Sponsored by:
BIO-RAD

Brighter *insights* into diseases,

with multiparameter flow cytometry and StarBright Dyes.

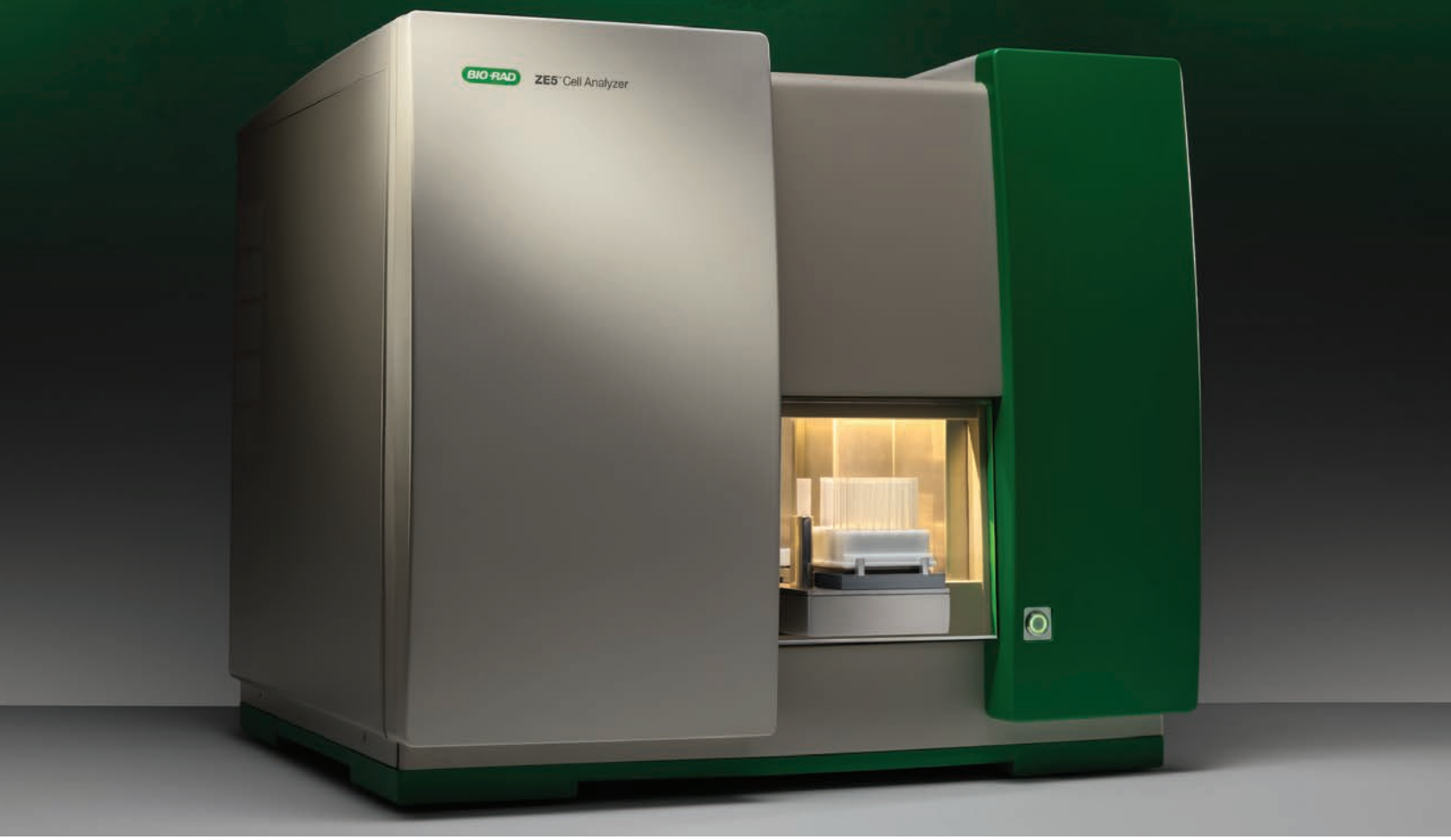

Accurately detect your infectious disease model

The ZE5 Cell Analyzer can detect down to 0.2 µm in cell size, can run at 100,000 events per second with washes and low carryover, and it has an established publication catalog in infectious diseases. Advance your research with the ZE5 Cell Analyzer, infectious disease antibody portfolio, and newly launched, exceptionally bright StarBright Dyes, which allow you to separate negative from positive, even for rare and dim populations.

To learn more, visit bio-rad.com/cellanalysis

#ScienceForward

BIO-RAD

Contents

4
Introduction

5
Flow Cytometry: An Overview
BY KATHERINE M. MCKINNON
Current Protocols in Immunology

16
Adapting to the Coronavirus Pandemic: Building and Incorporating a Diagnostic Pipeline in a Shared Resource Laboratory
BY EMMA RUSSELL, ANA AGUA-DOCE, LOTTE CARR, ASHA MALLA, KEROL BARTOLOVIC, DINA LEVI, CARL HENDERSON, DEBIPRIYA DAS, HEFIN RHYS, PHILIP HOBSON, SUKHVEER PUREWAL, ANDREW RIDDELL
Cytometry Part A

26
A Mouse Model of Sublethal Leptospirosis: Protocols for Infection with *Leptospira* Through Natural Transmission Routes, for Monitoring Clinical and Molecular Scores of Disease, and for Evaluation of the Host Immune Response
BY NISHA NAIR AND MARIA GOMES-SOLECKI
Current Protocols in Microbiology

50
CD4+ T Cell Activation and Associated Susceptibility to Hiv-1 Infection in vitro Increased Following Acute Resistance Exercise in Human Subjects
BY ALEXANDER K. HOLBROOK, HUNTER D. PETERSON, SAMANTHA A. BIANCHI, BRAD W. MACDONALD, ERIC C. BREDAHL, MICHAEL BELSHAN & JACOB A. SIEDLIK
Physiological Reports

62
Modularly Programmable Nanoparticle Vaccine Based on Polyethyleneimine for Personalized Cancer Immunotherapy
BY JUTAEK NAM, SEJIN SON, KYUNG SOO PARK, AND JAMES J. MOON
Advanced Science

Introduction

Few technologies are more central to the investigation of and therapeutic development for infectious diseases than flow cytometry. Capable of identifying and characterizing single cells based on cellular markers, this technology is critical to understanding immune responses to infection from pathogens and the pathology of cancer. Further, the development of therapeutics to infections such as SARS-CoV-2 or personalized medicine approaches to cancer treatment benefit from this foundational technology. This collection of articles presents a sampling of studies utilizing flow cytometry to better understand infectious diseases and develop diagnostic and therapeutic interventions.

First, McKinnon (2018) provides an in-depth overview of the flow cytometry technologies available to researchers. They discuss the different modalities of flow cytometry as well as their potential applications to answering research questions. Next, Russell et al. (2020) describes the process of designing a clinical diagnostic laboratory for SARS-CoV-2 testing at The Francis Crick Institute's Flow Cytometry Science Technology Platform. This includes an accounting of factors, such as COVID-19 restrictions, that impacted the development of a functional diagnostic pipeline and SARS-CoV-2 assay development. Continuing, Nair and Gomes-Solecki (2020) describe protocols for bacterial infection of mouse models with *Leptospira* to recapitulate disease progression and physiologically relevant transmission routes. They also discuss protocols for evaluating clinical, molecular, and histological scores, as well as flow cytometry based-analysis of the host-immune response. Moving to human studies, Holbrook et al. (2019) used flow cytometry to examine the effects of acute resistance exercise on CD4+ T lymphocyte activation and replication (susceptibility) of HIV-1. They were able to demonstrate that acute bouts of resistance exercise increased the activation state of CD4+ T lymphocytes, lead to an increase in infection susceptibility and the potential for this measure to quantify exercise-induced changes in immune function. Lastly, personalized treatments such as cancer vaccines holds great therapeutic potential. One emerging technology for this area is programmable nanoparticle vaccines. Polyethyleneimine (PEI)-based nanoparticle vaccines have been studied for the treatment of numerous infectious diseases previously. In Nam et al. (2021), they explore the potential of modularly programmed PEI-based nanoparticle vaccines for personalized cancer immunotherapy. To characterize the uptake of the nanoparticles, tumor tissues were processed via flow cytometry for the intracellular concentration of nanoparticle as well as the activation state of tumor-draining lymph nodes. They report that optimized nanovaccines were highly effective at priming of antigen-specific CD8+ T-cells with antitumor efficacy, illustrating their therapeutic potential.

By introducing readers to the advantages of flow cytometry for diagnostic development and research into infectious disease, we hope to empower users to investigate the use of this technology to address their specific research or diagnostic goals. For more information and resources for flow cytometry, we encourage you to visit the Bio-Rad ZE5 Cell Analyzer product page and explore the resources provided there.

By Jeremy Petravicz, PhD, Editor,
Current Protocols

References

McKinnon, K. M. (2018). Flow cytometry: An overview. *Current Protocols in Immunology,* 120, 5.1.1–5.1.11. https://doi.org/10.1002/cpim.40

Russell, E., et al (2021). Adapting to the Coronavirus Pandemic: Building and Incorporating a Diagnostic Pipeline in a Shared Resource Laboratory. *Cytometry*, 99: 90-99. https://doi.org/10.1002/cyto.a.24248

Nair, N., & Gomes-Solecki, M. (2020). A mouse model of sublethal leptospirosis: Protocols for infection with Leptospira through natural transmission routes, for monitoring clinical and molecular scores of disease, and for evaluation of the host immune Response. *Current Protocols in Microbiology,* 59, e127. https://doi.org/10.1002/cpmc.127

Holbrook, A. K., et al (2019). CD4+ T cell activation and associated susceptibility to HIV-1 infection in vitro increased following acute resistance exercise in human subjects. *Physiol Rep*, 7 (18), e14234, https://doi.org/10.14814/phy2.14234

Nam, J., et al (2021). Modularly Programmable Nanoparticle Vaccine Based on Polyethyleneimine for Personalized Cancer Immunotherapy. *Adv. Sci.*, 8, 2002577. https://doi.org/10.1002/advs.202002577

Flow Cytometry: An Overview

Katherine M. McKinnon[1]

[1]Vaccine Branch, National Cancer Institute, National Institutes of Health, Bethesda, Maryland

Flow cytometry is a technology that provides rapid multi-parametric analysis of single cells in solution. Flow cytometers utilize lasers as light sources to produce both scattered and fluorescent light signals that are read by detectors such as photodiodes or photomultiplier tubes. These light signals are converted into electronic signals that are analyzed by a computer and written to a standardized format (.fcs) data file. Cell populations can be analyzed and/or purified based on their fluorescent or light scattering characteristics. A variety of fluorescent reagents are utilized in flow cytometry. These include fluorescently conjugated antibodies, nucleic acid binding dyes, viability dyes, ion indicator dyes, and fluorescent expression proteins. Flow cytometry is a powerful tool that has applications in immunology, molecular biology, bacteriology, virology, cancer biology, and infectious disease monitoring. It has seen dramatic advances over the last 30 years, allowing unprecedented detail in studies of the immune system and other areas of cell biology. © 2018 by John Wiley & Sons, Inc.

Keywords: flow cytometry • fluorescence • reagents • light scatter

INTRODUCTION

Flow cytometry is a technology that rapidly analyzes single cells or particles suspended in a buffered salt-based solution as they flow past single or multiple lasers. Each particle is analyzed for visible light scatter and one or multiple fluorescence parameters. Visible light scatter is measured in two different directions, the forward direction (forward scatter, FSC) which can indicate the relative size of the cell and at 90° (side scatter, SSC) which indicates the internal complexity or granularity of the cell. Light scatter is independent of fluorescence. Samples are prepared for fluorescence measurement through transfection and expression of fluorescent proteins (ex. green fluorescent protein, GFP), staining with fluorescent dyes (e.g., propidium iodide, which labels nucleic acids such as DNA) or immunostaining with fluorescently conjugated antibodies (e.g., CD3 antibody conjugated to fluorescein isothiocyanate, FITC).

Flow cytometry is a powerful tool with applications in multiple disciplines such as immunology, virology, molecular biology, cancer biology, and infectious disease monitoring. For example, it is very effective for the study of the immune system and the immune response to infectious diseases and cancer. It allows for the simultaneous characterization of mixed populations of cells from blood and bone marrow as well as solid tissues that can be dissociated into single cells such as lymph nodes, spleen, mucosal tissues, solid tumors, etc. In addition to analysis of populations of cells, a major application of flow cytometry is sorting cells into uniform populations to be used for further downstream analysis. A more detailed look at applications will be discussed later in this unit.

The instrumentation used for flow cytometry has evolved over the last several decades. Multiple laser systems are common as are instruments designed for specific purposes, such as systems with 96-well loaders for bead analysis, systems that combine microscopy and flow cytometry, and systems that combine mass spectrometry and flow cytometry. An overview of current instrumentation platforms will be covered in this unit.

Current Protocols in Immunology 5.1.1–5.1.11, February 2018
Published online February 2018 in Wiley Online Library (wileyonlinelibrary.com).
doi: 10.1002/cpim.40

The increase in available reagents over the last several years has led to explosive growth in the number of parameters used in flow cytometry experiments. There has been a dramatic increase in fluorochromes that can be conjugated to monoclonal antibodies, such as tandem dyes and polymer dyes. In addition, there has been an increase in available fluorescent proteins beyond GFP that can be used for transfection, such as mCherry, mBanana, mOrange, mNeptune, etc. These advances in fluorochromes and instrumentation has led to experiments with the possibility of 30+ parameters.

Finally, data analysis has been expanded to evaluate the additional information available from the new instrumentation and reagents. Traditional two parameter histogram (dot plot) gating and analysis is still being used frequently. However, the increase in number of parameters and complexity in experiments is leading to the use of newer cluster data analysis algorithms such a principal component analysis (PCA), spanning-tree progression analysis of density-normalized events (SPADE), and t-stochastic neighbour embedding (tSNE). These improved methods of data mining allow useful information to be extracted from the high-dimensional data now available from flow cytometry.

INSTRUMENTATION

Traditional Flow Cytometers

Traditional flow cytometers consist of three systems: fluidics, optics, and electronics. The fluidics system consists of sheath fluid (usually a buffered saline solution) that is pressurized to deliver and focus the sample to the laser intercept or interrogation point where the sample is analyzed. The optical system consists of excitation optics (lasers) and collection optics (photomultiplier tubes or PMTs and photodiodes) that generate the visible and fluorescent light signals used to analyze the sample. A series of dichroic filters steer the fluorescent light to specific detectors and bandpass filters determine the wavelengths of light that are read so that each individual fluorochrome can be detected and measured. More specifically, dichroic filters are filters that pass light through that is either shorter or longer in wavelength and reflect the remaining light at an angle. For example, a 450 dichroic long pass (DLP) filter lets light with a wavelength longer than 450 nm through the filter and bounces the shorter wavelengths of light off at an angle to be sent to another detector. Bandpass filters detect a small window of a specific wavelength of light. For example, a 450/50 bandpass filter passes fluorescent light with a wavelength of 450 nm $\pm$ 25 nm through the filter to be read by the detector. The electronic system converts the signals from the detectors into digital signals that can be read by a computer.

Multiple laser systems are common with instruments often having 20 parameters (e.g. FSC, SSC, and 18 fluorescent detectors). There are new instrument platforms being introduced with five or more lasers and 30-50 parameters, but these are less common. The most common lasers used in traditional flow cytometers are 488 nm (blue), 405 nm (violet), 532 nm (green), 552 nm (green), 561 nm (green-yellow), 640 nm (red) and 355 nm (ultraviolet). Additional laser wavelengths are available for specialized applications. In addition, there are instruments that have replaced PMTs with avalanche photodiodes (APD) for fluorescence detection, with the aim of increasing sensitivity.

Acoustic Focusing Cytometers

This cytometer uses ultrasonic waves to better focus cells for laser interrogation. This type of acoustic focusing allows for higher sample input and less sample clogging. This cytometer can utilize up to 4 lasers and 14 fluorescence channels.

Cell Sorters

A specific type of traditional flow cytometer is the cell sorter which can purify and collect samples for further analysis. A cell sorter allows the user to select (gate) a population of cells or particles which is positive (or negative) for the desired parameters and then direct those cells into a collection vessel. The cell sorter separates cells by oscillating the sample stream of liquid at a high frequency to generate drops. The drops are then given either a positive or negative charge and passed through metal deflection plates where they are directed to a specific collection vessel based on their charge. The collection vessels can be tubes, slides or plates (96-well or 384-well are common).

There are two types of cell sorters, quartz cuvette and "jet-in-air", that differ in where the laser interrogation point is located. The quartz cuvette cell sorters have fixed laser alignment and are easier to prepare for a sort. The "jet in air" cell sorters need to have the lasers aligned daily and are more difficult to set up but are more adaptable for small particle detection.

Imaging Cytometers

Imaging flow cytometers (IFC) combine traditional flow cytometry with fluorescence microscopy. This allows for rapid analysis of a sample for morphology and multi-parameter fluorescence at both a single cell and population level (Barteneva, Fasler-Kan, & Vorobjev, 2012). IFC can track protein distributions within individual cells like a confocal or fluorescence microscope but is also able to process large numbers of cells like a flow cytometer. They are particularly useful in multiple applications such as cell signaling, co-localization studies, cell to cell interactions, DNA damage and repair, and any application that needs to be able to coordinate cellular location with fluorescence expression in large populations of cells.

Mass Cytometers

Mass cytometers combine time-of-flight mass spectrometry and flow cytometry. Cells are labeled with heavy metal ion-tagged antibodies (usually from the lanthanide series) instead of fluorescently-tagged antibodies and detected using time-of-flight mass spectrometry. Mass cytometers do not have FSC or SSC light detection, and therefore do not allow for the conventional method of detecting cell aggregates. However other methods such as cell barcoding can be employed for this purpose (Leipold, Newell, & Maecker, 2015). Also, mass cytometry does not have cellular autofluorescence signals and reagents do not have the emission spectral overlap associated with fluorescent labels so compensation is not needed. However, the sample is destroyed during analysis so cell sorting is not possible, and the acquisition rate is much lower than a standard flow cytometer (1000 cells/second instead of 10,000 cells/second). Currently, there are commercially available reagents for 40 channels but this number will increase with the introduction of other metal ions such as platinum for conjugation to antibodies (Mei, Leipold, & Maecker, 2016).

Cytometers for Bead Array Analysis

Multiplex bead arrays have become popular for analyzing large amounts of analytes in small sample volumes. Briefly, these assays utilize capture beads with a known amount of fluorescence in a specific channel and a reporter molecule detected by a separate laser to quantify the amount of captured analyte associated with the specific bead. It is essentially the equivalent of 100 ELISA assays.

Small flow cytometers with usually 2 lasers and 96-well loaders have been developed to analyze these assays. These instruments have small footprints and optical bench designs that are optimized to detect and discriminate beads with different amounts of fluorescence along two channels. Instruments have been developed that can detect 100-500 different bead combinations.

Spectral Analyzers

One of the challenges of multi-parameter flow cytometry is compensation (erasing spectral overlap) between flurochromes. A new type of flow cytometer, the spectral analyzer is specifically designed to address this problem. A spectral analyzer measures the entire fluorescent emission spectra for each fluorochrome in a multicolor sample to create a spectral fingerprint. Then during analysis, each spectra is unmixed to provide a pure signal for each fluorochrome (Sony, 2017). Spectral analysis is starting to replace traditional PMTs as a detection method for high-dimensional flow cytometry.

New Detector Technologies

Photomultiplier tubes (PMTs) remain the standard detector technology for flow cytometry. Their high sensitivity and low backgrounds make them useful for fluorescence technology. However, solid state detectors are starting to appear in some cytometers. Avalanche photodiodes (APDs) are inexpensive, sensitive and highly linear, and are more spectrally responsive in the long red region. Silicon photodiodes (SiPDs) are also a promising option for solid state detectors.

REAGENTS

Small Organic Molecules

Small organic molecules such as fluoroscein (MW=389 Da), Alexa Fluor 488 (fluorescein analog, MW=643 Da), Texas Red (TxRed, MW=625 Da), Alexa Fluor 647 (MW=1155 Da), Pacific Blue (MW=242 Da), and Cy5 (MW=762 Da) are commonly used for antibody conjugation. These have consistent emission spectra and a small Stokes shift (the difference between excitation wavelength and emission wavelength, approximately 50-100 nm). These are also stable and reasonably easy to conjugate to antibodies. The Alexa Fluor (Thermo Fisher) dyes were designed to be more resistant to photobleaching and are better reagent choices for samples that will also be used for imaging.

Phycobiliproteins

Phycobiliproteins are large protein molecules derived from cyanobacteria, dinoflagellates, and algae. These are large molecules, for example phycoerythrin (PE) has a molecular weight of 240,000 Da. These proteins have large Stokes shifts (75-200 nm) and are very stable with consistent emission spectra. Because of their large size, phycobiliproteins are excellent for quantitative flow cytometry since they usually have a 1:1 protein to fluorochrome ratio during conjugation. However, phycobiliproteins are susceptible to photobleaching and are not recommended for applications with long or repeated exposure to excitation sources. Examples of phycobilibroteins are phycoerythrin (PE), allophycocyanin (APC), and peridinin chlorophyll protein (PerCP).

Quantum Dots

Quantum Dots (Qdots) are semiconductor nanocrystals that have tight fluorescence emission spectra associated with the size of the nanocrystal. They are optimally excited with UV or violet lasers but can be minimally excited by multiple lasers. This minimal excitation complicates fluorescence compensation when Qdots are used in multi-parameter experiments. Because of the compensation issues and difficulty in conjugating Qdots to antibodies, these reagents have largely been replaced with the polymer dyes in multi-parameter staining panels.

Polymer Dyes

Polymer dyes consist of polymer chains that collect light signals and can be "tuned" to absorb and emit light at specific wavelengths based on the length of the polymer chain and the attached molecular subunits. These dyes are very stable and have similar quantum efficiency to phycobiliproteins with greatly increased photostability. Since polymer dyes can be made to absorb light only at specific wavelengths, they avoid the issues with multiple laser excitation that make Qdot reagents difficult to use in multi-parameter experiments. Examples of these reagents are the Brilliant Violet (BV), Brilliant Ultraviolet (BUV) and Brilliant Blue (BB) reagents.

Tandem Dyes

Tandem dyes chemically couple either phycobiliproteins (PE, APC, PerCP) or polymers dyes (BV421, BUV395) with small organic fluorochromes (Cy3, Cy5, Cy7) to create a dye that uses fluorescence energy transfer (FRET) to increase the available fluorochromes that can be excited with a single laser source. For example, Texas Red has a maximum excitation of 589 nm, and PE has an emission of 585 nm, so by coupling PE to Texas Red, the emission from PE is used to excite Texas Red through FRET, allowing PE-TxRed to be excited by either a 488 nm or 532 nm laser. The polymer chain antibodies use the same method to increase available fluorochromes that can be excited by a single laser. Tandem dyes are extremely bright with large Stokes shift values (150-300 nm) which is useful when dealing with low antigen density. However, tandem dyes are less stable than the donor fluorochromes and can differ from lot to lot in their energy transfer efficiency, complicating compensation. Most of the longer Brilliant polymer dyes are also tandems and share these issues.

Metal Conjugates for Mass Cytometry

Antibodies for use in mass cytometry are conjugated to single isotope heavy metal ions in the lanthanide series of elements. There are currently 35 lanthanide series isotopes commercially available for antibody conjugation. These probes are non-fluorescent and only applicable for mass cytometry. Additional antibody conjugates will become available as soon as other metal elements are evaluated for suitability with this platform.

Fluorescent Proteins

Fluorescent proteins are frequently used as reporter systems for gene expression. The most commonly used is green fluorescent protein (GFP) derived from the jellyfish *Aequorea victoria* (Tsien, 1998). GFP was cloned to generate cyan fluorescent protein (CFP) and yellow fluorescent protein (YFP). Red fluorescent protein (DsRed) was derived from the mushroom anemone, *Discosoma* (Mikhail V. Matz, 1999) and then cloned for use in protein expression systems. Next generation monomeric fluorescent proteins (mCherry, mBanana) were cloned from DsRed and have broader excitation and emission spectra. The violet and green/yellow excited fluorescent proteins see especially heavy use in flow cytometry. New fluorescent proteins are continuously being discovered and generated; currently, several hundred exist, with excitation and emission spectra ranging from the ultraviolet to near infrared. The presence of many laser wavelengths on modern flow cytometers has dramatically expanded the use of fluorescent proteins in flow cytometry.

Nucleic Acid Dyes

Nucleic acid dyes bind DNA, RNA, or both. These are used to quantitate DNA for cell cycle analysis (Propidium Iodide, 7-aminoactinomycin D or 7AAD, DyeCycle Violet, 4',6-diamidino-2-phenylindole or DAPI), discriminate chromosomes for sorting (Hoescht 33342, Chromomycin A3), sorting stem cells using side population analysis (Hoescht 33342), cell viability analysis, and for sorting bacteria. They can be combined with another marker such as fluorochrome conjugated anti-bromodeoxyuridine (BrdU) to determine proliferation.

Proliferation Dyes

Cell proliferation can be measured by pulsing cells with BrdU (bromodeoxyuridine) and then staining with an antibody against BrdU and a DNA dye. However, this method does not allow for long term proliferation studies. Carboxyfluoroscein succinimidly ester (CFSE) and other similar dyes can be used to follow multiple divisions of proliferating cells. Red and violet excited variants of these dyes are also now available. Each cell is permanently labeled with the dye and the subsequent generations of cells inherit lower amounts of the dye due to the dilution of the dye. These dyes do not affect cell growth or morphology and are suitable for long term proliferation studies.

Viability Dyes

Cell viability can be measured through exclusion of dyes (Propidium iodide, DAPI) or by the binding of a dye to amines within a cell to determine if the cell membrane is intact. The exclusion dyes cannot be fixed and are only suitable for cells that are not infectious and will be analyzed immediately. Amine binding dyes such as the Live/Dead reagents (ThermoFisher), Zombie dyes (Biolegend) or Fixable Viablity dyes (BD Biosciences) can be fixed and used for cells that are infectious, cells that need to be stained for internal antigens, and cells that need to be stored prior to acquisition.

Calcium Indicator Dyes

Calcium indicator dyes undergo a color shift upon binding to calcium. They are used to indicate cell activation and signaling. The data is expressed as a ratio of the two wavelengths associated with bound and unbound calcium and dye. The most commonly used dye remains indo-1, an ultraviolet biphasic calcium probe. Blue-green calcium probes including fluo-3 are also available.

APPLICATIONS

Flow cytometry has a wealth of techniques and applications suitable for multiple fields of study. In this section, applications are broadly grouped under specific disciplines; however, any of these techniques can be used in all fields of study.

Immunology

Immunophenotyping

Flow cytometry is most commonly used for immunophenotyping. This application utilizes the unique ability of flow cytometry to simultaneously analyze mixed populations of immune cells for multiple parameters. In its simplest form, an immunophenotyping experiment consists of cells stained with fluorochrome-conjugated antibodies that are targeted against antigens on the cell surface. Most of these antigens are given "cluster of differentiation" numbers or CD numbers by the Human Leukocyte Differentiation Workshops so that a common nomenclature is used to define monoclonal antibodies that are directed against specific cellular antigens. For example, CD3 is "cluster of differentiation number 3" and is used to define the T cell co-receptor that is present on all T cells.

Most immune cells have specific CD markers that define them as a population of cells. These cell markers are called lineage markers and are used to define specific cell populations for additional analysis in each immunophenotyping experiment. Examples are the T cell markers (CD3, CD4, CD8), B cell markers (CD19, CD20), monocyte markers (CD14, CD11b) and natural killer (NK) cell markers (CD56, CD161).

In addition to lineage markers that define populations of immune cells, other markers are used to characterize each cell population. These markers can include activation markers (CD69, CD25, CD62L), memory markers (CD45RO, CD27), tissue homing markers ($\alpha 4/\beta 7$) and chemokine receptor markers (CCR7, CCR5, CXCR4, CCR6). Often, immunophenotyping experiments also include intracellular markers such as FoxP3 (defines T_{reg} cells), cytokines (IFN-γ, TNF-α, IL-2 define T_H1 cells), proliferation markers (Ki67, CFSE), and antigen specific markers (major histocompatibility or MHC Tetramers). Current instruments and reagents are capable of 28 color immunophenotyping experiments, although it is more common to have experiments in the 12-15 color range. A

Table 5.1.1 Example of a 15-Color T_{reg} Cell Staining Panel

Laser	Dichroic filter	Bandpass filter	Fluorochromes
488 nm	505LP	525/50	CD14 FITC
488 nm	690LP	710/50	CD4 PerCP-Cy5.5
532 nm		575/26	CD127 PE
532 nm	600LP	610/20	TGF-B1 PE-CF594
532 nm	635LP	660/20	HLA-DR PE-Cy5
532 nm	685LP	710/50	
532 nm	755LP	780/60	CD73 PE-Cy7
628 nm		670/30	CD25 APC
628 nm	685LP	730/45	CD3 Ax700
628 nm	755LP	780/60	CD20 APC-Cy7
405 nm		450/50	FoxP3 BV421
405 nm	505LP	525/50	Live/Dead Aqua Dye
405 nm	557LP	560/20	
405 nm	570LP	585/42	
405 nm	600LP	610/20	CD39 BV605
405 nm	635LP	670/30	CD8 BV650
405 nm	690LP	710/50	IL-10 BV711
405 nm	750LP	780/60	CD45 BV786

sample 15-color T_{reg} cell immunophenotyping panel is shown in Table 5.1.1.

Antigen specific responses

Antigen specific responses can be measured by stimulating immune cells with a specific antigen and then looking for cytokine production, proliferation, activation, memory, or antigen recognition through MHC multimers. MHC multimers are MHC monomers (MHC-I or MHC-II) that are usually biotinylated and then bound to a fluorescent streptavidin backbone in groups of 4 (tetramer), 5 (pentamer) or 10 (dextramer). These MHC multimers are "loaded" with the antigen of choice and then used to bind to T cells that recognize the antigen, thus indicating the level of response to a specific antigen. This application is commonly used in vaccine studies.

Intracellular cytokine analysis

Intracellular cytokine analysis is performed by treating immune cells with a protein transport inhibitor (Brefeldin A or Monensin) for 2 to 12 hours to allow for cytokines produced by the cells to accumulate within the cell, enabling better detection. Cells can be stimulated with various antigens during this incubation, such as peptides from a vaccine, to measure immune response.

Following protein transport inhibitor treatment, cells are stained for viability markers and cell surface markers, then fixed and permeabilized for intracellular staining with anti-cytokine antibodies.

Proliferation analysis

Cell proliferation can be measured by flow cytometry using several different assays and markers. These assays use different methods to target proliferation-related events such as incorporation of thymidine analogs (BrdU) into replicating DNA, generational tracking of inheritable permanent dyes (CFSE), and expression of proliferation related antigens (Ki67, PCNA).

The flow cytometry equivalent of the ^{3}H thymidine proliferation assay utilizes the thymidine analogs BrdU or EdU (ethynyl deoxyuridine) to pulse growing cells for 2 to 6 hours. Following this incubation, the cells are stained for surface markers (optional) and then fixed and permeabilized for staining the incorporated BrdU or EdU. The BrdU procedure utilizes DNase to exposed the BrdU for antibody staining, but the EdU procedure

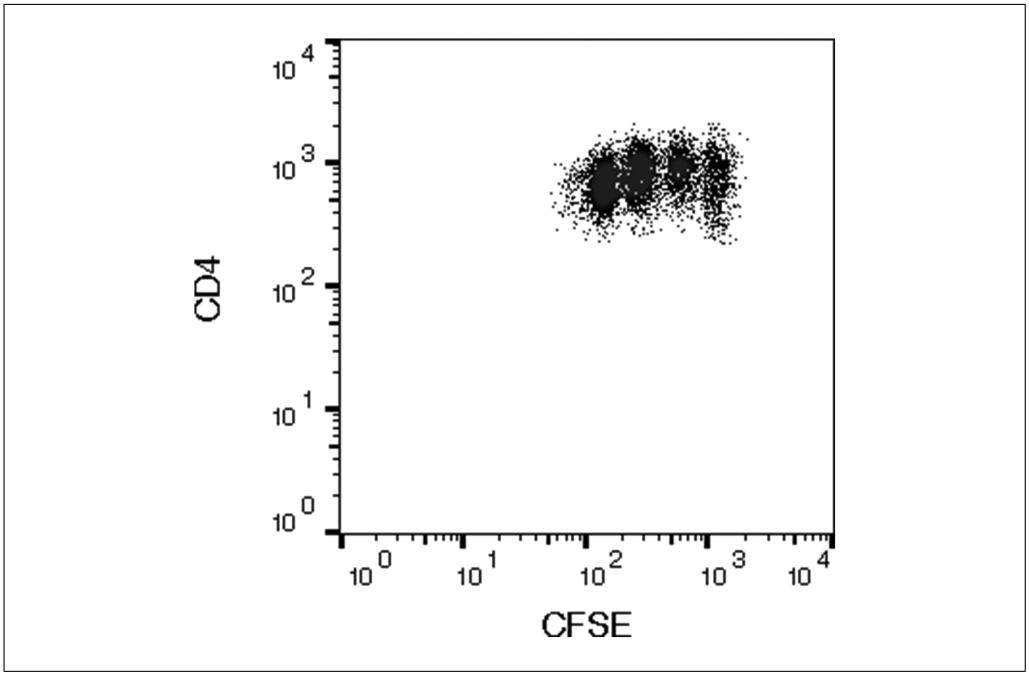

Figure 5.1.1 Example of CFSE staining used for proliferation analysis. Human CD4+ T cells were stained with CFSE and then stimulated for 5 days with an antigen. Each peak of CFSE staining represents one generation of cell division.

utilizes a copper catalyzed click chemistry to detect the EdU. Both methods are usually counterstained with a DNA-binding dye like propidium iodide. In addition, both the BrdU and EdU method are compatible with staining for additional intracellular antigen markers.

CFSE and other similar dyes (CellTrace Violet, FarRed, etc) cross the cellular membrane in living cells and bind covalently and permanently to intracellular structures (usually to lysine residues or other amines). The daughter cells of each subsequent generation inherit the dye allowing for long term analysis of proliferation. This technique is very useful when following proliferation resulting from long-term antigen stimulation. An example of CFSE staining is shown in Figure 5.1.1.

Expression of proliferation-related antigens can also be used as a marker for proliferation. Ki67 is a protein expressed during all phases of cell proliferation but not during cell quiescence. Proliferating cell nuclear antigen (PCNA) is required for DNA replication. The presence of either Ki67 or PCNA is an indicator of cell proliferation. Ki67, PCNA, and BrdU staining in the same cells is shown in Figure 5.1.2.

Apoptosis analysis

Apoptosis, or programed cell death, is a phenomenon that is frequently examined in immunology and other fields of study. It is used by the immune system to maintain the homeostasis by removing cells without triggering an inflammatory response. This is in contrast to necrosis, a type of cell death that does trigger an inflammatory response. Apoptosis is the mechanism of cell death for clonally expanded T cells following an immune response, for self-targeting T cells, for autoreactive B cells, and multiple other cells in the immune system.

The detection of apoptosis by flow cytometry utilizes multiple targets along the cascade of apoptosis-associated events. The translocation of phosphatidylserine to the outer layer of the plasma membrane is detected by Annexin V staining, the endonuclease digestion of DNA is detected by the TUNEL (TdT dUTP Nick End Labeling) assay, and the activation of Caspases can be detected by antibodies and dyes, mitochondrial apoptosis is targeted by dyes that determine mitochondrial membrane potential and chromatin condensation in the nucleus detected by staining with Hoescht 33342.

Annexin V is a phospholipid binding protein that binds to phosphatidylserine when it is translocated to the outer layer of the cellular membrane during apoptosis. A viability exclusion dye (like propidium iodide) should be used when staining with Annexin V to confirm that the binding is happening on the outer surface of the cellular membrane.

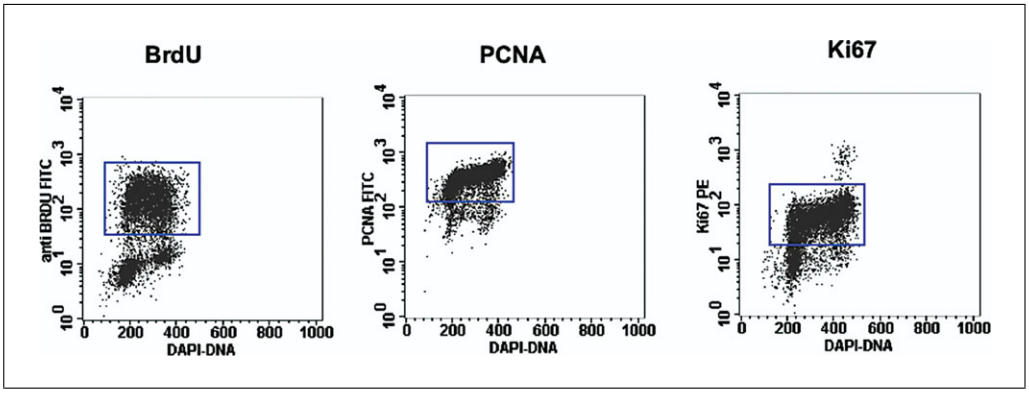

Figure 5.1.2 Example of BrdU, Ki67, and PCNA used to measure proliferation. Cells from the H23 lung cancer cell line were fixed and then stained with BrdU, Ki67 or PCNA, and DAPI. The BrdU sample was pulsed for 2 hr with BrdU prior to staining. The samples were counterstained with DAPI to indicate cell cycle as well as proliferation. The positive cells are indicated in the rectangular region.

TUNEL is a technique that utilizes the ability of terminal deoxynucleotidyl transferase (TdT) to label the ends of DNA breaks associated with apoptosis with dUTP (deoxyuridine triphosphate) or BrdU. The dUTP or BrdU are labeled with a fluorchrome for detection and the cells are counter stained with a DNA dye prior to data acquisition.

The caspase signaling pathway is activated in most cases of apoptosis. This is targeted by using intracellular staining and antibodies that are specific to the active form of caspase 3. There are additional assays that utilize fluorogenic substrates that when exposed to caspase activity are cleaved and then emit fluorescence.

Mitochondrial apoptosis does not always utilize the caspase pathway so different methods are used for detection. Most of these methods examine mitochondria membrane potential such as using the dye JC-1. However, there is an antibody against APO2.7 that is localized on the mitochondrial membrane and only expressed during apoptosis.

Molecular Biology

Fluorescent protein analysis

Fluorescent proteins (GFP, mCherry, YFP, mRuby, etc) are used as markers for protein expression. Typically, cells are transfected with a plasmid that contains a promotor sequence and encodes for a gene of interest along with a fluorescent protein. The expression of the fluorescent protein is used as an indicator for the expression of the gene of interest. More recently, the expression of a split bi- or tri-partied fluorescence complementation linked to other proteins allow detection of RNA–protein and protein–protein interactions. These methodologies revolutionized the detection and isolation of cells where the fluorescence is detected only in response to surrogate (Han et al., 2014). This technology is used for multiple applications, for example *in vivo* tracking of transplanted cells, bacterial or viral infections, and gene knockout in cells to further elucidate gene function.

Cell cycle analysis

Cell cycle analysis assays consist of staining DNA with a saturating amount of DNA binding dye. In most cases, the cells are fixed with a 70% ethanol solution which permeabilizes the cells and then stained with the dye (PI, 7AAD, DAPI). However, there are dyes that can enter living cells and stain DNA without harm to the cells such as Hoescht 33342. In this type of analysis, samples are acquired at a low flow rate with linear amplification and then analyzed using ploidy modeling software to determine the cell cycle phases.

Signal transduction flow cytometry

This application uses antibodies made against resting and phosphorylated signaling molecules. The use of these reagents and specialized buffers in staining panels allows for the study of signaling pathways in mixed populations of cells.

RNA flow cytometry

RNA flow cytometry combines flow cytometry with fluorescent *in situ* hybridization (FISH) to detect RNA expression along with protein expression. This technique requires staining panel optimization since not all fluorochrome conjugated antibodies will withstand treatment at 40°C for multiple 1 hr

incubations. It is a useful technique when antibodies are not available for a target and RNA expression can be used instead.

Cell Sorting

Cell sorting utilizes a flow cytometer with cell sorting capabilities to separate and purify cells or particles for further analysis. Essentially, any cell or particle that can be made fluorescent can be separated by a cell sorter. Cells can be sorted into 96 or 384 well plates, tubes and slides. A few common types of samples are transfected cells expressing a fluorescent protein, stem cells, tumor infiltrating lymphocytes, tumor cells, and white blood cell populations. A major consideration with any cell sort is scaling up the amount of antibody needed for staining large amounts of cells.

Other Applications

Absolute cell counting

Absolute cell counting can be added to any immunophenotyping experiment. The procedure utilizes fluorescent beads of a known concentration that is acquired along with the sample. The sample is analyzed and the gated number of cells for the population of interest is compared with the number of beads acquired in the same sample to generate the number of cells per milliliter.

Quantitative flow cytometry

Quantitative flow cytometry uses a bead based standard to generate a staining curve of known fluorescence amounts. Cells are then acquired with the same instrument settings and linear regression analysis is used to calculate the amount of fluorescence on the cells. Depending on the bead system used, this can be expressed as Antibodies Bound per Cell (ABC), Antibody Binding Capacity (ABC) or Molecules of Equivalent Soluble Fluorochrome (MESF). The best fluorochrome for this application is PE which, because of its size, almost always bind to an antibody with a 1:1 Fluorochrome to Protein Ratio. Molecular Equivalent of Soluble Fluorescence (MESF) standards can be used to convert arbitrary fluorescence intensity measurements to number of fluorescent molecules, by generating a standard curve and regression from MESF-bead data in any specific experiment, to quantitate approximate numbers of fluorescent labels on a cell.

Multiplexed bead array assays

Multiplexed bead array assays are sets of beads coated with antibodies against specific soluble proteins or nucleic acids. Each bead has a known amount of fluorescence and a specific target which gives a location for the bead in the matrix. The collection of up to 100 beads are incubated with the sample of interest, treated with a fluorescence reporter and then acquired on a flow cytometer with at least 2 lasers to detect the 2 different fluorochromes. Special software is used to calculate analyte amounts based on fluorescence.

Phagocytosis assays

Using fluorescently tagged bioparticles or bacteria, it is possible to detect phagocytosis using flow cytometry. The bacteria are labeled with a pH sensitive dye that only fluoresces when exposed to the lower pH of a phagosome, indicating that the bacteria are phagocytosed.

Small particle analysis and sorting

Using flow cytometers with enhanced sensitivity, it is possible to detect and sort exosomes and other sub-micron particles. Analysis of cellular exosomes, viruses, and other subcellular particles creates new applications in multiple fields including cancer biology, cancer therapy, and vaccine development. This technology is still in its development stages, but techniques and instrumentation are rapidly improving to make this application more accessible in the near future.

DATA ANALYSIS

FCS 3.1 File Standard

The FCS file format was created in 1984 to standardize flow cytometry list mode data files. All flow cytometry data files have the ".fcs" file extension that allow the files to be read by any flow cytometry analysis program. The current fcs file standard is FCS 3.1.

Conventional Flow Cytometry Analysis

Conventional flow cytometry analysis consists of drawing a region around a population of cells (gating) and applying that region to other parameters within the experiment. This allows specific groups of cells to be selected for further analysis of other markers. For example, helper T cells can first be defined by CD3+, CD4+ expression, and then analyzed for activation by looking within that population for expression of an activation marker, like CD25 (IL-2Rα), and then IFN-γ cytokine

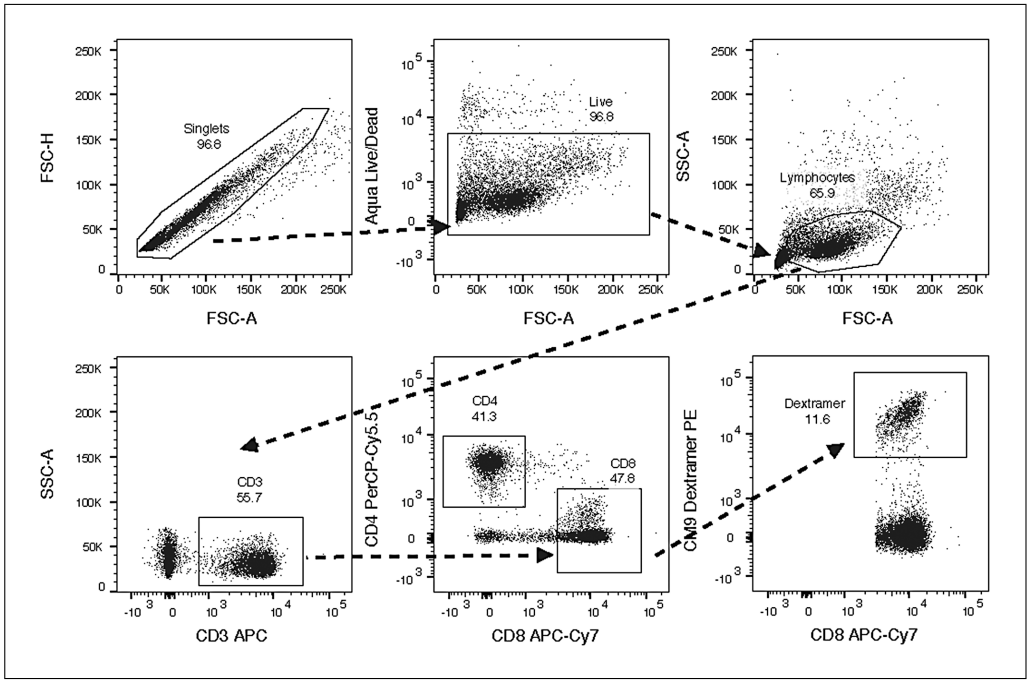

Figure 5.1.3 Example of gating for standard data analysis using FlowJo 10.3. Cells are first gated to remove doublets, for viability, for light scatter, and then for specific lineage markers. This example is looking at CM9(SIV-gag) Dextramer staining on CD8 cells in PBMC from a vaccinated *Rhesus macaque*.

production. An example of gating is in Figure 5.1.3.

Multiple commercial computer programs, in addition to the instrument-provided software, are available for analysis of flow cytometry data. The most popular are FlowJo, FCS Express, WinList, Kaluza and WinMDI.

Cell Cycle Analysis

Cell cycle analysis software programs uses ploidy modeling to determine the phase of the cell cycle represented by the DNA histogram. ModFit LT is a program dedicated to this type of analysis. In addition, a cell cycle analysis module is available on FlowJo.

Analysis of High Dimensional Data

Analysis of high dimensional data containing 14 plus parameters using conventional flow gating strategies is cumbersome and time consuming. In addition, it is possible to miss interesting populations of cells because relationships between markers are not easily determined using traditional gating methods. There are multiple new analytical tools that are being used to visualize and analyze this type of data. Examples are SPADE (Spanning-tree progression analysis of density-normalized events), tSNE (t-Distributed Stochastic Neighbor Embedding), PCA (Principal component analysis), and FLOCK (FLOw clustering without K).

Mathematically, t-SNE is similar to PCA, but it can identify more co-segregating features than PCA, since t-SNE optimizes only the clustering of similar objects with each other, while PCA optimizes both proximity of similar events and separation of dissimilar events. Most of these algorithms require data reduction or down sampling techniques to reduce the complexity of data prior to analysis.

Cytobank is another source for cloud-based high dimensional data analysis where users upload data and subscribe to the web-based platform. tSNE is available as plug-in for FlowJo and FCSExpress software.

LITERATURE CITED

Barteneva, N. S., Fasler-Kan, E., & Vorobjev, I. A. (2012). Imaging flow cytometry: Coping with heterogeneity in biological systems. *The Journal of Histochemistry and Cytochemistry*, *60*(10), 723–733. doi: 10.1369/0022155412453052.

Han, Y., Wang, S., Zhang, Z., Ma, X., Li, W., Zhang, X., . . . Cui, Z. (2014). In vivo imaging of protein-protein and RNA-protein interactions using novel far-red fluorescence complementation systems. *Nucleic Acids Research*, *42*(13), e103. doi: 10.1093/nar/gku408.

Leipold, M. D., Newell, E. W., & Maecker, H. T. (2015). Multiparameter Phenotyping of Human PBMCs Using Mass Cytometry. *Methods in Molecular Biology*, *1343*, 81–95. doi: 10.1007/978-1-4939-2963-4_7.

Mei, H. E., Leipold, M. D., & Maecker, H. T. (2016). Platinum-conjugated antibodies for application in mass cytometry. *Cytometry. Part A*, *89*(3), 292–300. doi: 10.1002/cyto.a.22778.

Matz, M. V., Fradkov, A. F., Labas, Y. A., Savitsky, A. P., Zaraisky, A. G., Markelov, M. L., & Lukyanov, S. A. (1999). Fluorescent proteins from nonbioluminescent Anthozoa species. *Nature Biotechnology*, *17*, 969–973. doi: 10.1038/13657.

Sony. (2017). Sony SA3800 Spectral Analyzer. Retrieved from https://www.sonybiotechnology.com/us/instruments/sa3800-spectral-analyzer/.

Tsien, R. Y. (1998). Green Fluorescent Protein. *Annual Review of Biochemistry*, *67*, 509–544. doi: 10.1146/annurev.biochem.67.1.509.

ISAC CYTOMETRY
Journal of Quantitative Cell Science PART A

Adapting to the Coronavirus Pandemic: Building and Incorporating a Diagnostic Pipeline in a Shared Resource Laboratory

Emma Russell, Ana Agua-Doce, Lotte Carr, Asha Malla, Kerol Bartolovic, Dina Levi, Carl Henderson, Debipriya Das, Hefin Rhys, Philip Hobson, Sukhveer Purewal, Andrew Riddell*

AT the beginning of February 2020, the COVID-19 outbreak in the UK gathered pace and it seemed highly probable that the United Kingdom would follow similar lockdown restriction policies seen in other European countries. The Crick's Flow Cytometry Science Technology Platform (Flow STP) helped prepare scientists to finish current experiments and store experimental material during lockdown to enable an efficient restart upon the eventual lifting of the restrictions. During this time safety measures were introduced into the Flow STP, including social distancing, that directly reduced the number of instruments available for use. When lockdown was announced in the United Kingdom on the 23rd March 2020 the total number of staff allowed into the Crick was reduced to a core group of key workers. The Flow STP was given key worker status and operated to provide flow cytometry to Crick scientists whose sole focus was now COVID-19.

In the lead-up to lockdown communications were sent to scientists to highlight the possible implications of the pandemic on Flow STP operation. There were significant changes in the way the Flow STP operated due to the challenges faced outlined in Table 1.

In early May 2020 the Crick prepared to support testing during the pandemic by establishing the Crick COVID-19 Consortium that successfully developed a diagnostic polymerase chain reaction (PCR) pipeline (1,2). The Flow STP was engaged to support COVID-19 research at the Crick, helping to develop novel flow cytometry assays utilizing SARS-CoV-2 virus-specific proteins. The STP was tasked with building a new clinical diagnostic lab and running a novel enzyme-linked immunosorbent assay (ELISA) that had been developed for detecting antibodies against the S1 spike of the SARS-CoV-2 virus. The key processes required are outlined in Figure 1.

SARS-CoV-2 Assay Development

The Flow STP was involved in the development of serology studies, comprising assays, and diagnostic tests focused on antibodies present in serum. Initially, work began on three assays: one cell-based, one bead-based, and an ELISA. The early development of these required many steps, beginning with a feasible idea through to procuring and testing reagents and methods. During protocol development testing was required to ensure their precision, accuracy, and coherence.

To accommodate the assay development and pipeline a restricted access containment level 2 (CL2) laboratory was created, housing a ZE5™ (Bio-Rad, Hercules, CA) and LSR Fortessa™ (BD Biosciences, San Jose, CA), for analysis of

The Francis Crick Institute, Flow Cytometry Science and Technology Platform, London, UK

Received 18 August 2020; Revised 23 September 2020; Accepted 19 October 2020

Grant sponsor: Cancer Research UK, Grant number: FC001999; Grant sponsor: Medical Research Council; Grant sponsor: Wellcome Trust

Additional Supporting Information may be found in the online version of this article.

*Correspondence to: Andrew Riddell, Flow Cytometry Science Technology Platform Lead, The Francis Crick Institute, 1 Midland Road, London NW1 1AT, UK. Email: andy.riddell@crick.ac.uk

Published online 22 November 2020 in Wiley Online Library (wileyonlinelibrary.com)

DOI: 10.1002/cyto.a.24248

Table 1. Table to highlight the approaches taken to overcome each challenge faced throughout the pandemic and pipeline creation

CHALLENGE	APPROACH
As a consequence of social distancing staffing levels had to be reduced.	Staff predominantly worked from home unless required to attend the Crick to aid in assay development. Other members of the team were furloughed under the government Coronavirus Job Retention Scheme. Employees received mandatory weekly COVID-19 swab tests to confirm suitability to work. A designated place was created in the lab where scientists could safely drop off and collect samples to reduce face-to-face contact. Users communicated with scientists via online video calling. Use of some instruments in close proximity was restricted, there was reduced occupancy in laboratories and extended cleaning regimes were put in place. Training was suspended to prevent any potential spread of infection, and remote support was provided as required.
The strict and constantly changing timelines for the development of both the assays and pipeline.	The Crick worked closely with a UKAS accredited medical laboratory to quickly meet the governance requirements allowing swift assay development.
Introducing the different approach required to work in diagnostics versus research.	The team was able to draw on diagnostic expertise from existing staff members within the Crick with a diagnostic background. We consulted with qualified biomedical scientists within the Crick to highlight where processes need adapting to conform to diagnostic standards.
Restrictions imposed by space available to accommodate equipment and staff.	A complete overhaul of both the layout and laboratory equipment was undertaken in less than a week to meet the requirements of a CL2 diagnostic facility.
Balancing the COVID-19 pipeline with usual workload responsibilities.	Users previously trained in cell sorting were required to perform their own sorts and analysis and were encouraged to help their nontrained colleagues to use the facility with oversight from the STP staff. During lockdown non-essential flow cytometry work was suspended and external users were banned.
Incorporating COVID-19 compliant practices into training regimes for new users.	Use of PPE including masks and face shields. Development of a series of online videos to provide an alternative to face to face contact.

serological samples. A second CL2 laboratory was created for ELISA testing.

The Role of Governance in Diagnostics

To operate as a clinical diagnostic lab specific standards must be attained. The United Kingdom Accreditation Service (UKAS) is a government-recognized body that provides certified testing, inspection, and calibration services together with an oversight function. UKAS requires medical laboratories to have International Organization for Standardization (ISO) 15189:2012 certification for quality and competence to run a clinical laboratory (3, 4). To meet these standards the Flow STP created new clinical-grade protocols and standard operating procedures (SOPs). The key requirements are auditability and the ability to connect the samples to their results; these shaped the protocols and the design of the Crick's new pipeline. The pipeline is in the process of attaining this accreditation.

Other standards and recommendations include those from the Royal College of Pathologists' "The retention and storage of pathological records and specimens" (5). These outline how to store samples and records required in relation to each sample. In the United Kingdom (and Europe) all personal data must be handled in accordance with data protection laws and regulations (the GDPR and UK Data Protection Act 2018) (6) and all internal recording and sample handling systems must be fit for purpose.

Completing adequate staff training was imperative and staff who built the necessary workflows and resources of the SARS-CoV-2 ELISA assay trained other staff to become competent in all processes of the pipeline. Those members of staff trained others until all were fully trained. A training log was kept for each member of staff as part of the audit process and

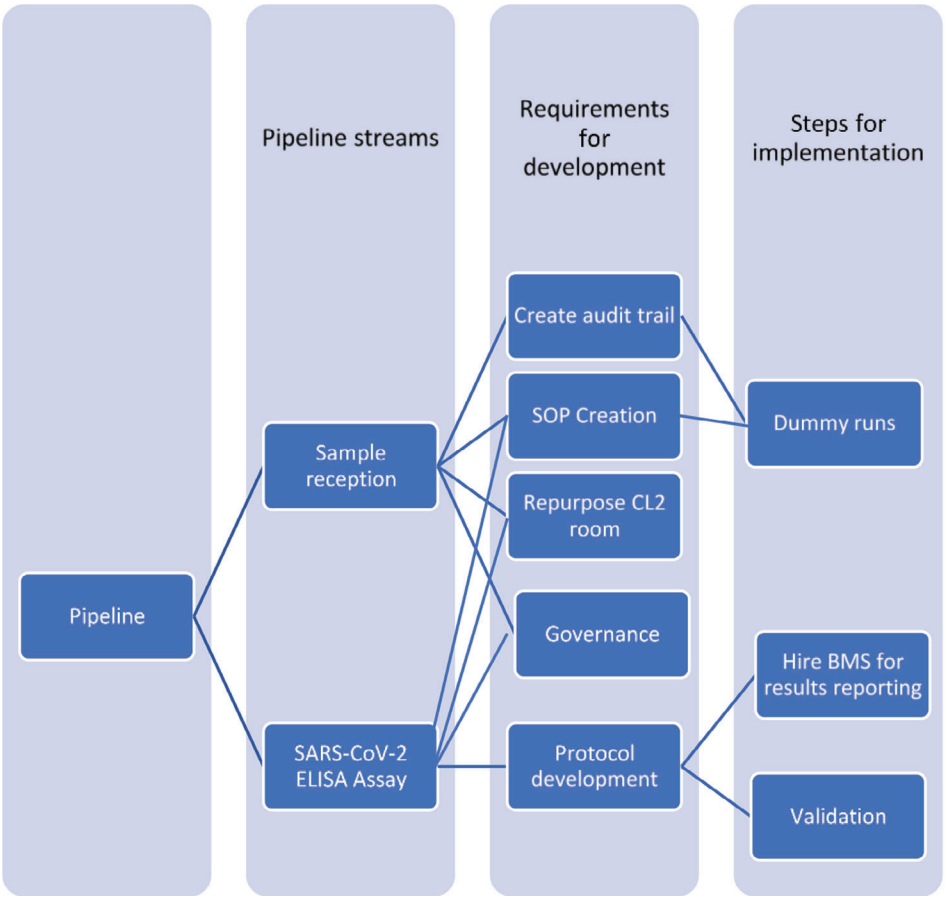

Figure 1. Outline of the key processes involved in pipeline development and implementation.

updated when new assays were introduced. The team received information regarding how sample handling adhered to the Human Tissue Act 2004 in the United Kingdom and training in the following areas:

- Good Clinical Practice (GCP) and the legal framework of a diagnostics lab.
- Data protection laws (the GDPR and UK Data Protection Act 2018) (6).

Auditability was achieved through recording processes within the pipeline. Internal quality control (QC) standards for the assays must be kept as specified in the ISO 15189:2012 standard. The following reports were stored and made accessible:

- Instrumentation QC, maintenance history and validation results.
- Reagents QC including validation batch numbers.
- External Quality Assurance (EQA) using a national or internationally recognized body, such as NEQAS in the United Kingdom (7).
- Maintenance and calibration records for equipment for example, pipettes used in the pipeline, must be kept for up to the lifetime of the equipment plus 4 years (5).
- The temperature of fridges and freezers via a sample management system to give an independent secondary recording.

Access to sample material was restricted in the interest of safety, information security, and confidentiality. Other governance comes from the Crick's institutional policy documents.

Rules on Results Reporting

The final step of the pipeline was reporting serology test results to a UKAS accredited medical laboratory by a certified Biomedical Scientist (BMS). The BMS's responsibility is to oversee the process and to ensure the results meet the specific standards set out above. They are given the processed results of the tests, as well as the raw data, to assess the quality and ensure they meet the standards for a clinical virologist to make a diagnosis.

Building a Diagnostic Pipeline

The audit trail formed the basis for the development of the sample reception process. At every decision point in

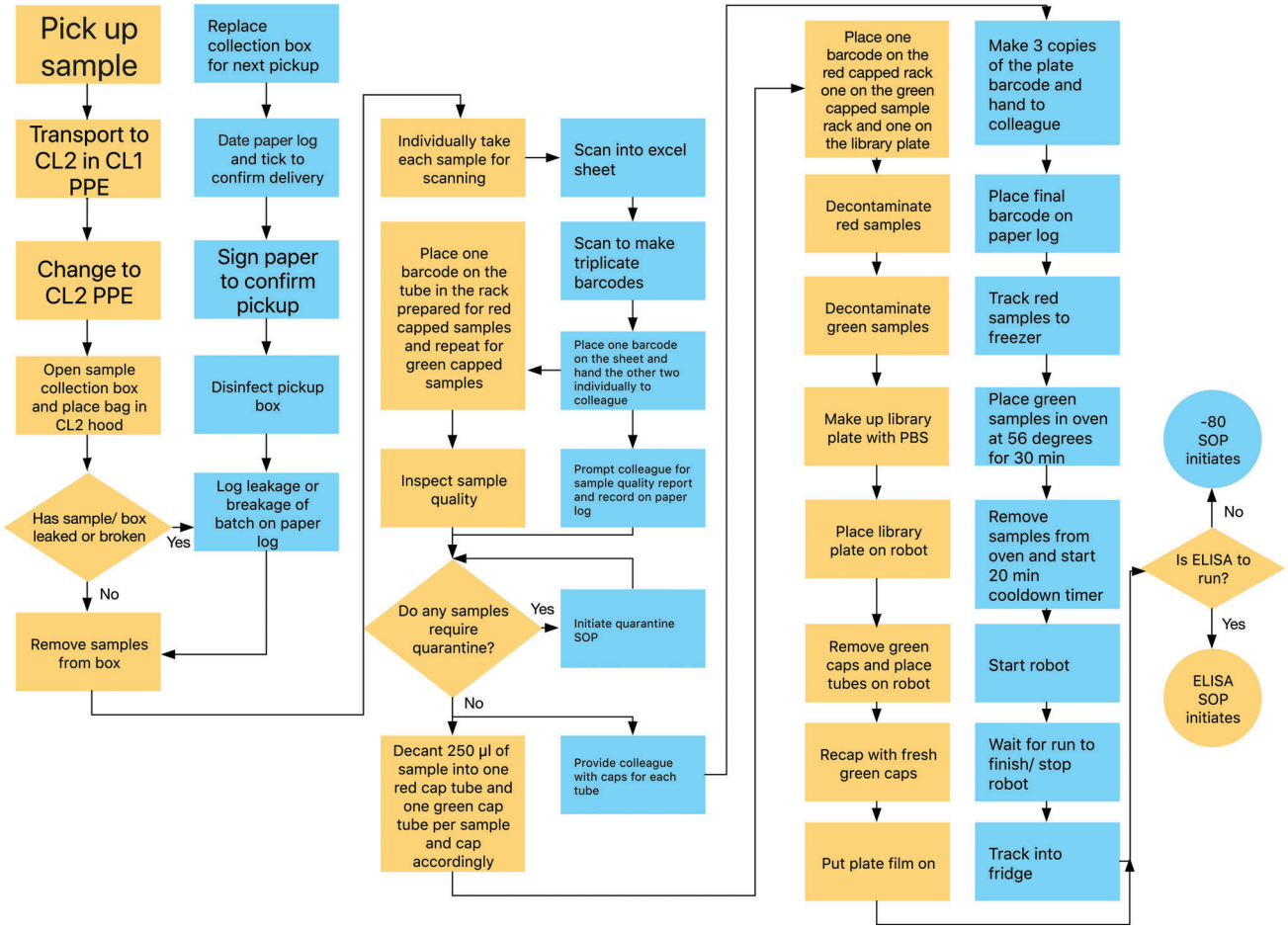

Figure 2. The flowchart outlines the steps taken along the pipeline from the moment of sample receipt to running the assay. The yellow pathway follows the person performing the tasks and making decisions. The blue pathway indicates a second person who checks the action of the person following the yellow pathway, as well as, tracking the sample manually along the pipeline. Rectangles denote actions, diamonds indicate decision points and circles provide the two end points.

designing the pipeline the primary concern was to ensure the sample could not be separated from its result. A two-person approach, as outlined in Figure 2, was used to enhance the level of security within the decision making and verification processes. SOPs were created to give clear guidelines for how the process should be carried out. These documents will be extended and added to over time.

Logs were created to identify the sample status across the entire pipeline and allowed identification of potential breakpoints along the way. For each breakpoint a contingency plan was developed in case of errors as shown in Table 2. The contingencies were then graded on a traffic light system: red, amber, and green to indicate the level of impact on the outcome of the assay and dictate the level of verification required.

As part of this process quarantine measures were introduced ensuring that unscheduled samples that arrived without manifests, or samples with specific rejection criteria were stored in a separate area. This was a location within the fridge that was separated by quarantine criteria notifying the team that the reporting body should be contacted for further instruction before samples were processed. This removed the chance of processing a sample that was not meant to be tested or one that met rejection criteria which would potentially invalidate the result.

As the pipeline developed, samples were received from multiple sources for various uses which required either diagnostic, research based or quality control output channels. The sample reception process was evolved to accommodate this.

Why Not Automate from the Outset?

The pipeline was started manually to get it working as quickly as possible and to enable a more efficient and timely digital development process. The parameters for a Laboratory Information Management System (LIMS) evolved from building the pipeline physically from scratch. Pressure tests in the form of dummy runs with batches of mock samples were undertaken to test the robustness of the manual pipeline. These steps were then used as a framework for digitization as shown in Table 3.

Table 2. Demonstrates examples of contingencies in place and their grading in case of operator error or equipment failures throughout pipeline.

ISSUE	CONTINGENCY	GRADE
Aspirator breaks.	Use multi-channel pipette to remove wash.	Green
No precoated plates prepared.	Masterplate stored in fridge at 4°C for up to 72 h.	Green
Barcode scanner breaks.	Manually record the barcode number in the paper log and on the 2 ml tube, proceed as normal.	Amber
Clumpy/hemolyzed sample upon aliquoting.	Record this information in log and continue.	Amber
Plate reader failure.	Add 50 µl of 1 M NaOH to quench plate at 15 min after addition of substrate, store in dark by wrapping in foil at room temperature until problem can be resolved. If >12 h repeat assay.	Red
Any steps not completed as per SOP/missed.	Terminate assay and repeat next day.	Red

Once all the parameters had been defined and tested automating the process removed multiple sources of potential human error. This increased not only the efficiency of the pipeline by reducing time spent performing manual steps but also freed up time spent by staff performing the tasks.

Initially, we used a commercial electronic sample tracking system already in place at the Crick. After collaborating with the Scientific Computing STP a web app-based LIMS was developed that encompassed all the specific requirements and parameters the commercial option could not. This custom-built system relied upon barcoding and robot technology to electronically track the samples through the pipeline. After further rounds of dummy runs and the creation of new SOPs, to include the new LIMS, the pipeline was fully automated leaving the manual system in place as a contingency for any potential point of failure.

Validating the Pipeline

Despite the abundance of recent studies on SARS-CoV-2 rigorous testing and knowledge of the immune response to the disease was still lacking. This posed a problem with reporting an accurate serological evaluation. Other ways of testing for SARS-CoV-2-specific antibodies were developed including both ELISA and flow cytometry assays with cells and beads. The development of such tests for diagnostic purposes required each variable to be tested and validated. There is currently no gold standard for SARS-CoV-2 serological tests so we used different commercial assays to cross validate our internal assays. Although mostly concordant, the different tests showed disparity between some positive samples. The disparity may be due to biological differences or varying assay sensitivities. Importantly, the negatives remained concordant.

Unlike in research, a diagnostic pipeline requires strictly defined protocols to minimize variability and ensure reliable reporting to external parties. The team identified steps in the pipeline where human error could possibly be introduced and incorporated extra checks or contingencies to prevent this. The first obvious step for introduction of human error was in the creation of the 96-well master plate. As well as human pipetting errors there was potential to introduce mismatches between sample position and sample ID. We therefore automated this step using a robot to decant samples from their tubes into a recorded position on the master plate. As the robot had not been previously used in a diagnostic pipeline several tests and validations had to be done. At least five runs of an ELISA assay with large sample numbers ($n > 30$) were carried out comparing the reproducibility of the robot to human pipetting.

We calculated the intra and inter percentage coefficients of variation (% CV) to measure the variability of samples both within and between each run. We found that dispensing samples using the robot gave an intra-assay % CV of 13.07 ± 14.86 (mean ± SD) while human pipetting resulted in an intra-assay % CV of 7.85 ± 4.74%. Conversely, robotic and human pipetting resulted in interassay % CVs of 19.45 ± 7.51 and 23.50 ± 11.63 respectively as shown in Figure 3. This suggested that while robotic sample dispensing increased intra-assay variation, believed to be due to uneven volume dispensing, it slightly decreased interassay variation. Importantly, we found the interassay variation in outcomes for each sample (as detected, not detected, or indeterminate) to be lower for robot versus human pipetting as shown in Figure 4. Taken together and with time constraints these data indicated that the assay uncertainty was within reasonable limits and the use of the robot for pipetting resulted in more consistent sample outcomes.

For validation it was necessary to demonstrate specificity, sensitivity and reproducibility within the results of the pipeline (8,9). Using the ELISA assay as an example we evaluated reproducibility by preparing multiple master plates with different operators. Our test batch of samples contained positives ($n = 45$) and negatives ($n = 40$) as previously confirmed by an independent laboratory through PCR and a commercially available assay. The criterion set for specificity was that tests should not report a negative sample as positive. The criterion for sensitivity was that tests should not report a positive sample as negative. Finally, for reproducibility the criterion was that results should be consistent among the five

Table 3. Breakdown of the steps involved in the pipeline, how each step is manually recorded and the proposed electronic alternative

TASK	MANUAL STEP	ELECTRONIC ALTERNATIVE
Samples received by the Crick from courier.	Sample delivery recorded via Crick usual processes	Notification system alerts Flow team that samples have been received
Samples collected from Crick drop off point and transported in the transfer box via shortest route.	Operator signs the paper log to confirm collection of samples	Notification system alerts Flow team the samples are in transit to the lab
Sample container placed in hood and visually inspected for leakages.	Operator records if any sample leakages seen on paper log	Operator records if any sample leakages are seen on LIMS
Samples scanned to confirm receipt.	Record made on the paper log of number on box	Notification system alerts sender samples have been received
Quarantine process initiated for any samples that are unexpected, incorrect or missing.	Quarantine logbook on sample fridge requires signing into the fridge with specific location and reason for quarantine.	Fridge Log tracks what samples are in which section of quarantine and notification system alerts sender samples are waiting.
For each sample 250 µl of serum will be transferred into one 5 ml tube and has a bar code attached.	One barcode is stuck to the paper log to confirm which tubes have been received.	Notification system records which samples match those we are expected to receive and highlights any "Quarantine" samples.
Serum quality logged for any hemolyzed or viscous samples.	Any samples that are hemolyzed or viscous are marked next to their barcode on the paper log.	Option on the dashboard to select sample is hemolyzed or viscous for specific samples.
Up to 40 samples are placed onto the robot and duplicated in a 96-well plate (Library Plate) with one Plate Manifest barcode.	Table filled in with sample barcodes. A copy of the Plate Manifest barcode is attached.	The Plate barcode is scanned. The robot individually scans the barcode of each sample and tracks it into whichever well the sample is placed. A plate manifest layout document is created with the date and time.
40 original 5 ml tube samples tracked for −80°C storage and the date and time marked on the rack.	Date and time of the 5 ml samples recorded.	FreezerPro® records date and time the 5 ml samples are being tracked.
Sample tubes are stored in the fridge (4°C) until ELISA is complete.	Operator signs samples into fridge using paper log.	N/A
ELISA process carried out.	SOP checklist double signed to confirm operator has carried out each stage.	Electronic checklist updated when each section of ELISA SOP completed.
ELISA plate placed on reader.	Plate barcode is recorded on paper log.	Scan plate onto reader so that notification system logs plate barcode as "being read".
Results generated for reporting.	Print a copy of the CSV. File generated by the plate reader and store.	Electronic reporting process carried out via LIMS.
Completed samples are transferred from fridge to freezer.	Sign in and sign out sheet on each fridge detailing what samples are where.	FreezerPro®.

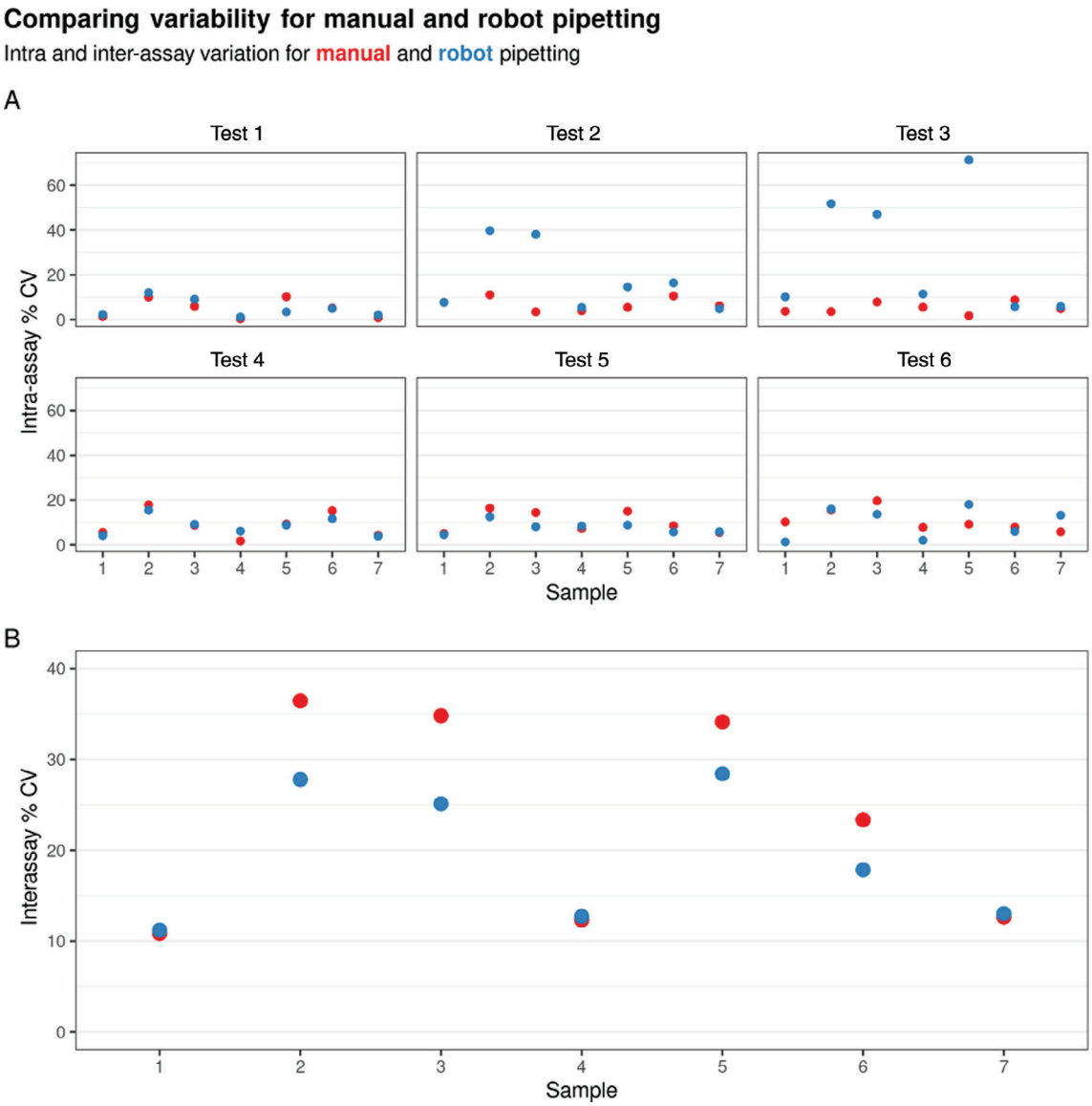

Figure 3. The variability between robot and manual pipetting. (**A**) Intra-assay percent coefficients of variation (% CV) for each sample across separate subplots for each experimental run. (**B**) Interassay % CV for each sample, collapsed across experimental runs.

different repeats. Our results showed the tests were reproducible, specific and sensitive as defined in Table 4.

Most diagnostic assays do not include standard curves because they are designed to provide a "YES" or "NO" answer. During the process of pipeline validation however, we included standard curves in some tests. These standard curves provided us with parameters such as limits of detection (20.41 pg/ml equivalent of positive control antibody with 95% confidence interval [17.67, 24.65]) and dilution linearity as shown in Figure 5 and defined in Table 4. Dilution linearity demonstrated that the coating did not interfere with accurate detection or result in nonspecific binding.

While our methods covered all the parameters required for confidence it remained necessary to evaluate each sample individually. It was imperative to evaluate sample stability because assays could be conducted at different time points. For this the same set of samples kept at 4°C were tested at different time points over 2 weeks.

The New Normal

In June 2020 lockdown restrictions were eased; members of the Crick started to return to work in a phased approach and normal staff duties began to increase. The decision was made to split the Flow STP into two groups on a rota basis to enable social distancing and to prevent the entire team having to self-isolate if one member tested positive for COVID-19. Careful management of staff time was required taking into consideration both annual and sick leave requirements.

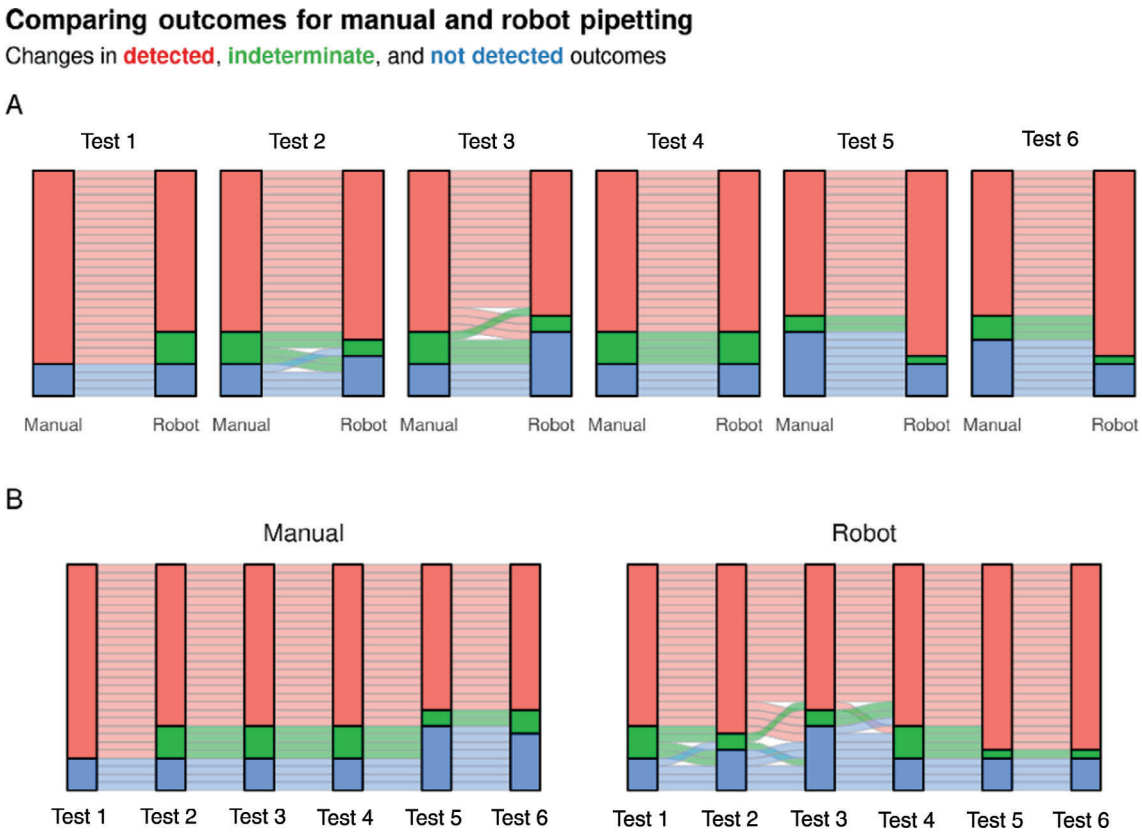

Figure 4. The reproducibility between robot and manual pipetting. (**A**) Alluvial plots showing how the outcome for each well changes when dispensed manually or with the robot. Separate subplots are drawn for each experimental run. Each horizontal ribbon represents a single well and is colored by its manual pipetting outcome. (**B**) The same data as in A showing how the outcome for each well changes between experimental runs. Separate subplots show manual and robot pipetting data.

Table 4. Summary of parameters used to validate the performance and suitability of the ELISA assay

	PARAMETER	RESULT
1	Reproducibility.	1.18 ± 0.83% of samples had discordant outcomes[a]
2	Sensitivity.	87 ± 3.0%[a]
3	Specificity.	100%[a]
4	Uncertainty.	Intra and interassay % CVs of 8.08 ± 7.23 and 14.57 ± 6.99, respectively[a]
5	Limits of detection.	20.41 pg/ml equivalent of positive control antibody with 95% confidence interval [17.67, 24.65][b]
6	Dilution linearity.	Linear relationship between log positive control antibody concentration and log absorbance[b]

[a]Mean ± standard deviation of five runs with 40 samples per run.
[b]From six independent standard curves of positive control antibody from 0.8 to 200 ng/ml.

This reduction in staff numbers combined with the running of the clinical diagnostic pipeline had a major impact on the services the Flow STP could provide. The pre-COVID workload could not be sustained and was streamlined. Prior to the lockdown we had pretrained scientists who were able to perform cell sorting both for themselves and their colleagues. Post lockdown this relieved a large burden on the Flow STP and enabled scientists to continue their research independently. The online booking system was adapted and we implemented a more consultative approach to staff planning and cell sorting which helped triage service requests.

The Flow STP continues to aid researchers with COVID-19 experiments. As previously discussed flow-based serological assays continue to be under development internally. These will be added to the clinical diagnostic pipeline based on their success. The reality of the "new normal" for the Flow STP at the Crick is to continue and build on our work on serology assays as a clinical diagnostics lab as well as maintaining an effective flow cytometry service to the Crick research labs. Although our time has been repurposed, putting constraints on our usual duties, we are delighted to contribute our newly adapted services to assist in this global pandemic.

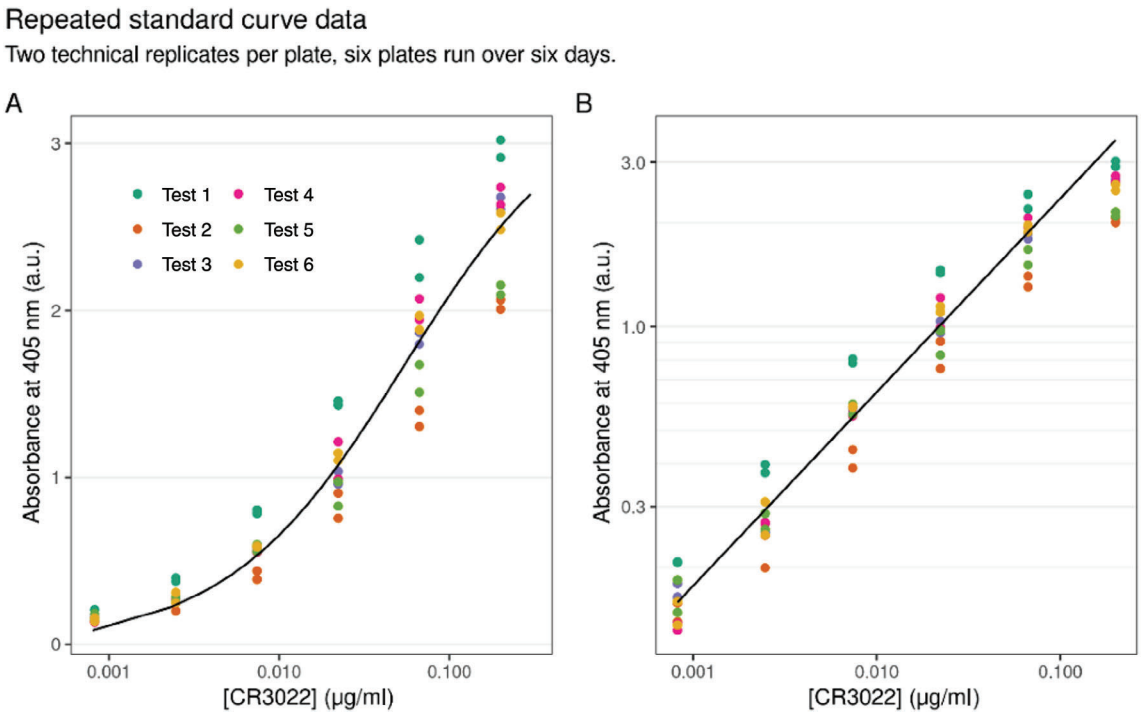

Figure 5. Concentration of the anti-S1 spike protein antibody CR3022 (the assay positive control antibody) against absorbance at 405 nm after performing six independent ELISAs. (**A**) is plotted on a natural scale and (**B**) is plotted on a semi-log scale. Two technical replicates per plate are shown. Note that except for the saturating concentration the relationship between log concentration and log absorbance is linear which indicates dilution linearity.

Conclusion

The challenges faced by the Flow STP can be separated into those created by COVID-19 regarding the changes required to everyday working practices and those posed by the uncertainty and novelty of creating the pipeline as outlined in Figure 1. The practices that have been put in place to overcome the first continue to be instilled in the current climate and are expected to ease off in line with both government advice and updates to Crick policies. While this project would have been possible without it, the team recognizes the advantage of having diagnostic expertise to advise and guide the pipeline development process. Particularly to maximize efficiency by avoiding potential pitfalls. Should the reader be looking to perform a similar process the authors recommend consulting with diagnostic expertise to facilitate this. Incorporating the pipeline into our daily tasks while at reduced staffing levels remains an ongoing challenge. The Flow STP have successfully carried out the development and implementation of a novel SARs-CoV-2 ELISA pipeline with the confidence that it is fit for purpose and ready for handover to be maintained outside the Flow STP when required.

Acknowledgments

To set up a clinical diagnostics lab in such a short time frame required a huge level of collaboration and assistance from other members of the Crick. Firstly, thank you to the Safety, Health and Sustainability team as well as Nicola O'Reilly for their advice on protocols and for helping us to set up the CL2 laboratories. Secondly, Richard Byrne, Gill Adams, Mathew Sargent and all the hub team for responding to our instrumentation requests so rapidly. With regards to ELISA assay development we would like to thank Laura McCoy from UCL, George Kassiotis and his team for their help and Peter Cherepanov for developing the protein coating for the ELISA as well as beads used in the bead assay. Also, thank you to Jerome Nicod for providing us with the robots, to Theo Sanderson for programming them and Phil Walker for setting up the barcoding system. In addition we would like to acknowledge the Crick COVID-19 Governance Team for their support and guidance, to thank Richard Stone and Emma Nye for reviewing the pipeline and the Crick's Scientific Computing STP for helping to set up a reporting strategy and the LIMS. Many thanks to Kathleen Evans for her invaluable input. Finally, the team would like to extend their thanks to all those who have not specifically been mentioned but who were fundamental to making this project possible. This work was supported by the Francis Crick Institute which receives its core funding from Cancer Research UK (FC001999), the Research Councils UK Medical Research Council (FC001999), and the Wellcome Trust (FC001999).

AUTHOR CONTRIBUTIONS

Emma Russell: Conceptualization; formal analysis; project administration; validation; writing-original draft; writing-

review and editing. **Ana Agua-Doce:** Conceptualization; formal analysis; project administration; validation; writing-original draft; writing-review and editing. **Lotte Carr:** Conceptualization; formal analysis; project administration; validation; writing-original draft; writing-review and editing. **Asha Malla:** Writing-original draft; writing-review and editing. **Kerol Bartolovic:** Conceptualization; writing-original draft; writing-review and editing. **Dina Levi:** Writing-original draft; writing-review and editing. **Carl Henderson:** Writing-original draft; writing-review and editing. **Debipriya Das:** Writing-original draft; writing-review and editing. **Hefin Rhys:** Conceptualization; formal analysis; project administration; validation; writing-original draft; writing-review and editing. **Philip Hobson:** Conceptualization; formal analysis; project administration; validation; writing-original draft; writing-review and editing. **Sukhveer Purewal:** Conceptualization; project administration; writing-original draft; writing-review and editing. **Andrew Riddell:** Conceptualization; formal analysis; project administration; resources; writing-original draft; writing-review and editing.

Declaration

The following rationale was applied to conclude that no ethics approval was required to conduct this assay development:

- Sera is not HTA relevant material.
- Samples used were leftover serum samples from routine clinical testing of individuals, not taken for a purpose within the remit of Research Ethics Committees.
- Individual samples were anonymized such that no personal identifying information was present.

These samples were provided with appropriate consents from the source.

Literature Cited

1. Houlihan CF, Vora N, Byrne, T, Lewer, D, Kelly, G, Heaney, J, Gandhi, S, Spyer, MJ, Beale, R, & Cherepanov, P, et al. Pandemic peak SARS-CoV-2 infection and seroconversion rates in London frontline health-care workers. Lancet 2020;396:e6–e7.
2. Aitken, J, Allen, Z, Ambler, R, Ambrose, K, Ashton, E, Avola, A, Balakrishnan, S, Barns-Jenkins, C, Barr, G, & Barrell, S , et al. Scalable and robust SARS-CoV-2 testing in an academic center. Nat Biotechnol2020;38:927–931.
3. Medical laboratories — Requirements for quality and competence (ISO 15189:2012). EUROPEAN COMMITTEE FOR STANDARDIZATION Ref. No. EN ISO 15189: 2012
4. Burnett DA. Practical Guide to ISO 15189 in Laboratory Medicine. London, UK: ACB Venture Publications, 2002.
5. Royal College of Pathologists. The Retention and Storage of Pathological Records and Specimens. 5th ed. London, UK: Royal College of Pathologists, 2005.
6. https://libraryfaqs.worc.ac.uk/faq/230277
7. https://ukneqas.org.uk
8. https://www.oie.int/fileadmin/Home/eng/Health_standards/aahm/current/chapitre_validation_diagnostics_assays.pdf
9. (https://www.ncbi.nlm.nih.gov/pmc/articles/PMC4541289/)

A Mouse Model of Sublethal Leptospirosis: Protocols for Infection with *Leptospira* Through Natural Transmission Routes, for Monitoring Clinical and Molecular Scores of Disease, and for Evaluation of the Host Immune Response

Nisha Nair[1] and Maria Gomes-Solecki[1,2]

[1]Department of Microbiology, Immunology and Biochemistry, The University of Tennessee Health Science Center, Memphis, Tennessee
[2]Corresponding author: *mgomesso@uthsc.edu*

Leptospirosis is a zoonotic disease caused by pathogenic *Leptospira* species that are maintained in sylvatic and domestic environments by transmission among rodents and other carriers. Humans become infected after contact of breached skin or mucosa with contaminated water or soil. Understanding persistent or sublethal infection in a host is critical for controlling human risk of exposure to pathogenic *Leptospira*. Animal models that recapitulate disease progression after infection via natural transmission routes are more appropriate for validation of vaccines and therapeutics. Furthermore, the ability to measure shedding of live *Leptospira* in urine of reservoir and carrier hosts can be used to develop new diagnostic assays and sensors to evaluate human risk of exposure. We developed inbred mouse models of Leptospirosis, that bypass survival as a criterion, in which we can analyze both pathogen and host factors affecting sublethal infection (<1 month), including shedding of *Leptospira* in urine. Mice are infected with pathogenic *Leptospira* using a physiologic route, and the clinical, histological, and molecular scores of disease are measured. Furthermore, the host immune response to *Leptospira* is evaluated. This mouse model also provides a tool in which to test fundamental hypotheses related to host-pathogen interactions and the immune mechanisms engaged in protective and pathogenic immune responses.

Basic Protocol 1: Culture and maintenance of virulent *Leptospira*
Basic Protocol 2: Infection of mice through a physiologic route and collection of clinical scores and biological samples
Basic Protocol 3: Analysis of pathogenesis after *Leptospira* infection

Keywords: *Leptospira* • mouse model • natural transmission routes • physiologic route of infection • sublethal leptospirosis

CURRENT PROTOCOLS
A Wiley Brand

Current Protocols in Microbiology e127, Volume 59
Published in Wiley Online Library (wileyonlinelibrary.com).
doi: 10.1002/cpmc.127

INTRODUCTION

Leptospirosis is a neglected emerging zoonotic disease with worldwide distribution that affects virtually all vertebrates, mostly in tropical regions in resource-poor countries. It is estimated to cause ~1 million cases and ~60,000 deaths a year globally (Costa et al., 2015). Reservoir hosts of *Leptospira* (e.g., rats, mice) and other carriers (cows, sheep, dogs, wildlife) become persistently infected and shed the bacteria in urine into the environment, maintaining the spirochete in its enzootic cycle. Humans become infected after contact of breached skin or mucosa with contaminated water or soil (Bharti et al., 2003; Casanovas-Massana et al., 2018; Schneider et al., 2018). Rats are good empirical animal models of chronic (>3 months) infection (Bonilla-Santiago & Nally, 2011, Thiermann, 1981), but the lack of reagents for immunology research limit their use. Our goal was to develop inbred mouse models of Leptospirosis that bypass survival as a criterion, in which we can study both pathogen and host factors affecting persistent sublethal infection (<1 month) and shedding of live *Leptospira* in urine.

We describe a mouse model of sublethal leptospirosis that produces consistent measurable readouts of disease progression and pathogen dissemination following infection through natural physiologic routes (Nair, Guedes, Werts, & Gomes-Solecki, 2020; Sullivan, Nair, Potula, & Gomes-Solecki, 2017). This model helps investigators understand persistent human disease, which affects ~90% of patients (Costa et al., 2015). It can be used to acquire data on the performance and toxicity of therapeutics for sublethal leptospirosis, on the efficacy and safety of vaccines including shedding-blocking vaccines, and on the antibody- and cellular-mediated immune mechanisms engaged in protective or pathological immune responses to vaccines or to other immunomodulator agents. It can be used to acquire proof-of-principle data on sensitivity, specificity, and accuracy of new non-invasive diagnostic tools designed to capture *Leptospira* directly in urine for human and veterinary applications. Furthermore, it can be used for analysis of host-pathogen interactions using pathogenic, intermediate, and non-pathogenic *Leptospira* serovars and to answer other basic research questions that require analysis of primary cells after infection or vaccination of live animals. Below is a representation of the methods herein described (Fig. 1).

Basic Protocol 1: Culture and maintenance of virulent Leptospira

Here, we describe how to culture *Leptospira* in vitro, how to quantify *Leptospira* both by counting live motile bacteria under a dark-field microscope and by qPCR, how to freeze

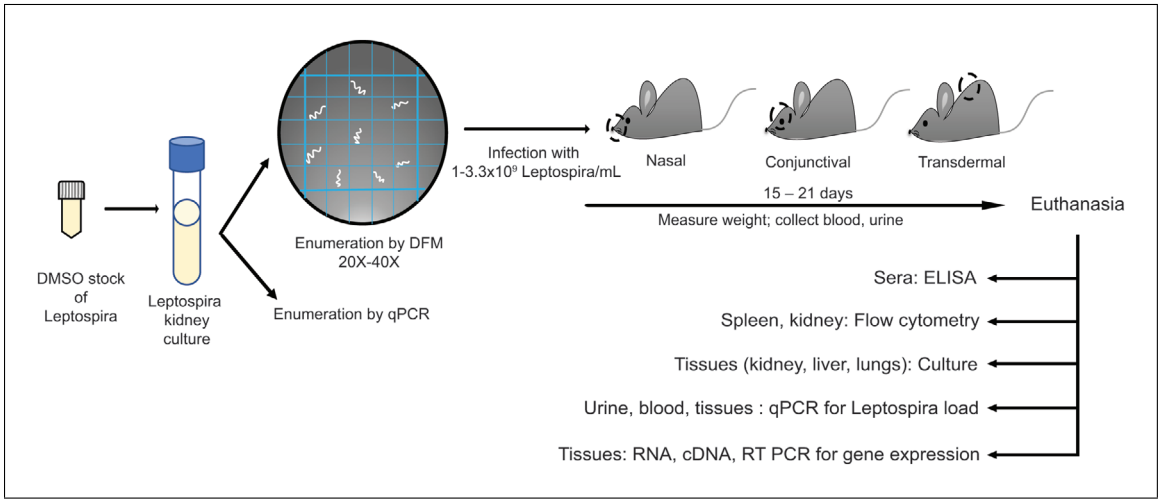

Figure 1 Workflow for infection of mice with pathogenic *Leptospira* and subsequent collection of biological samples.

cultures, and how to passage cultured pathogenic *Leptospira* in hamster to maintain virulent stocks in the laboratory.

Basic Protocol 2: Infection of mice through a physiologic route, and collection of clinical scores and biological samples

In this protocol, we describe how to infect mice with pathogenic *Leptospira* using three natural physiologic routes of infection (transdermal abrasion and conjunctival and nasal mucosa), how to record clinical scores (weight) that correlate with disease progression, and how to collect blood, urine, and tissues to process for analysis of pathogenesis.

Basic Protocol 3: Analysis of pathogenesis after Leptospira infection

The purpose of this protocol is to provide guidance on which techniques to use to evaluate dissemination of *Leptospira* to target tissues and how to evaluate molecular, cellular, and histologic differences that characterize the immune response to infection and tissue inflammation.

CULTURE AND MAINTENANCE OF VIRULENT *LEPTOSPIRA*

BASIC PROTOCOL 1

In vitro culture of *Leptospira* is essential to produce the inoculum needed for assessment of host-pathogen interactions. Furthermore, a growth curve is the gold standard test of bacterial viability. Here, we describe how to culture *Leptospira* in vitro from a frozen stock, how to quantify the number of spirochetes in culture, and how to make stocks for freezing. Finally, we describe how to passage *Leptospira* in vivo to produce highly virulent bacteria from hamster kidney, which is then maintained by n vitro subculture. Quantification of live *Leptospira* is done by enumeration of motile spirochetes in a Petroff-Hausser chamber under a dark-field microscope followed by confirmation by qPCR. All of these techniques must be mastered before infection of live animals.

Definitions

BSL2/ABSL2 = Biosafety Level 2/Animal Biosafety Level 2
EMJH = Ellinghausen-McCullough-Johnson-Harris
PPE = personal protective equipment
DFM = dark-field microscopy
PCR = polymerase chain reaction
RT-PCR = reverse-transcriptase polymerase chain reaction
DNA = deoxyribonucleic acid
PBS = phosphate-buffered saline

CAUTION: Biosafety Level 2 (BSL-2)/Animal Biosafety Level 2 (ABSL-2) procedures must be used for handling *Leptospira* cultures and infected hamsters. Personal protective equipment (PPE) needed: glasses or goggles, cap, mask, gloves, and gown.

NOTE: All animal experiments require approval by the local ethical and animal handling offices.

Materials

Pathogenic *Leptospira* species (*Leptospira*): we use *Leptospira interrogans* serovar Copenhageni strain Fiocruz L1-130 (ATCC #BAA-1198)
EMJH base medium (BD, cat. no. 279410)
Leptospira enrichment EMJH (BD Difco™, cat. no. 279510)
DNeasy Blood & Tissue Kit (Qiagen, cat. no. 69506)
Maxima Probe/ROX qPCR 2× mix (Thermo Fisher Scientific, cat. no. K0233)
Leptospira-specific TAMRA probe and 16S rRNA primers (Eurofins Scientific, Table 1)

Table 1 TAMRA Probes and Primers for RT-PCR

Leptospira specific	
Lepto_F	CCCGCGTCCGATTAG
Lepto_R	TCCATTGTGGCCGAACAC
LIC_TAMRA	CTCACCAAGGCGACGATCGGTAGC
Mouse specific	
β-actin _F	CCACAGCTGAGAGGGAAATC
β-actin_R	CCAATAGTGATGACCTGGCCG
β-actin_TAMRA	GGAGATGGCCACTGCCGCATC
TNF-α_F	CACACTCAGATCATCTTCTCAAAAT
TNF-α_R	AAGGTACAACCCATCGGCTGGCA
TNF-α-TAMRA	AGCCTGTAGCCCACGTCGTAGCAAAC
IFN-γ _F	CAAGTGGCATAGATGTGGAAGAAA
IFN-γ_R	CTGGCTCTGCAGGATTTTCA
IFN-γ-TAMRA	GGAGGAACTGGCAAAAGGATGGTGAC
RANTES_F	AGTGCTCCAATCTTGCAGTCGT
RANTES_R	CTTCTTCTCTGGGTTGGCACACACT
RANTES-TAMRA	TTGTCACTCGAAGGAACCG
MIP2_F	TGACTTCAAGAACATCCAGAGCTT
MIP2_R	CTTGAGAGTGGCTATGACTTCTGTC
MIP2-TAMRA	TGACGCCCCCAGGACCCCA
KC_F	CGAGGCTTGCCTTGACCCTGAA
KC_R	GGGACACCTTTTAGCATCTT
KC_TAMRA	CCCTTGGTTCAGAAAATTGTCCA
IL-4_F	TGTACCAGGAGCCATATCCA
IL-4_R	TTCTTCGTTGCTGTGAGGAC
IL-4_TAMRA	ATCCATCTCCGTGCATGGCG
iNOS_F	GCTGGGCTGTACAAACCTTC
iNOS_R	GCATTGGAAGTGAAGCGTTTC
iNOS_TAMRA	GGCAGCCTGTGAGACCTTTGAT
ColA1_F	TAAGGGTACCGCTGGAGAAC
ColA1_R	GTTCACCTCTCTCACCAGCA
ColA1_TAMRA	AGAGCGAGGCCTTCCCGGAC

Dimethyl sulfoxide (DMSO) (Sigma-Aldrich, cat. no.D2650-100ML)
Liquid nitrogen (N_2)
Phosphate-buffered saline (PBS; Sigma-Aldrich, cat. no. TMS-012-A)
Hamster, 4-weeks-old, male or female
Forane (Isoflurane, USP, Baxter, SKU cat. no. 10011936060)

14-ml round-bottom tube (Thermo Fisher Scientific, cat. no.150268)
30°C incubator
Glass slides and coverslips (VWR micro cover glass)
Dark-field microscope (DFM; Zeiss, USA)
Petroff-Hausser chamber (Hausser Scientific, cat. no.3900)

Eppendorf minispin microcentrifuge (Eppendorf, cat. no. 022668498)
StepOne Plus Real-Time PCR System (Thermo Fisher Scientific, cat. no. 43-766-00) or any other real-time PCR system
MicroAmp™ Fast Optical 96-Well Reaction Plate with Barcode, 0.1 ml (Thermo Fisher Scientific, cat. no. 4366932)
0.5 ml O-ring screw-cap cryovials (Midsci, SKU cat. no. AV-2125-S0)
Syringe (BD, cat. no. 309657)
21-G needles (BD, cat. no. 305167)
Somnosuite (Kent Scientific Corporation, cat. no. SS-01)
Surgical equipment

Additional reagents and equipment for euthanasia (see Current Protocols article: Donovan & Brown, 2006a) injection (see Current Protocols article: Donovan & Brown, 2006b), and anesthesia (see Current Protocols article: Donovan & Brown, 2001) of rodents

Culture of Leptospira in vitro

1. Thaw 250 µl of a frozen stock and immediately add to 4.25 ml of EMJH base medium. Add 500 µl of the supplement (BD Difco™ *Leptospira* enrichment EMJH) and add 5-fluorouracil at a final concentration of 100 µg/ml in a 14-ml round-bottom tube.

2. Place cultures at 30°C up to 4 weeks.

   5-Fluorouracil prevents contamination of the culture by inhibiting the growth of other organisms, but does not affect the growth of Leptospira. When reviving a frozen stock, inoculate quickly after thawing into supplemented EMJH base, and add 5-FU 3-4 days after confirming growth under dark-field microscopy (DFM).

3. Monitor the culture for the presence of live, motile spirochetes by DFM every 3-4 days: deposit 5 µl of culture on a glass slide and cover with a coverslip before checking under the 40× objective of the microscope. Set aside a 100-µl aliquot of the culture for quantification by qPCR.

   Other pathogenic Leptospira species should grow under these standard conditions. However, differences exist between species and serovars. If the above protocol proves unsuccessful, consider trying modifications such as replacing plastic tubes with glass, wrapping tubes in aluminum foil to provide a dark environment, and adding or omitting supplements in the EMJH base (unpub. observ.).

Quantification and determination of viability

Quantification of *Leptospira* can be done by DFM of cultured *Leptospira* and confirmed by amplification of *Leptospira* 16S rRNA by qPCR.

Quantification of live Leptospira by DFM

4. Add 10 µl of a 1- to 3-week-old culture of *Leptospira* to the grid of a Petroff-Hausser (PH) chamber and cover the grid with a glass coverslip.

5. Count motile spirochetes in five fields of the PH chamber under a DFM set at 20× or 40×.

6. To graph a growth curve, count the number of *Leptospira* at a minimum of three time points—e.g., d1, d7, and d14 if growing *Leptospira* from a frozen stock; or d1, d3, and d7 if growing *Leptospira* from infected kidney.

The total number of *Leptospira* in the culture is calculated as follows:

No. of bacteria/ml = (avg. of 5 squares) × 25 × dilution factor × 50,000.

Quantification of live and dead Leptospira by qPCR

7. *Prepare a known standard curve of a Leptospira stock:* Take 10^8 *Leptospira* cells enumerated under DFM and microcentrifuge at maximum speed in an Eppendorf minispin microcentrifuge. Purify the DNA with a DNeasy kit and serially dilute to 10^5-10^1 cells/μl.

8. Load 18 μl of PCR master mix per well (prepared using *Leptospira*-specific primers and TAMRA probe (listed in Table 1) and Maxima Probe/ROX qPCR 2× mix, as per the instructions of Maxima probe/ROX 2× mix user guide) on a MicroAmp™ Fast Optical 96-Well Reaction Plate.

9. Add 2 μl of the known standard curve DNA and 2 μl of the test culture (1-3 week old) into separate assigned wells.

10. Run the StepOne Plus PCR machine program recommended for the Maxima Probe/ROX qPCR master mix (usually 40 cycles).

11. Analyze data by comparison to the known standard curve.

Leptospira are always quantified by DFM before inoculation of live cultures into animals; qPCR is used as a confirmatory method, employing primers and probes specific for the Leptospira species of interest, keeping in mind that qPCR will amplify DNA from both live and dead spirochetes.

Live culture quantification by DFM should be within 1 Log of qPCR quantification. Counting with Petroff-Hausser chamber under DFM is considered the gold standard for enumeration.

Personnel should be previously trained in use of the qPCR machine.

Freezing a culture of Leptospira

12. Add 4% of DMSO to a culture of *Leptospira* after it reaches cell density $>10^7$ cells/ml.

13. Add 250 μl of culture per 0.5-ml cryovial and freeze at −80°C or in liquid nitrogen immediately.

Infection of hamsters

Maintenance of virulence in pathogenic *Leptospira* requires passaging cultured bacteria in hamsters in vivo. Virulent *Leptospira* are obtained by culturing kidney from infected hamsters.

14. Inoculate 500 μl of PBS containing 1000-5000 *Leptospira* previously quantified by DFM into the peritoneal cavity of an hamster anesthetized with 2%-5% isoflurane using a Somnosuite instrument according to the manufacturer's operating instructions.

Intraperitoneal injection of rodents is described in detail in Current Protocols article Donovan & Brown (2006). Anesthesia of rodents is described in Current Protocols article Donovan & Brown (2001).

15. Monitor the hamster for 15 days: record weight and signs of disease such as loss of appetite, arched back, and prostration, and determine when the animal reaches the endpoint criterion (>10% weight loss).

16. Euthanize the hamster with 5% isoflurane (see Current Protocols article: Donovan & Brown, 2001), harvest the kidneys aseptically, cut the kidney into four pieces. and place each piece in one tube containing 5 ml of EMJH base medium supplemented with 500 μl *Leptospira* enrichment EMJH. Incubate the tubes at 30°C up to 4 weeks to recover live virulent *Leptospira*.

17. Two to three days after euthanasia, remove the kidney tissue from the tube and return the culture to the 30°C incubator.
18. Monitor the cultures for live motile *Leptospira* weekly by observation under the DFM.
19. When *Leptospira* cultures reach cell density of $>10^7$ bacteria/ml, prepare DMSO stocks and freeze in −80°C (see steps 12 and 13) to save for later use.

Hamster passage 1 cultures frozen as DMSO stocks can be subcultured up to passage 4 in vitro without losing virulence; these subcultures are then used to prepare inoculum to infect mice.

Removing kidney tissue from EMJH culture after 3-4 days (before it starts to decay) allows for faster growth of Leptospira than leaving the tissues in the tube for 2-4 weeks.

INFECTION OF MICE THROUGH A PHYSIOLOGIC ROUTE AND COLLECTION OF CLINICAL SCORES AND BIOLOGICAL SAMPLES

In the protocols below, we describe how to infect mice using three physiologic routes of infection, how to keep records of weight (gain or loss), how to collect urine and blood from live mice, and how to collect tissues for analysis of pathogenesis after euthanasia. The basic protocol describes infection through transdermal abrasion (TD; Nair et al., 2020). Infection through other physiologic routes such as the conjunctiva (CJ; Sullivan et al., 2017) and nasal mucosa (NM; Nair et al., 2020) are presented as alternate protocols. Although described by others (Asoh et al., 2014), we did not succeed in infecting mice through the oral route (Nair et al., 2020). Thus, oral infection is not described.

In general, mice are anesthetized and inoculated with a prequantified dose of infectious *Leptospira*, the weight is recorded, and blood and urine are collected during 15-21 days. After euthanasia, blood and kidneys are collected, and other tissues, such as lung, liver, and spleen, may be collected for further analysis of pathogenesis.

Infection of mice via physiologic routes of infection

Natural transmission routes of infection are more appropriate to fully validate vaccines, therapeutics, and diagnostic assays for human and veterinary use. Here, we describe a main protocol for transdermal abrasion and two alternate physiologic infection routes. The standard laboratory practice of intraperitoneal inoculation (Richer, Potula, Melo, Vieira, & Gomes-Solecki, 2015) is added for comparative purposes. For experimental outcomes strictly dependent on infection dose, the intraperitoneal route is recommended. Materials specific to each infection route and the protocol steps are listed below.

NOTE: These infection protocols were established using *Leptospira interrogans* serovar Copenhageni strain Fiocruz L1-130 and C3H-HeJ mice older than 9 weeks. Other pathogenic *Leptospira* species may be used. If so, before proceeding with the entire protocol, consider doing a dose titration using 10^5-10^8 *Leptospira* for infection and PCR from urine as a readout to determine the best infection dose. Mice younger than 9 weeks can be used.

CAUTION: Biosafety Level 2 (BSL-2)/Animal Biosafety Level 2 (ABSL-2) procedures must be used for handling *Leptospira* cultures and infected mice. Personal protective equipment (PPE) needed: glasses or goggles, cap, mask, gloves, and gown.

NOTE: All animal experiments require approval by the local ethical and animal handling offices.

Definitions

TD = transdermal abrasion
CJ = conjunctival inoculation
NM = nasal mucosa inoculation

IP = intraperitoneal inoculation
BSC II = Class II biological safety cabinet

BASIC PROTOCOL 2

INFECTION OF MICE VIA TRANSDERMAL ABRASION

A transdermal abrasion protocol should be considered when questions arise regarding infection through wounded skin. The materials below are needed for infection via transdermal abrasion and for all of the infection routes described in the alternate protocols.

Materials

9-11 week old C3H/HeJ mice (The Jackson Laboratory)
Forane (Isoflurane, USP, Baxter, SKU cat. no. 10011936060)
Sterile alcohol pads
$\sim 10^8$ *L. interrogans* (see Basic Protocol 1) in 50 µl sterile PBS (Sigma-Aldrich, cat. no. TMS-012-A)

Somnosuite (Kent Scientific Corporation, cat. no. SS-01)
Hair clippers
Sterile razor blades
Sandpaper
Sterile non-adhesive gauze pads (Medique, cat. no. 64212)
Occlusive bandage (Curad, or any non-medicated adhesive bandage)
Disposable Animal Biosafety Level 2 (ABSL-2) mouse cages
10-, 20-, and 200-µl repeat pipettor and sterile tips (Rainin LTS)

Additional reagents and equipment for anesthesia (see Current Protocols article: Donovan & Brown, 2001) of rodents

1. Anesthetize mice with 4%-5% isoflurane for induction and 1%-2% for maintenance (see Current Protocols article: Donovan & Brown, 2001) using a Somnosuite.
2. Clip and shave a small area of fur (<1 in.^{2}) in the mouse dorsal area (to prevent grooming and scratching).
3. Clean the shaved area using alcohol pads and allow to dry. Use a sterile razor or sandpaper to gently scrape the skin while avoiding deep cuts and bleeding.
4. Add 25 µl of the *L. interrogans* culture (10^8 organisms/50 µl PBS) to the wound and allow the liquid to absorb and air dry. This process can be repeated until sufficient volume has been added to the wound to reach the required infection dose ($\sim 10^8$ for *L. interrogans*).
5. Cover the wound using sterile non-adhesive gauze pads and an occlusive bandage.
6. House mice individually in ABSL-2 cages for 8 days until the wound starts to heal.

   After 8 days, mice can be grouped in numbers of four per cage.
7. Monitor the wound three times on the day of the procedure to confirm that the occlusive bandage has not been removed, and then daily until termination (d15-21) to check for clinical signs of disease.

ALTERNATE PROTOCOL 1

CONJUNCTIVAL (CJ) INFECTION

Additional Materials *(also see Basic Protocol 2)*

3.34×10^9 *L. interrogans*/ml in sterile PBS (Sigma-Aldrich, cat. no. TMS-012-A)

1. Anesthetize mice in a Somnosuite with 4%-5% isoflurane for induction and 1%-2% for maintenance (see Current Protocols article: Donovan & Brown, 2001).
2. Using a 10-µl pipette tip, apply 10 µl of the 3.34×10^9 *Leptospira*/ml culture on the medial canthus of one eye; then add 10 µl of the culture in the other eye.

3. Gently massage the eyelids to spread the liquid evenly over the conjunctiva.
4. Allow enough time (~20 min) for the bacterial culture to be absorbed.
5. To attain the infection dose of $1-2 \times 10^8$ *L. interrogans*/mouse, repeat the above process for a total of three times per eye.
6. House mice in groups of four in ABSL-2 cages.
7. Monitor three times on the day of the procedure and then daily until termination (d 15-21) to check for clinical signs of disease.

NASAL MUCOSA (NM) INFECTION

ALTERNATE PROTOCOL 2

Additional Materials *(also see Basic Protocol 2)*

3.34×10^9 *L. interrogans*/ml in sterile PBS (Sigma-Aldrich, cat. no. TMS-012-A) (see Basic Protocol 1)

1. Anesthetize mice with 4%-5% isoflurane for induction and 1%-2% for maintenance (see Current Protocols article: Donovan & Brown, 2001).
2. Deposit 10 µl of sterile PBS containing *L. interrogans* as small drops into each nostril, synchronized with inhalation.

   The volume added per nostril has to be adjusted in order to attain a desired infectious dose.
3. House mice in groups of four in ABSL-2 cages.
4. Monitor mice daily until termination (d 15-21) to check for clinical signs of disease.

INTRAPERITONEAL (IP) INFECTION

ALTERNATE PROTOCOL 3

Materials

~10^6 to 10^8 *L. interrogans* in 60 µl sterile PBS (Sigma-Aldrich, cat. no. TMS-012-A)
25-G needles (BD, cat. no. 305122)

Additional reagents and equipment for anesthesia (see Current Protocols article: Donovan & Brown, 2001) and intraperitoneal injection (see Current Protocols article: Donovan & Brown, 2006b) of mice

1. Anesthetize mice with 4%-5% isoflurane for induction (see Current Protocols article: Donovan & Brown, 2001).
2. Using a 25-G needle, carefully inoculate 100-200 µl of PBS containing 10^6-10^8 *L. interrogans* into the peritoneal cavity of the mouse (see Current Protocols article: Donovan & Brown, 2006b).
3. House mice in groups of four in ABSL-2 cages.
4. Monitor mice daily until termination (d 15-21) to check for clinical signs of disease.

COLLECTION OF CLINICAL SCORES AND BIOLOGICAL SAMPLES AFTER INFECTION

SUPPORT PROTOCOL

Assessment of pathogenesis and immune responses induced by infectious *Leptospira* can be done after processing of clinical scores and tissues from mice, before and after euthanasia. From live mice, we collect weight records and urine daily, and blood every other day. We use weight loss as a clinical measurement of disease progression, and we quantify *Leptospira* load in blood and urine to estimate bacterial dissemination to target organs, colonization of the kidneys, and shedding. After euthanasia, blood, kidney, lung, liver, and spleen are collected.

Weight Measurement

Additional Materials *(also see Basic Protocol 2)*

Empty tip box or small bowl
Weighing balance (Fisher Science Education™ Portable Balances)

1a. Place an empty tip box/bowl on a scale and record its weight (tare).
2a. Place a mouse inside the tared box on the scale and record the weight daily for up to 15-21 days.

Urine Collection from Live Mice

Additional Materials *(also see Basic Protocol 2)*

Sterilized piece of aluminum foil (6-in. × 6-in.)
Transfer pipet or 200-µl repeat pipettor with tips
Labeled sterile 1.5-ml microcentrifuge tubes (e.g., Eppendorf)

1b. Transfer one cage into BSL-2 biosafety cabinet after sterilizing the surface.
2b. Spread a 6-in. × 6-in. size sterilized piece of aluminum foil inside the biosafety cabinet.
3b. Gently but effectively restrain one mouse within one hand and hold the animal directly above the aluminum foil.
4b. Gently massage the bladder area of the mouse until it urinates.

Female mice tend to urinate readily. Male mice comply with more difficulty.

Do not apply pressure while massaging to collect urine. If urine cannot be collected, put the mouse back in the cage and repeat the procedure after a couple of hours.

5b. Using a pipette collect the urine from aluminum foil into a sterile 1.5-ml micro-centrifuge tube.
6b. Store the urine in a −20°C freezer.

Blood Collection from Live Mice

Additional Materials *(also see Basic Protocol 2)*

Mouse Tailveiner restraint (Braintree Scientific Inc., cat. no. TV-150)
23-G needle (BD, cat. no. 305193)
Lancet
Capillary tubes (Thermo Fisher Scientific, cat. no. 22-260943)
Pipet bulb (Thermo Fisher Scientific, cat. no. 22-170-406)

1c. Restrain the mouse with its tail accessible for drawing blood.
2c. Use a 23-G needle to pierce the tail vein. Alternatively, a lancet can also be used to pierce the tail vein.
3c. Massage the tail gently and collect the blood using a capillary tube with a bulb.
4c. Centrifuge the tube and save the plasma/serum in an Eppendorf at −20°C.

Blood can be collected using a pipettor and sterile tips instead of a capillary tube; however, the capillary tube is much more efficient.

Up to 50 µl of blood is collected from the tail every other day until d 15-d 21 (max 150 µl per week).

Collection of Tissues After Euthanasia: Blood, Kidney, Lung, Liver, and Spleen

Additional Materials *(also see Basic Protocol 2)*

Heat-inactivated fetal bovine serum (FBS; Thermo Fisher Scientific, cat. no. 10-082-139)
Corning penicillin-streptomycin solution (Thermo Fisher Scientific, cat. no. MT30001CI)

RPMI 1640 medium (Thermo Fisher Scientific, cat. no. MT10041CV)
70% ethanol
RNA*later*™ (Thermo Fisher Scientific, cat. no. AM7021)
EMJH base medium (BD, cat. no. 279410)
Leptospira enrichment EMJH (BD Difco™, cat. no. 279510)
Neutral buffered formalin (Thermo Fisher Scientific, cat. no. 22-110-869)

15 -ml tubes (VWR, cat. no. 89039-664)
Sterile surgical equipment (scissors, scalpel, forceps, dissecting pins)
Instant sealing sterilization pouches (Thermo Fisher Scientific, cat. no. 01-812-55)
Sterile tissue culture petri dishes
Sterile 1.5-ml microcentrifuge tubes (e.g., Eppendorf) and 10-ml culture tubes

Additional reagents and equipment for euthanasia of mice (see Current Protocols article: Donovan & Brown, 2006a)

Humane endpoints and euthanasia

Mice are euthanized when weight loss reaches 20% unless they reach a depressed state (>15% weight loss plus ruffled fur plus loss of mobility) before losing 20% of weight.

1d. Euthanize mice (see Current Protocols article: Donovan & Brown, 2006a) by CO_2 asphyxiation or 5% isoflurane and exsanguination, and thoracotomy.

Collection of tissues

2d. Prepare complete RPMI 1640 medium by combining 50 ml of heat-inactivated FBS and 5 ml of penicillin-streptomycin solution in 445 ml RPMI 1640 medium. Aliquot 5 ml of into a sterile 15-ml tube and place it on ice.

3d. Spray the euthanized mouse with 70% ethanol, drain excess ethanol on a paper towel, and place it on its back on a styrofoam holder (the Styrofoam holder from a box of 50-ml conical Falcon-type tubes works well for this purpose). Pin down its four limbs in a cross format.

4d. Using sterile surgical scissors or a scalpel, cut an incision line from the navel to the top of the thorax, and with forceps, pull the skin and muscles aside (like opening a book) to access the organs in the thorax (lung) and peritoneal cavity (liver, spleen, and kidney).

Surgical equipment is sterilized by autoclaving in instant sealing sterilization pouches prior to euthanasia.

5d. Hold an organ (e.g., kidney) with forceps and cut the blood vessels to release it from the abdominal cavity. First, collect spleen into a tube with 5 ml RPMI complete medium, and store on ice until processing. Place each organ in a sterile tissue culture petri dish and cut in three or four fractions as needed (except spleen).

This work is done under aseptic conditions.

6d. Place one third of each organ (lung, liver, kidney) in a microcentrifuge tube containing 0.5-1 ml (ideally 10 µl per mg tissue) of RNA*later*™ and freeze for purification of *Leptospira* DNA. Place one third of each organ in another microcentrifuge tube containing 0.5-1 ml of RNA*later*™ and freeze at −80°C to process for mRNA purification for assessment of inflammatory mediators (e.g., cytokines, fibrosis markers). Finally, place the remaining one third of the organ in a sterile 10-ml tube containing 7 ml of EMJH medium supplemented with 500 µl of *Leptospira* enrichment EMJH to culture *Leptospira*.

7d. Place the other kidney in neutral buffered formalin for histopathology staining and for immunohistochemistry.

Kidney can also be collected for analysis of single cells as described in Basic Protocol 3 for spleen (Evaluation of the host humoral and cellular immune responses to Leptospira infection).

BASIC PROTOCOL 3

ANALYSIS OF PATHOGENESIS AFTER *LEPTOSPIRA* INFECTION

In this protocol, we first describe which techniques to use to evaluate dissemination of *Leptospira* in blood, urine, and target tissues such as lung, liver, and kidney. We use qPCR for bacterial load quantification and culture of tissues to assess *Leptospira* viability. Second, we describe the techniques that we use to evaluate molecular, cellular, and histologic differences that allow for determination of pathogenesis after *Leptospira* infection. Classic histologic staining and immunohistochemistry techniques are used to evaluate histopathology and typing of immune cell infiltrates in the kidney; inflammation of the target organ (kidney) is accessed by quantification of immune markers (chemokines, cytokines, fibrosis markers) by RT-PCR and by flow cytometric analysis of the kidney; and, lastly, immunoassays and flow cytometry are used to evaluate the host's antibody and cellular immune responses to *Leptospira* infection from serum and spleen, respectively.

Definitions

ELISA = enzyme-linked immunosorbent assay
HRP = horseradish peroxidase
RT = room temperature (20°C-25°C)
PCR = polymerase chain reaction
RT-PCR = reverse-transcriptase polymerase chain reaction
TAMRA = 6-carboxyfluorescein–6-carboxytetramethylrhodamine
H&E = Hematoxylin and Eosin
PAS-D = Periodic Acid Schiff Diastase

CAUTION: Biosafety Level 2 (BSL-2)/Animal Biosafety Level 2 (ABSL-2) procedures must be used for handling *Leptospira* cultures and infected mice. Personal protective equipment (PPE) needed: glasses or goggles, cap, mask, gloves, and gown.

NOTE: All animal experiments require approval by the local ethical and animal handling offices.

Materials

Tissues collected from euthanized, *Leptospira*-infected mice (see Support Protocol, steps 6d and 7d)
DNeasy Blood & Tissue Kit (Qiagen, cat. no. 69506)
NucleoSpin® Tissue Kit (Takarabio USA Inc., cat. no. 740952.250)
Leptospira-specific TAMRA probe and 16S rRNA primers (Eurofins Scientific)
RNeasy Mini Kit (Qiagen, cat. no. 74106)
RNase inhibitor (Applied BiosystemsTM, cat. no. 4374967)
RNase-free DNase (Qiagen, cat. no. 79254)
High-Capacity cDNA Reverse Transcription Kit (Thermo Fisher Scientific, cat. no. 4368814)
TAMRA probe and primers: sequences in Table 1
Maxima Probe/ROX qPCR Master Mix (2×) (Thermo Fisher Scientific, cat. no. K0233)
Neutral buffered formalin (Thermo Fisher Scientific, cat. no. 22-110-869)
Culture of $>10^8$ *Leptospira*/ml (see Basic Protocol 1)
10× phosphate-buffered saline (PBS; Thermo Fisher Scientific, cat. no. BP399-500)
Modified Lowry Protein Assay Kit (Thermo Fisher Scientific, cat. no. PI23240)

1× coating buffer: add 10.6 g of sodium carbonate (anhydrous) to 100 ml of distilled water; adjust the pH to 9.5; make up total volume to 1 L

Alternatively, purchase 5× carbonate buffer (VWR, cat. no. 421701-BL) and dilute 1:5 to make 1× buffer (i.e., 1 ml of 5× buffer in 4 ml deionized water)

Washing buffer: PBST (1× PBS containing 0.05% Tween; add 100 ml of 10× PBS to 900 ml of distilled water. then add 500 µl of Tween 20)

Alternatively, purchase 10× PBS/0.5% Tween (Thermo Fisher Scientific, cat. no. AAJ63596K3) and dilute to 1×

Blocking buffer: 1× PBST + 1% BSA (Thermo Fisher Scientific, cat. no. BP9704100), prepared fresh daily: add 500 mg of BSA to 50 ml of washing buffer

Serum samples (prepared from blood taken in the Support Protocol)

Goat anti−mouse IgG (H+L) secondary antibody, HRP (Jackson ImmunoResearch, cat. no. 115-035-146)

Peroxidase AffiniPure F(ab')$_2$ fragment goat anti−mouse IgM, µ-chain-specific (Jackson ImmunoResearch, cat. no. 115-036-020)

TMB SureBlue Microwell Peroxidase Substrate (Thermo Fisher Scientific, cat. no. 5067497 or Seracare Life Sciences, cat. no. 51200083)

TMB stop solution (VWR, cat. no. 95059-200)

Spleen in RPMI medium (see Support Protocol, "d" steps)

1× ACK lysing buffer (Thermo Fisher Scientific, cat. no. BW10548E)

RPMI 1640 medium (Thermo Fisher Scientific, cat. no. MT10041CV)

Fetal bovine serum, (FBS; R&D systems, cat. no. S11150)

Nexcelcom Bioscience acridine orange (AO)/propidium iodide (PI) viability stain (Thermo Fisher Scientific, cat. no. NC0285242)

Staining buffer: 1× DPBS (Thermo Fisher Scientific, cat. no. 14-190-144) containing 3% heat-inactivated FBS)

Fc block: Ultra-LEAF™ Purified anti-mouse CD16/32 Antibody (BioLegend, cat. no. 101329)

CD3 clone 17A2 conjugated with fluorescein isothiocyanate (FITC; Tonbo Biosciences, cat. no. 35-0032-U100)

CD4 clone RM4-5 conjugated with phycoerythrin (PE; Tonbo Biosciences, cat. no. 50-0042-U100)

CD8 clone 53-6.7 conjugated with allophycocyanin (APC)-Cy7 (Tonbo Biosciences, cat. no. 25-0081-U100)

CD62L clone MEL-14 conjugated with PE-Cy7 (Tonbo Biosciences, cat. no. 60-0621-U100)

CD44 clone IM7 conjugated with APC (BioLegend, cat. no. 103012)

CD19 clone 1D3 conjugated with PE (Tonbo Biosciences, cat. no. 50-0193-U100)

4% paraformaldehyde in PBS (Thermo Fisher Scientific, cat. no. J19943K2)

Invitrogen™ UltraComp eBeads™ (Thermo Fisher Scientific, cat. no. 50-112-9040)

Nanodrop One microvolume UV/Vis spectrophotometer (Thermo Fisher Scientific, cat. no. 84-027-42PR20)

MicroAmp™ Fast Optical 96-Well Reaction Plate with Barcode, 0.1 ml (Thermo Fisher Scientific, cat. no. 4366932)

StepOnePlus™ Real-Time PCR System (Thermo Fisher Scientific, cat. no. 4376600)

15-ml tubes (VWR, cat. no. 21008-216)

15-ml tubes (VWR, cat. no. 89039-664)

Axio Zeiss Imager A1 light microscope

Refrigerated centrifuge

Dark-field microscope (DFM; Zeiss, USA)

2.0-ml microcentrifuge tubes (VWR cat. no. 20170-170)
Heat block
–80°C Freezer
MaxiSorp™ flat-bottom 96-well plate (Nunc, cat. no. 44-2404-21)
ELISA plate washer: Fisher AccuWash 96 (Thermo Fisher Scientific, cat. no. 14 377 577)
Wypall paper towels (Thermo Fisher Scientific, cat. no. 15-235-83)
Multichannel pipettor and tips
Polystyrene reservoirs, 50 ml, sterile (VWR, cat. no. 89094-680)
SpetramaxPlus ELISA reader (Molecular Devices) or another ELISA reader
50-ml tubes (VWR, cat. no. 89039-656)
Petri dish–60 mm × 15 mm (VWR, cat. no. 25384-092)
Fisherbrand™ Frosted slides (Thermo Fisher Scientific, cat. no. 12-550-343)
70-μm-pore-size and 40-μm-pore-size nylon filters (BD Falcon, cat. no. 22-363-548 and 22-363-547)
Luna-FL automated cell counter (Logos Biosystems)
96-well plate, V-bottom, polypropylene (Millipore Sigma, SKU cat. no. M8185-100EA)
LSR II flow cytometer (BD Immunocytometry Systems)
ZE5 Cell Analyzer (Bio-Rad)

qPCR and RT-PCR

We use qPCR for quantification of *Leptospira* load in tissues and cultures of organs.

We use RT-PCR to quantify immune markers of infection in tissues.

1. Extract DNA from blood, urine, kidney (20-25 mg) and other tissues using DNeasy Blood & Tissue Kit and NucleoSpin tissue kit according the manufacturer's instructions.
2. Quantify *Leptospira* using a TAMRA probe and primers (Table 1) to *Leptospira* 16S rRNA by qPCR as described in Basic Protocol 1, steps 7–11.
3. Extract total RNA from 15-20 mg of tissue using an RNeasy Mini kit following the manufacturer's protocol for on-column DNase digestion. Quantify and analyze the RNA for purity by loading 2 μl onto the Nanodrop One and measuring absorbance (A) at 260, 280, and 230 nm. RNA is considered to be pure if the ratio of $A_{260/280}$ is ~2 and $A_{260/A230}$ is in the range of 2.0-2.2.
4. Reverse transcribe 1 μg of RNA using a high-capacity cDNA reverse transcription kit, with RNase inhibitor, in a 20-μl reaction according to the manufacturer's protocol. Place tubes on the thermal cycler using the reaction conditions recommended by the cDNA Reverse Transcription Kit.
5. Set up the PCR reaction for the target gene using primers and TAMRA probes described in Table 1: add 2 μl of cDNA per well of a MicroAmp™ Fast Optical 96-Well Reaction Plate previously loaded with 18 μl of master mix per well [as per reaction conditions recommended by the Maxima Probe/ROX qPCR Master Mix (2×)]. A no-template control (NTC) without DNA is used as a negative control. All samples are run in duplicate using comparative Ct method.

   An additional step of DNase digestion is performed, according to manufacturer's instructions, while performing RNA purification. DNase digestion will ensure that the purified RNA is free from genomic DNA contamination, and that the results of gene expression obtained are from the cDNA and not due to the presence of genomic DNA.

PCR data are reported as the relative increase in mRNA transcript levels of a given marker corrected for by the respective levels of β-actin.

Histopathology and immunohistochemistry of the kidney

Histologic staining involves fixation, processing, embedding, sectioning, and staining or immunostaining (Alturkistani, Tashkandi, & Mohammedsaleh, 2016), all of which require ultra-specialized equipment. For this reason, we use the services of Research Histology Core facilities (UTHSC and Vanderbilt University) to acquire histologic and immunohistochemistry data. These services are commonly offered by major U.S. universities. The only techniques we perform in the laboratory are fixation of the tissue after harvest from the mouse and scoring of histopathology and immunohistochemistry analysis after we receive the stained slides. For resources on how to perform classic histology and immunohistochemistry techniques in the laboratory, consult Junqueira's Basic Histology: Text and Atlas (Mescher, 2018).

6. For fixation, place the tissue in a 15-ml tube containing 10% neutral buffered formalin.
7. Submit/ship the material to the Histology Research Core
8. Determine histopathology and immunohistochemistry scores as follows:

   H&E or PAS-D: Measure the glomeruli size in five fields per sample, and average groups. Grade nephritis scores blindly on a scale of 0-5 in a longitudinal section of the organ following previously published criteria (Chan, Madaio, & Shlomchik, 1997).

   An example of PAS-D staining is shown in Figure 2.

   Masson trichrome: Digitally analyze (40×, Photoshop) five randomly chosen fields as a percentage of pixels of the total area.

   An example is shown in Figure 3. Masson's trichrome staining is very sensitive to processing of the tissue before and after staining. It should only be performed between groups of the same experiment by experienced personnel.

   Immunohistochemistry: Count positive cells/total cells per antibody marker in 10 randomly chosen fields (400×) from the cortex and medulla of kidney. At least two

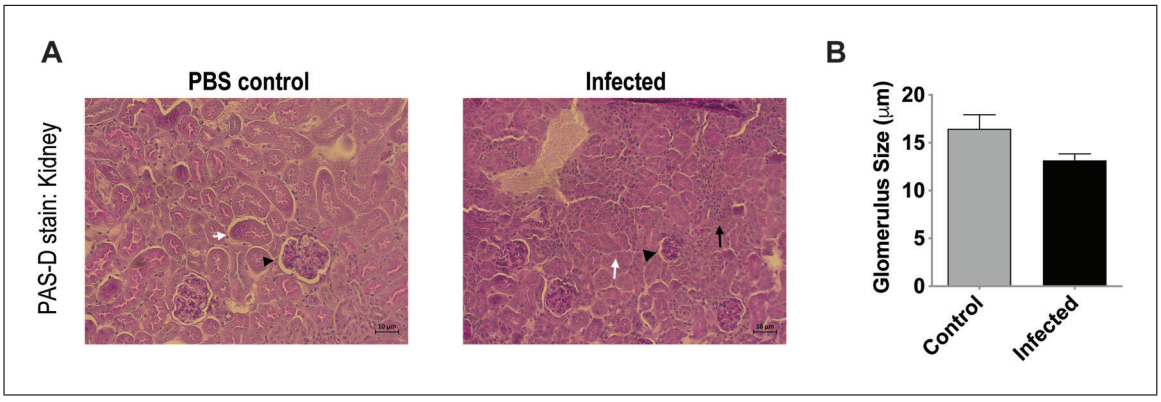

Figure 2 Histopathology of the kidney. (**A**) PAS-D staining showing shrinkage of glomeruli, infiltration of immune cells, and loss of tubular structure in the infected group (20×); (**B**) diameter of glomeruli is measured under 20× using a measurement function (e.g., CaptaVision Software). Legend: white arrow, tubules; black arrow, infiltration of immune cells; black triangle, glomerulus (Sullivan et al., 2017).

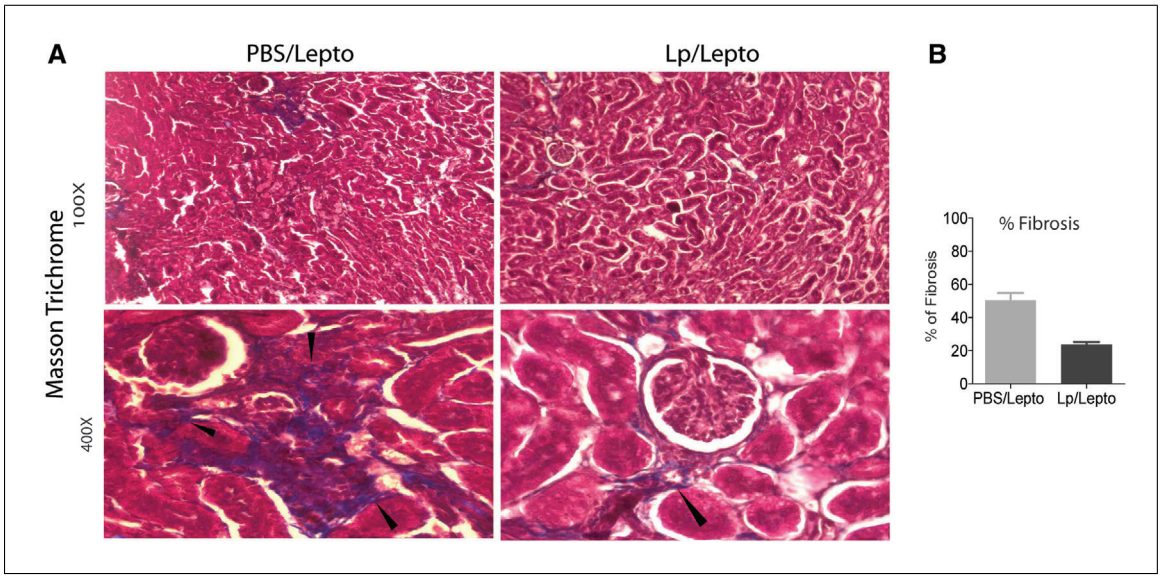

Figure 3 Histopathology of the kidney. (**A**) Masson trichrome staining of kidney sections from infected mice pre-treated with PBS and with *Lactobacillus plantarum*. (**B**) Digital quantification of fibrosis was determined as the % area (pixels) where blue staining exceeds a threshold. The slides were processed and stained in parallel, and images where taken using the same illumination (Potula et al., 2017).

sections per kidney are counted for each experiment. Acquire images at 200×, or 400× using a Zeiss microscope with ZEN software.

An example is shown in Figure 4.

Evaluation of the host humoral and cellular immune responses to Leptospira infection

The immune response to *Leptospira* is evaluated by quantification of *Leptospira*-specific antibodies in serum and by analysis of immune cell populations by flow cytometry of single cell suspensions (spleen) and other techniques to determine signatures of gene expression.

Serological analysis of immunoglobulins

We use ELISA to evaluate immunoglobulin class and isotype and to quantify total antibody as well as *Leptospira*-specific antibody in the serum of infected mice. Quantification of total antibody and determination of IgG isotype in serum is done using the Ready-Set-Go enzyme-linked immunosorbent assay (ELISA) [Thermo Fisher Scientific, cat. no. 88-50400-22 (IgG) and 50-246-320 (IgM)] and kits for IgG1, IgG2a, and IgG3 (Thermo Fisher Scientific, cat. no. 88-50410-22, 88-50420-22, and 88-50440-22, respectively) according to the manufacturer's instructions. Determination of IgM- and IgG-specific antibodies to *Leptospira* is done by ELISA using heat-killed *Leptospira* or purified recombinant proteins as antigens to coat a 96-microwell plate.

Production of heat-killed Leptospira antigen

9. Centrifuge 5 ml culture of *Leptospira* (10^8/ml) 10 min at 12,000 × *g*. Discard the supernatant.
10. Wash pellet with 5 ml PBS, then centrifuge 10 min at 12,000 × *g*.
11. Count the cells under DFM. Adjust to 10^7-10^9 cells/ml with PBS.
12. Aliquot 1 ml of bacteria into 2-ml tubes.

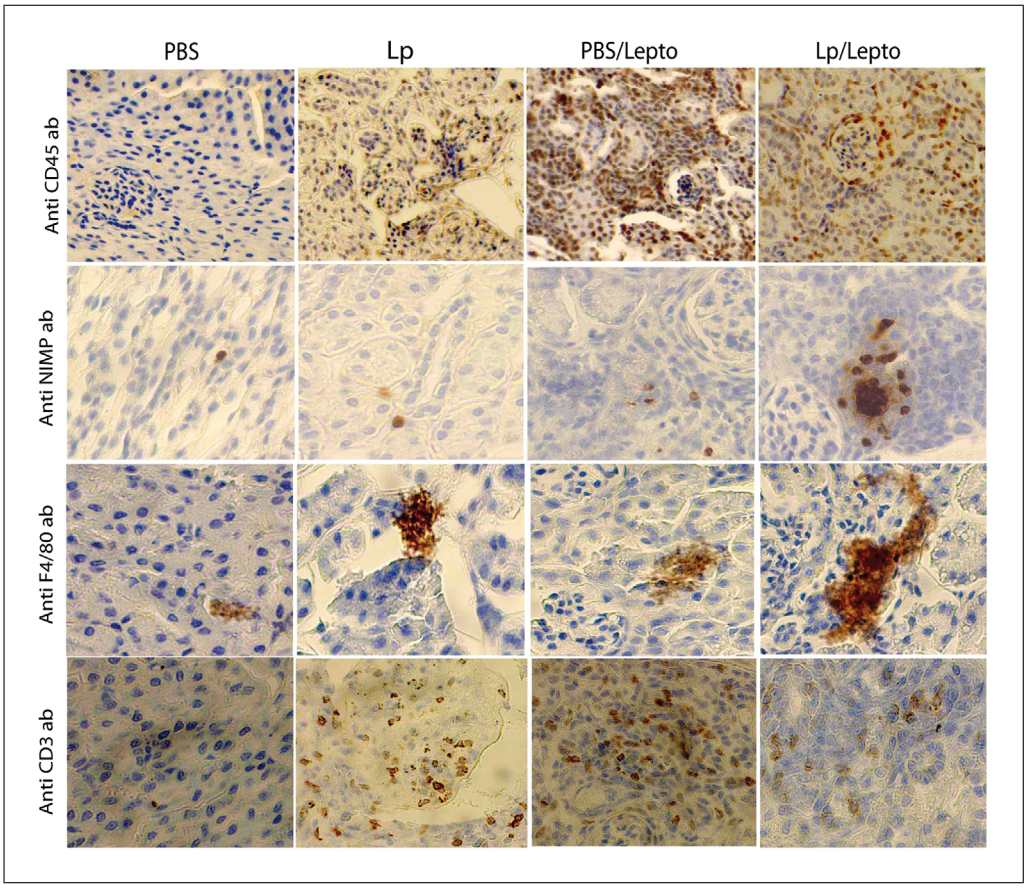

Figure 4 Immunohistochemistry of the kidney. Immunostaining of kidney sections from groups of treated mice in the presence or absence of *Leptospira* infection using various leucocyte markers (CD45+, NIMP-R14+, F4/80+, and CD3+) (Potula et al., 2017).

13. Subject *Leptospira* to heat killing for 15 min at 95°C. Heat killing is confirmed by checking under the DFM: no motile *Leptospira* are expected to be visible.

    If motile Leptospira are visible under DFM, the process is repeated until no motile Leptospira are observed (up to three times over 1 hr).

14. Determine the protein concentration using the Modified Lowry Protein Assay Kit according to the manufacturer's protocol.

Quantification of Leptospira-specific antibody (IgM and IgG) in serum

15. Coat a plate with antigen as follows. Dilute heat-killed *Leptospira* in 1× coating buffer to a final concentration of 1×10^5-10^8/well or 100 µl/well of 4 mg/ml of heat-killed *Leptospira* in a flat-bottom 96-well plate. Cover the plate and incubate overnight at 4°C.

    This protocol can be modified to test antibody levels against recombinant proteins as antigens. Instead of heat-killed Leptospira, coat the plates with 0.1-1 µg/ml of the proteins in coating buffer in step 15 and follow the protocol from step 16.

16. Next morning wash the plate using the ELISA plate washer and run a total of four washes with 300 µl washing buffer.

17. *To block the plate:* Pour blocking buffer into a new reagent reservoir and add 250 µl of blocking buffer (1× PBST+ 1 %BSA; prepare fresh) in each well (using a multichannel pipet) and incubate for 1-2 hr at room temperature or 37°C.

    If a plate washer is not available, use a multichannel pipettor to dispense 300 µl of washing buffer per well, dump the washing buffer into a sink. and tap dry over a layer of 3-4 clean paper towels.

At this point, the plate can be stored at 4°C for maximum of 2 days (cover the plate or put plate inside a ziplock bag). Otherwise, continue following the protocol.

18. Wash the plate two times with 300 µl washing buffer. Tap dry over a layer of 3-4 clean paper towels.

19. Dilute the serum samples 1:100 in blocking buffer, add 100 µl of diluted serum sample to each well of the Test plate, cover the plate, and incubate for 1.5 hr at room temperature or 1 hr at 37°C.

20. Wash the Test plate four times; tap dry over a layer of 3-4 clean paper towels.

21. *Clean the plate washer:* Dip the wash head in washing buffer (1×PBST) in the blue boat provided with the instrument and run a Wash plate twice to remove any primary sera sticking to the wash head.

    We use two 96-well plates to run the enzymatic reaction: one is labeled Test plate and contains the serum samples subject to study; the second plate is a Wash plate used to clean up the plate washer instrument after the washes.

22. Dilute the secondary antibody-HRP (IgM or IgG) in blocking buffer and pour this into a new reagent reservoir. Add 100 µl to the wells of the Test plate using a multichannel pipettor. Cover the plate and incubate 1 hr at room temperature or 37°C for 30 min.

23. Wash the Test plate four times on the plate washer; tap dry over a layer of 3-4 clean paper towels.

24. *Clean the plate washer:* Dip the wash head in 1×PBST in the blue boat provided with the instrument and run a Wash plate with the "2 wash" program to remove any HRP-conjugated antibody sticking onto the wash head.

25. Add 100 µl of TMB SureBlue substrate at room temperature into each well of the Test plate using a multichannel pipettor.

26. Cover the plate and incubate for 15 min at room temperature or 37°C.

27. Add 100 µl of TMB Stop Solution into each well and read the absorbance at 450 nm in the SpectraMax ELISA reader; save the file and export the raw data as an `.xls` file for analysis.

28. Connect the washer to the MilliQ bottle and run a wash cycle with MilliQ water.

    If the instrument is left in buffer, solutes form deposits and block the tubing.

    Before starting the enzymatic reaction part of this protocol, aliquot the volume of TMB SureBlue required for the ELISA in a 50-ml tube and keep it at room temperature covered in foil (TMB substrate is light sensitive and is to be used at room temperature).

Profiling immune cell populations (T and B cells) by flow cytometry

Cellular immune responses to *Leptospira* infection are studied in our laboratory by profiling immune cell populations (T and B cells) by flow cytometric analysis of single cells isolated from spleen. Quantification of signatures of gene expression produced by immune cells can also be done using a T-Cell & B-Cell Activation RT^2 Profiler PCR Array (Qiagen, PAMM-053Z) according to the manufacturer recommendation.

Cell preparation

29. Transfer spleen and the complete RPMI medium from the 15-ml tube to a petri dish.

30. Tease the spleen with frosted slides to produce single cell suspensions.

31. Centrifuge 4 min at 453 × *g*, at 4°C. Discard the supernatant.

32. Add 2 ml/spleen of 1× ACK lysing buffer to lyse red blood cells and let stand for 2 min. Stop the reaction by adding 3-5 ml of RPMI 1640 containing 10% heat-inactivated fetal bovine serum.

33. Wash the cells in RPMI 1640 containing 10% heat-inactivated fetal bovine serum, followed by passage through 70-μm pore-size and 40-μm pore-size nylon filters

34. Count the cells using a Luna-FL automated cell counter.

Flow cytometric cell staining

35. Analyze cell viability by mixing 18 μl of splenocyte suspension obtained in step 33 with 2 μl of acridine orange−propidium iodide staining solution in the Luna-FL automated cell counter.

36. Stain 1−5 × 10^6 live cells per well of a 96-well V-bottom plate:

    a. Incubate cells in 0.5-1 μg Fc block (Ultra-LEAF™ Purified anti-mouse CD16/32 antibody) for 15 min at 4°C in staining buffer, wash twice with staining buffer, each time centrifuging 4 min at 453 × *g*, 4°C, and incubate with the appropriate marker for surface staining in the dark for 30 min at 4°C.

    InvitrogenTM UltraComp eBeadsTM are also stained using each of the conjugates (used for surface staining) separately to create compensation controls.

    b. The following are the surface markers used for T cell panel:
    CD3 clone 17A2 conjugated with fluorescein isothiocyanate (FITC) (1:200)
    CD4 clone RM4-5 conjugated with phycoerythrin (PE) (1:150)
    CD8 clone 53-6.7 conjugated with allophycocyanin (APC)-Cy7 (1:150)
    CD62L clone MEL-14 conjugated with PE-Cy7 (1:150)
    CD44 clone IM7 conjugated with APC (1:150)
    Pacific blue as the dump channel.

    c. The following are the surface markers used for the B cell panel:
    CD3 clone 17A2 conjugated with fluorescein isothiocyanate (FITC) (1:200)
    CD19 clone 1D3 conjugated with PE (1:150).

Stain control beads and cells using the same dilution. Wash cells twice in staining buffer.

37. *Fixation with 4% paraformaldehyde (optional):* Wash the cells with staining buffer, centrifuge 4 min at 453 × *g*, 4°C, and resuspend in 0.5 ml of 4% paraformaldehyde solution. Incubate the cells for 15 min at room temperature and wash with 1× PBS. Resuspend the cells in 1× PBS and store at 4°C until analysis.

38. For flow cytometry, acquire cells on an LSR II flow cytometer equipped with 405, 488, 561, and 640 nm excitation lasers or a ZE5 Analyzer.

39. Collect data using BD FACSDiva software (BD Biosciences) for LSRII, or Everest software for ZE5 analyzer.

    The cells fixed with 4% paraformaldehyde solution can be stored up to a couple of days (at 4°C in the dark) for analysis.

COMMENTARY

Background Information

Although *Leptospira* are not considered Gram-negative, they do produce lipopolysaccharide (LPS), a potent inflammatory cell wall component. In human cells, *Leptospira* LPS signals through TLR2 rather than the conventional TLR4 signaling system (Nahori et al., 2005, Werts et al., 2001). However, in mice, signaling occurs through TLR2 as well as TLR4 (Nahori et al., 2005). Mice can tolerate levels of LPS endotoxin 250 times higher than humans (Copeland et al., 2005), which makes them excellent reservoir hosts for a number of human pathogens, including *Leptospira*. For

this reason, infection doses in mice have to be at least 2-3 logs higher than infectious doses in higher-phylum vertebrates like humans. The *sine qua non* condition for a reservoir host is to remain persistently infected with the pathogen that it maintains in the enzootic cycle. Transmission to sylvatic rodents results in asymptomatic infection (Ko, Goarant, & Picardeau, 2009). In the first studies in which inbred mice were tested, Balb/c did not develop evident clinical signs of leptospirosis (Adler & Faine, 1976, 1977). Thus, asymptomatic infection was conflated with resistance to infection, and as such, mice were not considered suitable models of leptospirosis. However, the concept of resistance to infection is at odds with the mouse's role as a reservoir host of *Leptospira*. To fulfil its role as reservoir host, the mouse immune system must allow the spirochete to disseminate to tissues and be shed in urine. Mice infected with bioluminescent *L. interrogans* followed for 5 months developed chronic leptospirosis (Ratet et al., 2014). Others showed that although infection of inbred mice did not result in lethal infection, some strains developed pathology indicative of subclinical infection (Santos et al., 2010). To break the reservoir-host tolerance of lipopolysaccaride (LPS), high doses of pathogenic *Leptospira* are used, and $>2 \times 10^8$ *Leptospira interrogans* ser. Copenhageni can lead to lethality of adult C57BL/6 KO (Chassin et al., 2009) and C3H-HeJ mice (Fig. 5).

We chose the C3H/HeJ strain rather than C57BL/6 used by others (Chassin et al., 2009; Fanton d'Andon et al., 2014; Ratet et al., 2014; Santos et al., 2010) because C3H-HeJ have a point mutation (aa712, P to H) in their *tlr4* coding region (Vogel et al., 1999). This mutation leads to impaired TLR4 recognition, which renders these mice hyporesponsive to *Leptospiral* LPS. Thus, a substandard immune response to infection should lead to dissemination of greater numbers of *Leptospira* to tissues. This factor facilitates establishment of an animal model of infection that allows for consistent measurement of significant differences between infected and uninfected mice (Nair et al., 2020, Potula, Richer, Werts, & Gomes-Solecki, 2017, Richer et al., 2015, Sullivan et al., 2017). We adapted the C3H-HeJ lethal model previously used by Pereira and colleagues (Pereira, Andrade, Marchevsky, & Ribeiro dos Santos, 1998), Nally and colleagues (Nally, Fishbein, Blanco, & Lovett, 2005), and Vinetz and colleagues (Viriyakosol, Matthias, Swancutt, Kirkland, & Vinetz, 2006), but, rather than infecting young 4-week-old mice, we infected adult mice at ~10 weeks of age (Richer et al., 2015) because the mouse immune system is functional after 5 weeks of age (Landreth, 2002). Thus, infection at 10 weeks allows for inclusion of a 5-week vaccination schedule before challenge is performed. Measurable clinical indicators of infection can be obtained in the form of weight loss, bacterial load in blood and urine over time, bacterial colonization of target tissues (such as kidney), and expression of certain inflammatory cytokine and chemokine genes in kidneys of infected mice. In addition, this model allows for analysis of the host's antibody and cellular immune response to infection. Once the basic mouse model was developed using the standard laboratory intraperitoneal route of infection, we proceeded to adapt the model to infection via natural transmission routes such as ocular conjunctiva, transdermal abrasion, and nasal

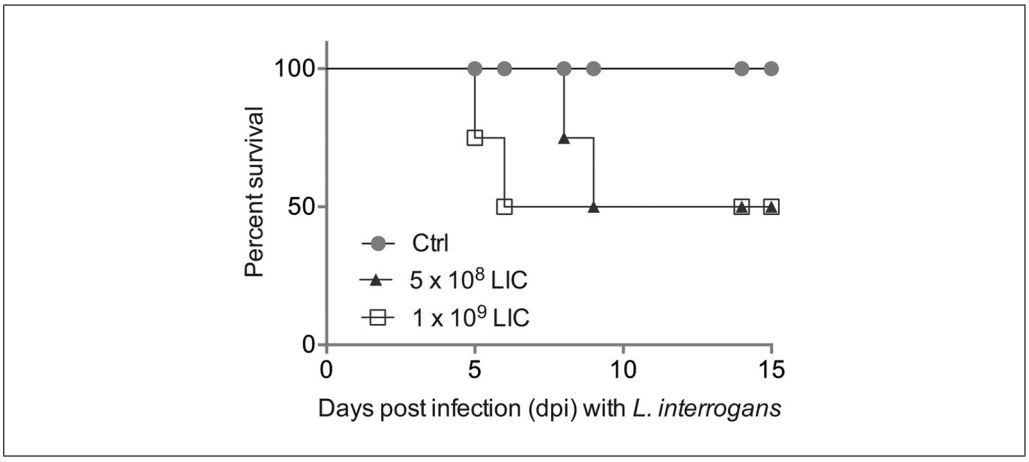

Figure 5 Susceptibility to lethal leptospirosis (LD50) in C3H-HeJ mice inoculated with PBS (Ctrl), 5×10^8 and 1×10^9 *Leptospira interrogans* ser. Copenhageni FioCruz. $N = 4$ mice per group.

mucosa. The latter routes of infection are more appropriate to fully validate vaccines, therapeutics, and diagnostic assays for human and veterinary use.

One of the drawbacks of the C3H-HeJ mouse model is that, due to the point mutation in TLR4, this mouse is considered immunocompromised. The analogous hyporesponsiveness and non-resposiveness of C3H-HeJ and human TLR4 to *Leptospira* LPS led us to use humanized TLR4 transgenic C57BL-6J mice to develop an immunocompetent mouse model of Leptospirosis (Nair, Soares Guedes, Hajjar, Werts, & Gomes-Solecki, 2020). Either using C3H-HeJ or humanized TLR4 C57BL-6J, these mouse models of infection can only help increase our knowledge of *Leptospira* pathogenesis if they are adopted by the research community.

Critical Parameters

Handling pathogenic *Leptospira* requires strict adherence to BSL-2 protocols to protect laboratory personnel from exposure. In the animal facility, disposable ABSL-2 mouse cages should be used. Since *Leptospira* is a slow-growing bacterium, aseptic techniques must be employed when harvesting tissues, to prevent contamination. The genetic background of the mouse (C3H-HeJ, C57BL/6, Balb/c) will affect the results observed. The age of the mice is known to affect the kinetics of disease progression (Nally et al., 2005; Richer et al., 2015). We found that male hamsters are more susceptible to lethal infection than their female counterparts (Gomes, Guedes, Potula, Dellagostin, & Gomes-Solecki, 2018). Although we have not repeated these experiments using mice, it is reasonable to expect that male mice could be more susceptible to leptospirosis. Furthermore, it is considerably more difficult to collect urine from male than female mice. The dose of inoculum and route of infection, i.e., intraperitoneal versus transdermal versus nasal versus conjunctival, are known to affect the timing and load of bacteria present in the blood, urine, and tissues. The number of days from infection to termination is known to affect bacterial load in tissues, gene expression, and immune cell profiles.

Troubleshooting

One of the issues that frequently delay initiation of experiments is that *Leptospira* is a slow-growing fastidious bacterium. It is common not to be able to see bacteria under a dark-field microscope using 20× and 40× magnification within 3-5 days of inoculation. Depending on the species and serovars, cultures take from 1-3 weeks to grow. Occasionally, after inoculation of a frozen stock/kidney culture, a coiled/dot form of bacteria can be observed. Provided that there is no contamination of the culture, the dot forms change into spirochetal forms over time. We use PCR over two time points to quickly determine if we have a live culture (e.g., d5 and d10 post inoculation). The growth rate depends on the number of live bacteria in the inoculum. Preparing single-use DMSO stocks to avoid multiple freeze-thaw cycles from the same master stock will ensure reproducible cultures. To ensure maintenance of virulence in mice, infect animals with cultures up to passage 4 (subculture in medium) of *Leptospira* (from the initial hamster stock). All experiments performed must be repeated with the culture from the same passage number. Thus, when preparing inoculum, plan for growing enough culture to save stocks for three experiments. We found that the physiologic route of infection most difficult to reproduce was transdermal abrasion, because of the need to use proper technique to create the wound, and that the intranasal route was the easiest. In case of failure to infect mice using the transdermal route, this can be resolved by requesting assistance from the animal facility's attending veterinarian.

Understanding Results

If the steps of the three basic protocols are followed, one should expect to obtain the following results

Basic Protocol 1: Full confluent cultures ($>10^8$) take from 1-3 weeks to grow depending on the species and serovar used. For example, a 1-week culture of *L. interrogans* will show a few cells per field under a dark-field microscope; a 2-week culture should be about 10^6-10^8 cells/ml. For maintenance of virulent *Leptospira*, hamsters infected intraperitoneally with 5000 *L. interrogans* should reach the endpoint criterion (>10% weight loss) 8-10 days post-infection. At this point, animals should be euthanized and kidney cultured to retrieve virulent *Leptospira*.

Basic Protocol 2: Infection of mice through a physiologic route. Weight loss should be observed between days 10 and 12 after inoculation; *Leptospira* should be detected in blood between days 1 and 7 post infection, and shedding in urine is expected to start 6-8 days post infection. In kidney, we usually detect $\sim10^4$ *Leptospira*/mg of tissue. Differences in transdermal and conjunctival infection should be seen within 15 days of infection against the

uninfected control, whereas intranasal infection benefits from a longer schedule, up to 21 days.

Basic Protocol 3: Analysis of pathogenesis after *Leptospira* infection. The following inflammatory markers should be increased in the kidney after infection (KC, MIP-2, RANTES, TNF-α, IFN-γ), as well as the antimicrobial iNOS and the fibrosis marker ColA1. Classic tissue staining techniques allow for visualization of *Leptospira* in the renal tubules (silver stain) and for evaluation of *Leptospira*-induced inflammation of the kidney (hematoxylin and eosin, H&E; periodic acid Schiff diastase, PAS-D, and Masson's trichrome) under a light microscope. Using H&E or PAS-D, we can visualize interstitial infiltration of immune cells and score tissue damage such as reduced glomerular size and tubular anomalies in *Leptospira*-infected kidney (Richer et al., 2015). We use Masson's trichrome staining of kidney sections to evaluate interstitial collagen deposition (fibrosis) (Ferrer et al., 2014, Potula et al., 2017). Immunohistochemistry requires labeling specific cell markers with antibodies. We use antibodies specific for total leukocytes (anti-CD45), neutrophils (anti-NIMP-R14), macrophages (anti-F4/80), and T cells (anti-CD3) to identify these immune cell populations in kidney cryosections (Potula et al., 2017). With regard to *Leptospira*-specific antibody, both IgM and IgG are expected to be increased 2 weeks post infection. With regard to profiles of immune cell populations, increased effector CD3+/CD4+ T cells and decreased CD3+/CD8+ populations and no difference in memory T cells in single-cell suspensions from spleen at 2 weeks post-infection should be expected.

Time Considerations

Basic Protocol 1: Growing *Leptospira* cultures will take between 1 and 4 weeks depending if starting from a frozen stock (up to 4 weeks) or passaging subcultures (∼1 week).

Basic Protocol 2: Infection of mice by transdermal, conjunctival, and intraperitoneal inoculation can be done following a 15-day schedule, but nasal mucosal infections benefit from longer infection schedules, until day 21.

Basic Protocol 3: Acquisition and analysis of pathogenesis data can take up to 3 months after euthanasia if all the techniques described in this section are used.

An entire protocol of infection and pathogenesis analysis can be completed in 4-6 months by experienced personnel.

Acknowledgments

Several people have contributed to the development of these mouse models over the years either through hands-on implementation of techniques or through vigorous scientific discussions: Luciana Richer, Hari-Hara Potula, Mariana Soares Guedes, Elsio Wunder, David Haake (DH), and Catherine Werts. Funding was provided by NIH NIAID grants RO1 AI034431 (DH and MGS), R44 AI096551 (MGS), R21 AI142129 (MGS), R43 AI136551 (MGS).).

Author Contributions

Nisha Nair: Data curation; formal analysis; investigation; methodology; validation; visualization; writing-review & editing. **Maria Gomes-Solecki:** Conceptualization; data curation; formal analysis; funding acquisition; methodology; project administration; resources; supervision; visualization; writing-original draft; writing-review & editing.

Literature Cited

Adler, B., & Faine, S. (1976). Susceptibility of mice treated with cyclophosphamide to lethal infection with *Leptospira interrogans* Serovar pomona. *Infection and Immunity*, *14*(3), 703–708. doi: 10.1128/IAI.14.3.703-708.1976.

Adler, B., & Faine, S. (1977). Host immunological mechanisms in the resistance of mice to leptospiral infections. *Infection and Immunity*, *17*(1), 67–72. doi: 10.1128/IAI.17.1.67-72.1977.

Alturkistani, H. A. T., Tashkandi, F. M., & Mohammedsaleh, Z. M. (2016). Histological stains: A literature review and case study. *Global Journal of Health Science*, *8*(3) doi: 10.5539/gjhs.v8n3p72.

Asoh, T., Saito, M., Villanueva, S. Y., Kanemaru, T., Gloriani, N., & Yoshida, S. (2014). Natural defense by saliva and mucosa against oral infection by *Leptospira*. *Canadian Journal of Microbiology*, *60*(6), 383–389. doi: 10.1139/cjm-2014-0016.

Bharti, A. R., Nally, J. E., Ricaldi, J. N., Matthias, M. A., Diaz, M. M., Lovett, M. A., … Peru-United States Leptospirosis Consortium. (2003). Leptospirosis: A zoonotic disease of global importance. *The Lancet Infectious Diseases*, *3*(12), 757–771. doi: 10.1016/S1473-3099(03)00830-2.

Bonilla-Santiago, R., & Nally, J. E. (2011). Rat model of chronic leptospirosis. *Current Protocols in Microbiology*, *20*, 12E.3.1−12E.3.10. doi: 10.1002/9780471729259.mc12e03s20

Casanovas-Massana, A., Pedra, G. G., Wunder, E. A. Jr., Diggle, P. J., Begon, M., & Ko, A. I. (2018). Quantification of *Leptospira interrogans* survival in soil and water microcosms. *Applied and Environmental Microbiology*, *84*(13), e00507–e00518. doi: 10.1128/AEM.00507-18.

Chan, O., Madaio, M. P., & Shlomchik, M. J. (1997). The roles of B cells in MRL/lpr murine lupus. *Annals of the New York Academy of Sciences*, *815*, 75–87. doi: 10.1111/j.1749-6632.1997.tb52046.x.

Chassin, C., Picardeau, M., Goujon, J. M., Bourhy, P., Quellard, N., Darche, S., … Werts, C. (2009). TLR4- and TLR2-mediated B cell responses control the clearance of the bacterial pathogen, *Leptospira interrogans. Journal of Immunology*, *183*(4), 2669–2677. doi: 10.4049/jimmunol.0900506.

Copeland, S., Warren, H. S., Lowry, S. F., Calvano, S. E., Remick, D., & Inflammation and the Host Response to Injury Investigators (2005). Acute inflammatory response to endotoxin in mice and humans. *Clinical and Diagnostic Laboratory Immunology*, *12*(1), 60–67. doi: 10.1128/CDLI.12.1.60-67.2005.

Costa, F., Hagan, J. E., Calcagno, J., Kane, M., Torgerson, P., Martinez-Silveira, M. S., … Ko, A. I. (2015). Global morbidity and mortality of Leptospirosis: A systematic review. *PloS Neglected Tropical Diseases*, *9*(9), e0003898. doi: 10.1371/journal.pntd.0003898.

Donovan, J., & Brown, P. (2001). Anesthesia. *Current Protocols in Immunology*, *27*, 1.4.1–1.4.5. doi: 10.1002/0471142735.im0104s27

Donovan, J., & Brown, P. (2006a). Euthanasia. *Current Protocols in Immunology*, *73*, 1.8.1–1.8.4. doi: 10.1002/0471142735.im0108s73

Donovan, J., & Brown, P. (2006b). Parenteral injections. *Current Protocols in Immunology*, *73*, 1.6.1–1.6.10. doi: 10.1002/0471142735.im0106s73

Fanton d'Andon, M., Quellard, N., Fernandez, B., Ratet, G., Lacroix-Lamande, S., Vandewalle, A., … Werts, C. (2014). *Leptospira interrogans* induces fibrosis in the mouse kidney through Inos-dependent, TLR- and NLR-independent signaling pathways. *PloS Neglected Tropical Diseases*, *8*(1), e2664. doi: 10.1371/journal.pntd.0002664.

Ferrer, M. F., Scharrig, E., Alberdi, L., Cedola, M., Pretre, G., Drut, R., … Gomez, R. M. (2014). Decay-accelerating factor 1 deficiency exacerbates leptospiral-induced murine chronic nephritis and renal fibrosis. *PloS One*, *9*(7), e102860. doi: 10.1371/journal.pone.0102860.

Gomes, C. K., Guedes, M., Potula, H. H., Dellagostin, O. A., & Gomes-Solecki, M. (2018). Sex matters: Male hamsters are more susceptible to lethal infection with lower doses of pathogenic leptospira than female hamsters. *Infection and Immunity*, *86*(10), e00369–e003718. doi: 10.1128/IAI.00369-18.

Ko, A. I., Goarant, C., & Picardeau, M. (2009). *Leptospira*: The dawn of the molecular genetics era for an emerging zoonotic pathogen. *Nature Reviews Microbiology*, *7*(10), 736–747. doi: 10.1038/nrmicro2208.

Landreth, K. S. (2002). Critical windows in development of the rodent immune system. *Human & Experimental Toxicology*, *21*(9-10), 493–498. doi: 10.1191/0960327102ht287oa.

Mescher, A. (2018). *Junqueira's Basic Histology: Text and Atlas* (15th ed.). New York: McGraw-Hill Education.

Nahori, M. A., Fournie-Amazouz, E., Que-Gewirth, N. S., Balloy, V., Chignard, M., Raetz, C. R., … Werts, C. (2005). Differential TLR recognition of leptospiral lipid A and lipopolysaccharide in murine and human cells. *Journal of Immunology*, *175*(9), 6022–6031. doi: 10.4049/jimmunol.175.9.6022.

Nair, N., Guedes, M. S., Werts, C., & Gomes-Solecki, M. (2020). The route of infection with *Leptospira interrogans* serovar Copenhageni affects the kinetics of bacterial dissemination and kidney colonization. *PloS Neglected Tropical Diseases*, *14*(1), e0007950. doi: 10.1371/journal.pntd.0007950.

Nair, N., Soares Guedes, M., Hajjar, A., Werts, C., & Gomes-Solecki, M. (2020). Humanized TLR4 immunocompetent mice are more susceptible to kidney disease after infection with *Leptospira interrogans* than wild-type mice. *BioRxiv*, *2020.06.15.153106*. doi: https://doi.org/10.1101/2020.06.15.153106.

Nally, J. E., Fishbein, M. C., Blanco, D. R., & Lovett, M. A. (2005). Lethal infection of C3H/HeJ and C3H/SCID mice with an isolate of *Leptospira interrogans* serovar copenhageni. *Infection and Immunity*, *73*(10), 7014–7017. doi: 10.1128/IAI.73.10.7014-7017.2005.

Pereira, M. M., Andrade, J., Marchevsky, R. S., & Ribeiro dos Santos, R. (1998). Morphological characterization of lung and kidney lesions in C3H/HeJ mice infected with *Leptospira interrogans* serovar icterohaemorrhagiae: Defect of CD4+ and CD8+ T-cells are prognosticators of the disease progression. *Experimental and Toxicologic Pathology*, *50*(3), 191–198. doi: 10.1016/S0940-2993(98)80083-3.

Potula, H. H., Richer, L., Werts, C., & Gomes-Solecki, M. (2017). Pre-treatment with *Lactobacillus plantarum* prevents severe pathogenesis in mice infected with *Leptospira interrogans* and may be associated with recruitment of myeloid cells. *PloS Neglected Tropical Diseases*, *11*(8), e0005870. doi: 10.1371/journal.pntd.0005870.

Ratet, G., Veyrier, F. J., Fanton d'Andon, M., Kammerscheit, X., Nicola, M. A., Picardeau, M., … Werts, C. (2014). Live imaging of bioluminescent *Leptospira interrogans* in mice reveals renal colonization as a stealth escape from the blood defenses and antibiotics. *PloS Neglected Tropical Diseases*, *8*(12), e3359. doi: 10.1371/journal.pntd.0003359.

Richer, L., Potula, H. H., Melo, R., Vieira, A., & Gomes-Solecki, M. (2015). Mouse model for sublethal *Leptospira interrogans* infection. *Infection and Immunity*, *83*(12), 4693–4700. doi: 10.1128/IAI.01115-15.

Santos, C. S., Macedo, J. O., Bandeira, M., Chagas-Junior, A. D., McBride, A. J., McBride, F. W., … Athanazio, D. A. (2010). Different outcomes of experimental leptospiral infection in mouse strains

with distinct genotypes. *Journal of Medical Microbiology*, *59*(Pt 9), 1101–1106. doi: 10.1099/jmm.0.021089-0.

Schneider, A. G., Casanovas-Massana, A., Hacker, K. P., Wunder, E. A., Jr., Begon, M., Reis, M. G., … Ko, A. I. (2018). Quantification of pathogenic *Leptospira* in the soils of a Brazilian urban slum. *PloS Neglected Tropical Diseases*, *12*(4), e0006415. doi: 10.1371/journal.pntd.0006415.

Sullivan, J. P., Nair, N., Potula, H. H., & Gomes-Solecki, M. (2017). Eye-drop inoculation leads to sublethal leptospirosis in mice. *Infection and Immunity*, *85*(4), e01050-10616. doi: 10.1128/IAI.01050-16.

Thiermann, A. B. (1981). The Norway rat as a selective chronic carrier of *Leptospira icterohaemorrhagiae*. *Journal of Wildlife Diseases*, *17*(1), 39–43. doi: 10.7589/0090-3558-17.1.39.

Viriyakosol, S., Matthias, M. A., Swancutt, M. A., Kirkland, T. N., & Vinetz, J. M. (2006). Toll-like receptor 4 protects against lethal *Leptospira interrogans* serovar icterohaemorrhagiae infection and contributes to in vivo control of leptospiral burden. *Infection and Immunity*, *74*(2), 887–895. doi: 10.1128/IAI.74.2.887-895.2006.

Vogel, S. N., Johnson, D., Perera, P. Y., Medvedev, A., Lariviere, L., Qureshi, S. T., & Malo, D. (1999). Cutting edge: Functional characterization of the effect of the C3H/HeJ defect in mice that lack an *Lpsn* gene: In vivo evidence for a dominant negative mutation. *Journal of Immunology*, *162*(10), 5666–5670.

Werts, C., Tapping, R. I., Mathison, J. C., Chuang, T. H., Kravchenko, V., Saint Girons, I., … Ulevitch, R. J. (2001). Leptospiral lipopolysaccharide activates cells through a TLR2-dependent mechanism. *Nature Immunology*, *2*(4), 346–352. doi: 10.1038/86354.

Physiological Reports

Open Access

Physiological Reports ISSN 2051-817X

ORIGINAL RESEARCH

CD4+ T cell activation and associated susceptibility to HIV-1 infection in vitro increased following acute resistance exercise in human subjects

Alexander K. Holbrook[1], Hunter D. Peterson[2], Samantha A. Bianchi[2], Brad W. Macdonald[2], Eric C. Bredahl[2], Michael Belshan[1] & Jacob A. Siedlik[2]

1 Department of Medical Microbiology and Immunology, Creighton University, Omaha, Nebraska
2 Department of Exercise Science and Pre-Health Professions, Creighton University, Omaha, Nebraska

Keywords
Physical activity, T cell activation, viral infection.

Correspondence
Jacob A. Siedlik, Department of Exercise Science and Pre-Health Professions, Creighton University, 2500 California Plaza, Omaha, NE 68178.
Tel: +1 402 280 2474
Fax: +1 402 280 4732
E-mail: jakesiedlik@creighton.edu

Funding information
This work was supported by the Dr. George F. Haddix President's Faculty Research Fund at Creighton University.

Received: 24 June 2019; Revised: 22 August 2019; Accepted: 27 August 2019

doi: 10.14814/phy2.14234

Physiol Rep, 7 (18), 2019, e14234, https://doi.org/10.14814/phy2.14234

Abstract

Early studies in exercise immunology suggested acute bouts of exercise had an immunosuppressive effect in human subjects. However, recent data, show acute bouts of combined aerobic and resistance training increase both lymphocyte activation and proliferation. We quantified resistance exercise-induced changes in the activation state of $CD4^+$ T lymphocytes via surface protein expression and using a medically relevant model of infection (HIV-1). Using a randomized cross-over design, 10 untrained subjects completed a control and exercise session. The control session consisted of 30-min seated rest while the exercise session entailed 3 sets × 10 repetitions of back squat, leg press, and leg extensions at 70% 1-RM with 2-min rest between each set. Venous blood samples were obtained pre/post each session. $CD4^+$ T lymphocytes were isolated from whole blood by negative selection. Expression of activation markers (CD69 & CD25) in both nonstimulated and stimulated (costimulation through $CD3^+CD28$) cells were assessed by flow cytometry. Resistance exercised-induced effects on intracellular activation was further evaluated via in vitro infection with HIV-1. Nonstimulated $CD4^+$ T lymphocytes obtained postexercise exhibited elevated CD25 expression following 24 h in culture. Enhanced HIV-1 replication was observed in cells obtained postexercise. Our results demonstrate that an acute bout of resistance exercise increases the activation state of $CD4^+$ T lymphocytes and results in a greater susceptibility to HIV-1 infection in vitro. These findings offer further evidence that exercise induces activation of T lymphocytes and provides a foundation for the use of medically relevant pathogens as indirect measures of intracellular activation.

Introduction

The human immune system is divided into two categories, innate and adaptive, that can elicit both broad or highly targeted responses. $CD4^+$ T cells are essential mediators of both the innate and adaptive immune responses. They play an integral role in the overall immunocompetence of an individual through the release of cytokines and chemokines, the recruitment of immune cells to sites of infection and inflammation, the activation of macrophages, and the activation of B cells to produce antigen-specific antibodies. In the adaptive arm, the activation of $CD4^+$ T cells following exposure to cognate antigen (Medzhitov 2007) is associated with changes in expression of specific proteins, including increased expression of CD69 and CD25, which are used as early (Testi et al. 1989) and intermediate (Malek 2008) markers of cellular activation, respectively.

It has been demonstrated that both aerobic and resistance exercise have the potential to alter the immune state of an individual. Evidence from a 2016 meta-analytic review suggests the proliferative response of mixed lymphocyte populations (i.e., peripheral blood mononucleocytes (PBMCs)) to in vitro mitogenic stimuli is

suppressed following an acute bout of exercise (Siedlik et al. 2016). Notably, most of the research investigating the effect of exercise on immunity have focused on PBMC proliferation in response to an acute bout of aerobic exercise (Walsh et al. 2011; b). In comparison, limited research has been conducted examining the relationship between acute bouts of resistance training and immunity often with conflicting results (Dohi et al. 2001; Koch et al. 2001; Potteiger et al. 2001; Chan et al. 2003). Nieman et al. (Nieman et al. 1995) observed no significant differences in concanavalin A (ConA) stimulated lymphocyte proliferation in trained men following repeated sets of 10 repetition back squats at 65% of 1 repetition maximum (1RM). Potteiger et al. (2001), however, observed reduced phytohemagglutinin (PHA) stimulated lymphocyte proliferation in untrained females following an acute bout of lower limb resistance training, but no change in proliferation for trained female participants. As seen above, the training status of the participants, as well as the mitogens used for stimulation, may affect in vitro proliferative responses. Moreover, the question of how different immune subsets respond to acute resistance exercise remains unanswered, preventing a full understanding of the clinical consequence of exercise prescription.

Cellular activation in response to an antigen leads to clonal expansion of antigen-specific T cells to facilitate neutralization of an invading pathogen (Mueller et al. 1989). In laboratory and clinical settings, clonal expansion in response to either mitogenic stimulation or co-stimulation through CD28 is commonly utilized as a measure of lymphocyte functional ability (Siedlik et al. 2016; 2017). Indeed, studies investigating the effects of exercise on the immune system have commonly used proliferation assays to quantify changes in lymphocyte function following an acute bout of aerobic exercise. As addressed briefly above, however, proliferative assays can produce ambiguous results due to methodological variability (Siedlik et al. 2016) and a failure to quantify specific elements of the activation process. Measurement of specific immune cell functions potentially can improve the understanding of the impact of excise on immunity.

Exercise-induced alterations in immune function have the potential to affect the interaction of pathogens with the immune system. A change in cellular activation state and/or subsequent alteration in proliferation of immune cell subsets could alter the disease state in an individual. For example, changes in $CD4^+$ T lymphocyte activation could enhance an immune response and provide greater protection against an invading pathogen. Conversely, heightened cell activation may create favorable conditions for lymphotropic pathogens, such as human immunodeficiency virus (HIV). Type 1 HIV (HIV-1), the etiologic agent of acquired immune deficiency syndrome (AIDS), is a member of the retrovirus family that preferentially infects activated $CD4^+$ T lymphocytes. More than 36 million persons are infected with HIV-1 worldwide (UNAIDS). HIV-1 replication correlates strongly with the activation state of T cells due to the metabolic requirements of reverse transcription and integration into the host genome (Gowda et al. 1989; Stevenson et al. 1990). Hence, any transient alteration in the metabolic state of a $CD4^+$ T cell will change its susceptibility to HIV-1. Here, we propose to use HIV-1 infection as a biological model to independently asses $CD4^+$ T cell activation state. Notably, quiescent $CD4^+$ T cells, which are metabolically and transcriptionally silent (Yusuf and Fruman 2003; Tzachanis et al. 2004), were originally thought to be refractory to HIV infection; however, evidence suggests that partially activated cells can support infection, especially with subsequent stimulation (Stevenson et al. 1990; Zack et al. 1990, 1992; Korin and Zack, 1998; Unutmaz et al. 1999; Manganaro et al. 2018).

Previous work from our laboratory demonstrated an increase in CD25 expression and enhanced proliferative responses in $CD4^+$ T cells following combined aerobic and resistance training exercise (i.e., circuit training) (Siedlik et al. 2017). In this study, we focused our efforts to investigate whether resistance training alone altered $CD4^+$ T cell activation state and response to co-stimulation with CD28. In parallel we tested susceptibility to HIV-1 infection to independently validate any changes in activation state resulting from exercise. To do this, we compared $CD4^+$ T cells isolated from individuals prior to and after acute resistance training. Notably, the data were cross-compared to a nonexercise session as an additional control. Changes in early markers of activation, specifically expression of CD25 and CD69, were analyzed from two distinct perspectives. First, was there an exercise-induced effect on $CD4^+$ T cell activation absent stimuli in culture (Arm 1), and second, was there an exercise-induced effect on the ability of $CD4^+$ T cells to respond to stimuli in culture (Arm 2). Together, this study represents a first attempt to quantify exercise-induced changes in $CD4^+$ T cell function using a medically relevant viral model.

Methods

Participants

Ten healthy, untrained, college-aged individuals (Mean ± SD, $n = 10$ [5 male & 5 female], age = 21 ± 2 year; weight = 71.5 ± 10.1 kg; height = 171.8 ± 7.1 cm) volunteered to participate. Untrained status was defined as no more than 1 h of aerobic and/or resistance

training per week. All participants provided written informed consent and completed a Health & Exercise Status Questionnaire prior to participation. At the time of recruitment, subjects were instructed to maintain their normal dietary patterns prior to participating in either session, but to refrain from exercise for 24 h prior to data collection. Participants reported that they had neither recently taken nor were currently using non-steroidal anti-inflammatory drugs (NSAID), aspirin, or other anti-thrombotic over-the-counter or prescription medications. All participants reported being negative for HIV infection. Participants reported no cold or flu symptoms in the 2 weeks prior to data collection. The study conformed to the standards set by the Declaration of Helsinki and the procedures followed were in accordance with the protocol approved by the Creighton University Institutional Review Board (959210-1).

3-repetition maximum assessments

Each participant completed an initial strength assessment that included 3-repetition maximum [RM] barbell high bar parallel squat, 3-RM leg press, and 3-RM leg extension. The 3-RM back squat was tested on their first visit and the leg press and leg extension were assessed at a visit at least 2 days after squat testing. All participants completed a 5 min self-paced warm-up on a cycle ergometer prior to starting any warm-up sets. The 3-RM testing followed the protocol recommended by the National Strength and Conditioning Association (Haff and Triplett 2016). For all exercises, the first warm-up set required 5–10 repetitions. The second warm-up set and beyond required 2–5 repetitions until a 3-RM was attempted. Participants were allowed multiple attempts at the 3-RM to attain the highest load possible. The 3RM was recorded and used for estimation of 1RM values using the following equation: (3RM/ 0.9 = 1RM). All experiment visits took place at least 1 week after completion of repetition maximum testing.

Testing protocol

Following the fitness assessments, each participant randomly completed a control and exercise session, which occurred between 0700 and 0745 h. Both visits occurred within a 7-day time frame. The exercise session included a 5-min self-paced warm-up on a cycle ergometer followed by 3 sets of 10 repetitions of back squats at 70% of estimated 1-RM, 3 sets of 10 repetitions of leg press at 70% 1-RM, and 3 sets of 10 repetitions of leg extension at 70% 1-RM with 2-min rest between sets. The control session involved the subjects sitting quietly in a room for 30 min. Subjects were not allowed to read or use electronic devices during this time and were monitored at random intervals to ensure they remained alert.

Physiological monitoring

Participants were fitted with a Zephyr BioHarness 3 (Zephyr Technology, Annapolis, MD) to measure heart rate (HR). Continuous HR measures were recorded at 1 sec intervals during the training session and downloaded using the Zephyr BioHarness Log Downloader (version 1.0.29.0). HR_{max} was estimated using the methods of Tanaka et al. (2001).

Blood collections

Blood samples were collected in sodium heparin vacutainers prior to (Pre) and immediately following (Post) each testing session using standard antecubital venipuncture technique.

Antibodies and reagents

Antibodies used for flow cytometry were purchased from BioLegend (San Diego, CA) and include: anti-CD4-Alexa Fluor 700 (RPA-T4), CD69-APC/Cy7 (FN50), and CD25-PE (M-A251).

Cell purification and culture

Blood samples (80 mL) were obtained at each time point for analyses of surface marker expression and viral replication. $CD3^+CD4^+$ T cell isolation from peripheral blood was conducted through negative selection using a Human $CD4^+$ T cell enrichment kit as directed by the manufacturer (Stemcell Technologies, Vancouver, BC, Canada). Purity was assessed following cell isolation by staining with anti-CD4-Alexa Fluor 700 (RPA-T4) and all samples were >97% $CD4^+$ by flow cytometry (Kohlmeier et al. 2006; Newton and Benedict, 2014; Siedlik et al. 2017). After purification, the cells were resuspended in warm Immunocult-XF T cell expansion medium (Stemcell Technologies, Vancouver, BC, Canada).

Surface marker expression – cell stimulation and culture

Cells were co-stimulated through $CD3^+CD28$ using plate-bound antibodies or no simulation as previously described (Chirathaworn et al. 2002; Kohlmeier et al. 2006; Siedlik et al. 2017). Each antibody was titrated to the lowest concentration that gave maximum T cell activation: anti-CD3 (OKT3) used at 1 μg/mL (BioLegend, San Diego, CA) and anti-CD28 (CD28.2) at 2 μg/mL

(BioLegend, San Diego, CA). Antibodies were diluted in sterile Dulbecco's Phosphate Buffered Saline (dPBS) (Life Technologies, Grand Island, NY) added to 96-well plates and incubated overnight at 4°C. Unbound antibodies were removed by washing 3x with dPBS prior to cell plating. $CD4^+$ T cells were plated at 1.5×10^6 cells/mL in 200 μL of Immunocult-XF T-cell media (Stemcell Technologies, Vancouver, BC, Canada) directly after isolation. Cells were cultured at 37°C in a humidified incubator with 5% CO_2. Cells were analyzed by flow cytometry using anti-CD4-Alexa Fluor 700, anti-CD69-APC/Cy7, and anti-CD25-PE antibodies immediately after $CD4^+$ T cell isolation (0 h), 24 h, and 72 h in culture using a ZE5 Cell Analyzer (Propel Labs, Fort Collins, CO). Data analysis was performed with FlowJo software v10 (TreeStar, Ashland, OR). Compensation was performed using single antibody positive and negative controls (OneComp eBeads Compensation Beads, ThermoFisher Scientific, Waltham, MA) in each assay. Gates were set based on fluorescence minus one controls. A representative gating strategy is shown in Figure 1.

HIV-1 viral replication assays - cell stimulation and culture

HIV-1 NLX virus stocks were produced through the transfection of 293T cells with 5 μg of pNLX molecular clone and quantified by p24 antigen ELISA as previously described (Siedlik et al. 2016). Both unstimulated and CD3/CD28 stimulated cells were infected for each condition. Unstimulated $CD4^+$ T cells were infected and cultured shortly after purification. 1×10^6 cells were seeded in three wells as per condition in a 24-well plate and incubated with HIV-1 at a multiplicity of infection (MOI) of 0.1 for 4 h at 37°C with 5% CO_2. Cells were then pelleted, washed with dPBS, and resuspended in 550 μL fresh culture media (RPMI-1640 Medium [GE Healthcare, Piscataway, NJ] + 10% Fetal bovine serum [Corning, Corning, New York] + 2% Penicillin/Streptomycin [Corning, Corning, New York] + 20 mmol/L L-glutamine [Corning, Corning, New York] + 50 units/mL recombinant Human IL-2 [R&D Systems, Minneapolis, MN]) per well, in a new 24-well plate. Cells were stimulated using plate-bound antibodies as outlined above, but in 24-well plates at 2×10^6 cells/mL in 500 μL of Immunocult-XF T-cell media (Stemcell Technologies, Vancouver, BC, Canada) culture. Stimulated $CD4^+$ T cell HIV-1 infections occurred after 3 days of CD3/CD28 stimulation. Both unstimulated and CD3/CD28 stimulated cells were cultured for 17 days. Supernatant samples were collected at 0, 3, 7, 10, 14, and 17 days post infection (dpi), clarified by centrifugation, and stored at −20°C. For the reactivation studies, unstimulated cells were activated at 14 dpi with human CD3/CD28/CD2 T cell activator beads for 3 days (Stemcell Technologies, Vancouver, BC, Canada) and additional RT sample collected at 17 dpi. An overview of the cell culture experiments is shown in Figure 2.

Reverse transcriptase assay

Virus replication/production was quantified by a reverse transcriptase (RT) assay as described previously (DeBoer et al. 2018). Triplicate 10 µL of supernatant were assayed per timepoint. Fresh culture media was used as a negative control, and an NLX virus standard as a positive control in each reaction plate. An RT assay mix of H_20, 50 mmol/L Tris (pH 7.9), 75 mmol/L KCL, 2 nmol/L DTT, 0.1875 mmol/L ATP, 5 mmol/L $MgCl_2$, RT Primer (25 mg/L), 0.05% NP-40, 2 μmol/L dTTP, and 2 μCi

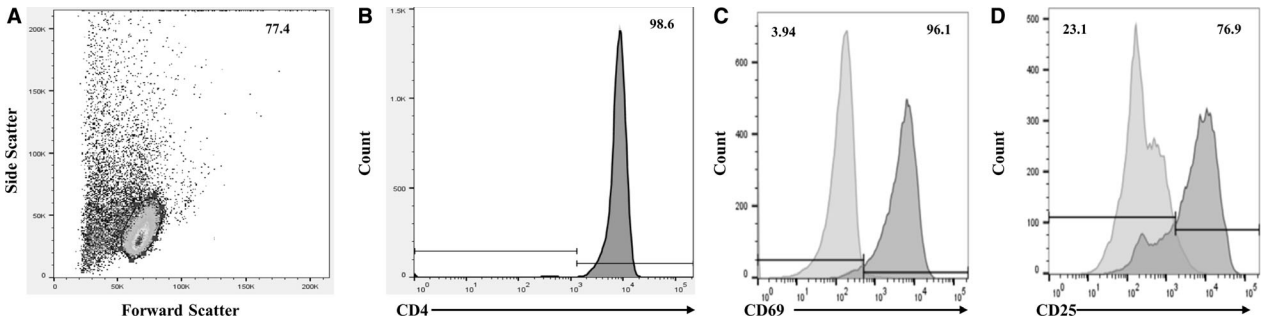

Figure 1. Representative gating procedures for analyzed samples. (A) Illustrates usage and placement of the live cell gate in the forward scatter versus side scatter plot. Sample populations were all >97% $CD3^+CD4^+$ following isolation. All flow data were gated as in (A) before further analysis. An unstained sample (not shown) was used as a guide for placement of the $CD4^+$ gate in the fully stained sample (B). Expression of surface markers of activation in non-stimulated and stimulated cell populations were quantified using median fluorescent intensity (MFI) of (C) CD69 and (D) CD25. Overlays of the non-stimulated (light gray) and stimulated samples (dark gray) were used to correct for the effect of costimulation through CD28 prior to analyzing exercise-induced alterations.

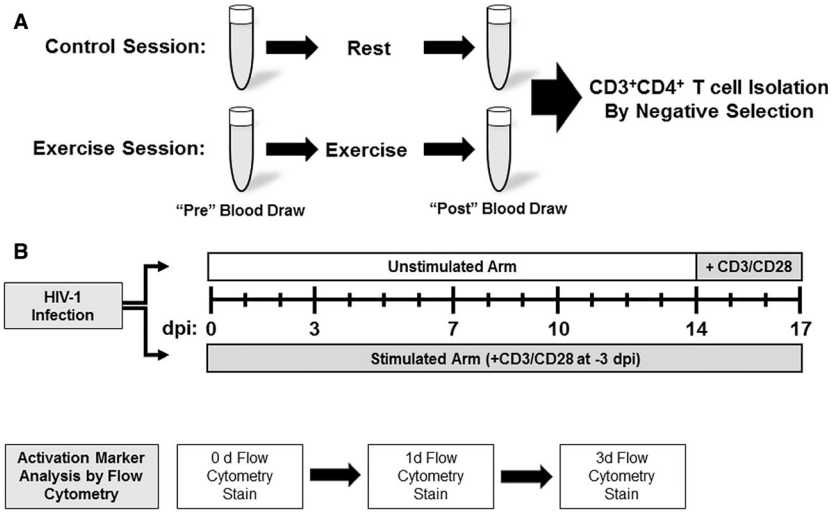

Figure 2. Overview of experiment design. Each subject participated in both a control and exercise session with order randomized. Blood was collected pre and post each visit (A) and $CD3^+CD4^+$ T cells isolated via negative selection. (B) Both unstimulated and CD3/CD28 stimulated cells were cultured for 17 days. Stimulated $CD4^+$ T cell HIV-1 infections occurred after 3 days of CD3/CD28 stimulation. Supernatant samples were collected at 0, 3, 7, 10, 14, and 17 days post infection (dpi). Surface protein expression was quantified via flow cytometry at 0, 1, and 3 days.

[^{32}P]-α-TTP was prepared and vortexed thoroughly (Siedlik et al. 2016). 30 μL of RT assay mix was added to each well and the plate was incubated at 37°C for 3 h. RT mix was added to Whatman paper in individual spots and allowed to dry. The paper was washed three times with 2× saline-sodium citrate (SSC) for 5 min while rocking, washed once with 95% Ethanol, and allowed to dry. The dried paper was then exposed to a phosphor screening plate. After overnight exposure, the phosphor plates are analyzed on GE Amersham Molecular Dynamics Typhoon 9410 Molecular Imager v5.0 (GE Healthcare, Piscataway, NJ). The image was quantified using Molecular Dynamics ImageQuant v5.2 software (GE Healthcare, Piscataway, NJ), setting the background to a negative control sample.

Statistical analysis

Power calculations were based on previously reported data that investigated exercise-induced changes in T cell activation and proliferation (Siedlik et al. 2017). The power analysis indicated 10 subjects would exceed 80% power for detecting an effect size of $d_z = 0.99$ [a large effect as outlined by Cohen (1992)] for relevant differences at an alpha < 0.05. For this investigation, quantification of the change in values from pre-to-post was of more interest than the absolute values of the measurements themselves; therefore, fold change scores were calculated using log2 transformations: log2(Post/Pre). Normality of data was verified using the D'Agostino-Pearson test. Data were analyzed using paired samples *t*-tests in R version 3.3.1 (Team 2014). Given the exploratory nature of this project, Bayesian paired samples *t*-tests were also performed using the BEST package in R (Kruschke 2013). Reported parameter estimates from Bayesian models include the posterior mean difference, 95% highest density intervals (HDI), probability the true mean difference is greater than 0, and, when relevant, threshold estimates to determine the probability the true difference of the means is greater than a 10% increase.

Results

Resistance training session induced substantial changes in heart rate

The exercise session elicited a substantial sympathetic stimulus as demonstrated by the HR data. The mean predicted HR_{max} for all subjects was 193 ± 2 bpm. Average HR during the exercise trial was 137 ± 14 bpm compared with 82 ± 10 bpm in the control subjects ($P < 0.001$). The average peak HR during the trials was 174 ± 14 bpm and 109 ± 11 bpm for exercise and control, respectively ($P < 0.001$). During the exercise session, subjects spent approximately half of the time (13.4 ± 7.3 min) working at over 70% of their predicted HR_{max}, whereas all subjects spent the entirety of the control session under the 60% threshold of predicted HR_{max}. Summary of statistical results and comparative analyses are presented in Table 1.

Table 1. Summary output for all statistical analyses performed.

		Null hypothesis significance test					Bayesian analyses			
	Time	$Mean_{diff}$	*t*	df	*P*	95% CI	Post. $Mean_{diff}$	SD_{diff}	95% HDI	*P* ($Mean_{diff}$ > 0)
No-Stim										
CD25	0 h	−0.2	−0.73	9	0.49	−0.8, 0.41	−0.2	0.89	−0.84, 0.47	0.25
	24 h	0.27	2.4	9	0.04	0.02, 0.52*	0.28	0.37	0.01, 0.53	0.98
	72 h	0.04	0.12	9	0.91	−0.7, 0.78	0.06	1.1	−0.74, 0.83	0.57
CD69	0 h	−0.29	−0.74	9	0.48	−1.7, 0.6	−0.23	1.3	1.2, 0.71	0.29
	24 h	0.02	0.09	9	0.93	−0.37, 0.41	0.02	0.58	−0.41, 0.43	0.55
	72 h	0.1	0.36	9	0.73	−0.53, 0.74	0.11	0.93	−0.56, 0.77	0.65
CD4	0 h	−0.04	−1.41	9	0.19	−0.1, 0.02	−0.04	0.1	−0.11, 0.03	0.13
	24 h	0.02	0.32	9	0.76	−0.11, 0.15	0.02	0.19	−0.12, 0.16	0.62
	72 h	0.05	1.09	9	0.3	−0.05, 0.14	0.05	0.15	−0.06, 0.15	0.82
Stim										
CD25	24 h	−0.58	−0.75	9	0.47	−2.35, 1.18	−0.51	2.5	−2.4, 1.3	0.27
	72 h	0.95	2.08	9	0.07	−0.08, 1.98	0.96	1.5	−0.16, 2.1	0.96
CD69	24 h	−0.36	−0.8	9	0.45	−1.37, 0.65	−0.04	0.76	−0.94, 0.57	0.43
	72 h	0.22	0.76	9	0.47	−0.43, 0.86	0.23	0.96	−0.48, 0.9	0.76
CD4	24 h	−0.06	−0.12	9	0.91	−1.24, 1.12	−0.29	1.3	−1.2, 0.75	0.26
	72 h	0.15	0.2	9	0.84	−1.49, 1.78	0.12	2.4	−1.6, 2	0.56
HIV-1										
Viral replication	0 day	0.35	1.34	9	0.21	−0.25, 0.97	0.21	0.6	−0.23, 0.78	0.87
	3 day	0.28	2.68	9	0.03	0.04, 0.51*	0.27	0.35	0.02, 0.53	0.98
	7 day	0.3	0.79	9	0.44	−0.56, 1.15	0.31	1.3	−0.65, 1.2	0.76
Heart rate										
Average		56	13.14	9	<0.001	46, 65*	56	14	46, 66	>0.999
Peak		66	12.42	9	<0.001	54, 78*	65	17	52, 77	>0.999

Mean differences were calculated as Experiment – Control.

Exercise induced changes in expression of CD25 but not CD69

Surface expression of CD4, CD25, and CD69 was quantified via median fluorescent intensity [MFI] immediately after $CD4^+$ T cell isolation (0 h) and after 24 and 72 h in culture. Notably, CD4 expression was not significantly different in cells isolated pre or post the control and exercise session (data not shown). When examining exercise-induced changes in nonstimulated $CD4^+$ T cells (Arm 1), there was no significant difference in CD25 expression on cells isolated before either the control or exercise session (Pre). There was, however, a significant increase in CD25 expression on cells isolated postexercise relative to the control session after 24 h in culture ($P = 0.04$, Fig. 3a). The estimated mean difference using the Bayesian model is 0.28, equivalent to a fold change increase > 21% in the cells collected pre-to-post the exercise session compared to the control. Moreover, 95% HDI does not include zero, and the probability the true value is greater than zero is 98% (Table 1). A threshold estimation indicates there is an 86.5% probability that the true difference in means is greater than 10%. The analysis implies that exercise-induced changes in CD25 expression, in addition to being statistically significant, are likely physiologically relevant. However, after 72 h in culture the effect dissipated ($P = 0.91$, Fig. 3b) indicating that the increased expression of CD25 was transient. No significant differences in the expression of CD69 were observed between the exercise and control sessions at any time points (Fig. 3C–D). Summary data for the intensity of surface protein expression on nonstimulated cells (Arm 1) are shown in Table 2.

In Arm 2, we investigated the $CD4^+$ T cell response to co-stimulation through CD28 (Fig. 4A–B). The results showed increased expression of CD25, similar to Arm 1, but no statistically significant ($P < 0.05$) differences were observed. Interestingly, the average fold change in CD25 expression after 72 h in culture was elevated in the exercise session compared to the resting control session, but not to a statistically significant level ($P = 0.07$, Fig. 4B). Follow-up Bayesian analyses to increase the predictive precision estimated the mean difference for CD25 expression at 72 h as 0.96 (equivalent to an increase > 93% in the exercise session relative to the control). The 95% HDI of the difference of means includes zero, but has 96% of

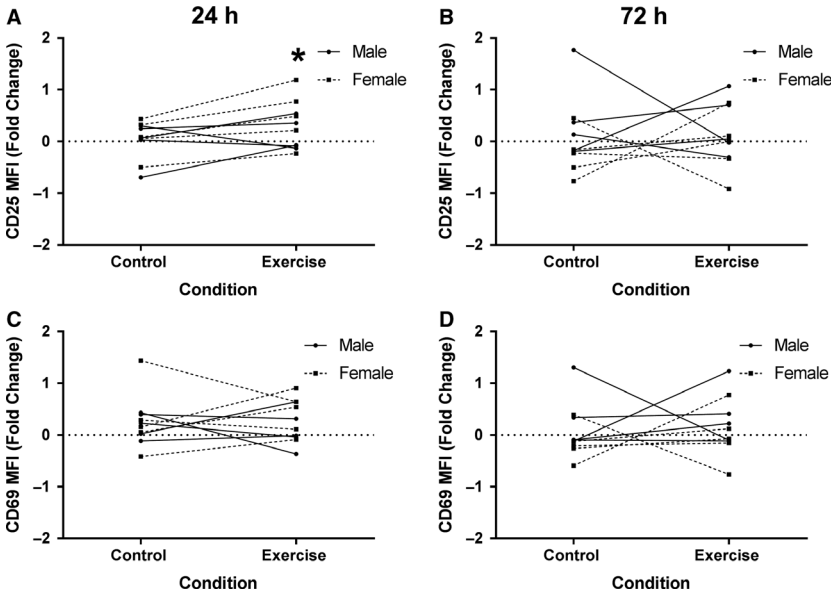

Figure 3. Expression of surface markers of activation increased on non-stimulated CD4$^+$ T cell populations. Human CD4$^+$ T cells were isolated and cultured in non-stimulated wells for 1 and 3 days then stained for CD25 and CD69 and analyzed by flow cytometry. The median fluorescence intensity (MFI) was determined for expression of CD25 at (A) 1 day (Control: 0.03 ± 0.36, Exercise: 0.3 ± 0.46) and at (B) 3 days (Control: 0.07 ± 0.7, Exercise: 0.11 ± 0.59). CD69 expression at (C) 1 days (Control: 0.25 ± 0.49, Exercise: 0.27 ± 0.54) and at (D) 3 days (Control: 0.06 ± 0.52, Exercise: 0.16 ± 0.55). Data are presented as fold change from baseline and visualized as spaghetti plots with each line representing the change between paired samples; n = 10. * Indicates a statistically significant difference ($P < 0.05$) from the control session.

Table 2. Summary data for surface protein expression on nonstimulated CD4$^+$ T lymphocytes.

		0 h	24 h	72 h
Control				
CD4	Pre	9578.9 ± 544.7	8966.1 ± 1216.5	9151.3 ± 1184.3
	Post	9868.3 ± 541.7	8975.9 ± 1022.2	9454.5 ± 1270.9
CD69	Pre	203.3 ± 143.2	171.4 ± 84.7	150.8 ± 40.1
	Post	207.0 ± 100.2	198.4 ± 71.4	159.2 ± 52.6
CD25	Pre	342.8 ± 156.9	291.8 ± 102.1	195.3 ± 55.8
	Post	374.3 ± 150.8	291.3 ± 71.6	212.5 ± 83.7
Exercise				
CD4	Pre	9456.9 ± 757.3	9196.3 ± 2251.4	8998.7 ± 1159.1
	Post	9476.2 ± 737.0	9269.2 ± 1850.5	9653.7 ± 1691.0
CD69	Pre	169.7 ± 66.1	172.1 ± 99.2	160.4 ± 56.5
	Post	180.5 ± 99.5	194.2 ± 69.7	173.3 ± 52.6
CD25	Pre	340.9 ± 117.0	325.4 ± 233.3	230.2 ± 90.6
	Post	332.7 ± 123.1	370.1 ± 206.1	231.2 ± 41.0

Values represent median fluorescent intensity (MFI) assessed via flow cytometry. Data are presented as Mean ± SD.

the credible values greater than zero. Thus, there is a strong probability that the estimated parameter is greater than zero (i.e., indicative of an exercise-induced increase in expression). The probability that the true mean difference would be greater than a 10% increase in CD25 expression was calculated at 93.3%. This suggests there is a 93.3% chance that exercise alters CD4$^+$ T cell response to stimuli. Similar to the nonstimulated Arm, there were no significant differences in CD69 expression observed at either 24 h or 72 h (Fig. 4C–D). Data for the intensity of surface protein expression on stimulated cells is summarized in Table 3. Summary data for the percent of activated cells in both stimulated and nonstimulated cultures are shown in Table 4.

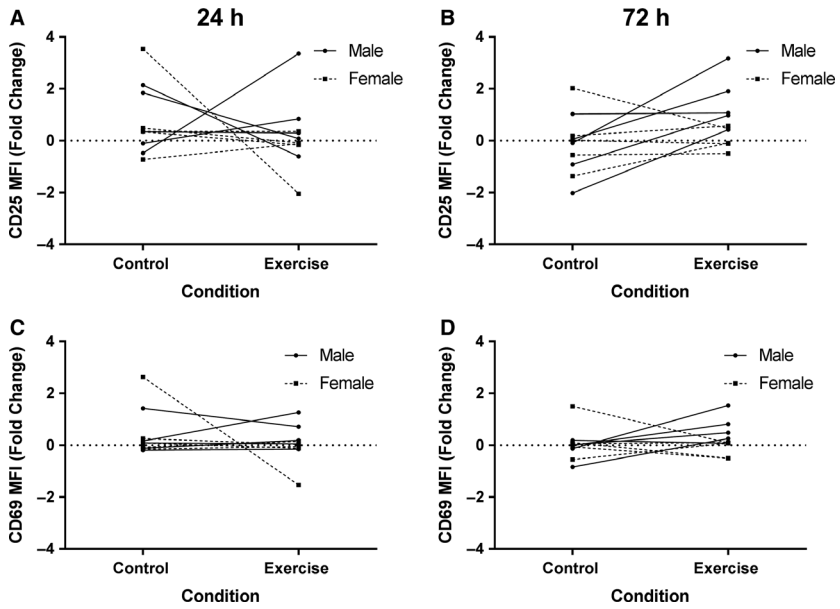

Figure 4. Expression of surface markers of activation in stimulated CD4⁺ T cell populations. Human CD4⁺ T cells were stimulated for 1 and 3 days with anti-CD3 and anti-CD28 then stained for CD25 and CD69 and analyzed by flow cytometry. The median fluorescence intensity (MFI) was determined for expression of CD25 at (A) 1 days (Control: 0.77 ± 1.3, Exercise: 0.19 ± 1.3) and at (B) 3 days (Control: −0.16 ± 1.2, Exercise: 0.79 ± 1.1). CD69 expression at (C) 1 days (Control: 0.41 ± 0.91, Exercise: 0.06 ± 0.71) and at (D) 3 days (Control: 0.03 ± 0.61, Exercise: 0.25 ± 0.6). Data are presented as fold change from baseline and visualized as spaghetti plots with each line representing the change between paired samples; n = 10.

Table 3. Summary data for surface protein expression on CD4⁺ T cells costimulated through CD28.

		24 h	72 h
Control			
CD4	Pre	6092.3 ± 2049.0	15675.9 ± 3537.3
	Post	6302.2 ± 2090.4	17547.6 ± 3360.9
CD69	Pre	4072.4 ± 2930.5	1031.2 ± 269.9
	Post	4436.9 ± 2305.4	1084.5 ± 339.1
CD25	Pre	2850.3 ± 2356.4	5496.5 ± 4290.7
	Post	3364.4 ± 1889.7	4718.2 ± 3469.1
Exercise			
CD4	Pre	6417.7 ± 2726.9	16004.6 ± 5179.2
	Post	6320.8 ± 2505.9	16762.9 ± 5133.9
CD69	Pre	4422.8 ± 2475.5	1748.0 ± 1746.5
	Post	4020.4 ± 2026.4	1721.3 ± 1270.1
CD25	Pre	3539.9 ± 2154.8	5391.2 ± 4791.3
	Post	3819.4 ± 2739.6	7203.3 ± 5967.8

Values represent median fluorescent intensity (MFI) assessed via flow cytometry. Data are presented as Mean ± SD.

Table 4. Summary data for percent of CD4⁺ T lymphocytes expressing both CD25 and CD69.

		0 h	24 h	72 h
No-stimulation				
Control	Pre	0.4 ± 0.2	0.6 ± 0.5	0.7 ± 0.3
	Post	0.7 ± 0.7	0.6 ± 0.4	0.7 ± 0.3
Exercise	Pre	0.4 ± 0.2	0.5 ± 0.2	0.8 ± 0.5
	Post	0.6 ± 0.5	0.4 ± 0.2	0.7 ± 0.4
Stimulation through CD3⁺CD28				
Control	Pre		57.9 ± 19.4	69.4 ± 18.3
	Post		64.0 ± 12.7	72.7 ± 14.5
Exercise	Pre		60.5 ± 19.9	68.8 ± 20.0
	Post		61.3 ± 17.9	73.6 ± 15.9

Values represent percent of cells expressing both surface proteins. Data are presented as Mean ± SD.

HIV-1 infection is increased in stimulated cells obtained postexercise

As an alternative means to measure the level of activation in CD4⁺ T cells, infection with the CXCR4-tropic HIV-1 NLX virus was chosen as a biological model system. HIV-1 preferentially infects activated CD4⁺ cells due to the presence of increased metabolic activity. We hypothesized that increased activation in CD4⁺ cells harvested postexercise would lead to an increased susceptibility to HIV-1 infection due to the increase in intracellular metabolism. To test this, we assayed virus replication in CD4⁺ cells isolated pre and post for both the exercise and control sessions for each participant. For each condition, we infected both unstimulated (resting) and cells pre-

Figure 5. Susceptibility to HIV-1 infection was increased in postexercise samples. (A) Example replication curve from one subject. Virus replication is presented as RT activity measured from cell culture supernatants (arbitrary units). (B) Plots show fold changes in HIV-1 replication levels in the activated $CD4^+$ T cells in each subject between control (0.02 ± 0.34) and exercise (0.29 ± 0.38) sessions at 3 days post infection. (C) The median fluorescence intensity (MFI) was determined for CD4 expression (Control: 0.46 ± 1.6, Exercise: 0.61 ± 1.5) following 3 days stimulation with anti-CD3 and anti-CD28. Data are presented as fold change from baseline and visualized as spaghetti plots with each line representing the change between paired samples; $n = 10$. *Indicates a statistically significant difference ($P < 0.05$) from the control session.

activated with CD3/CD28/CD2 beads. The levels of virus replication were measured by quantification of RT activity in cell supernatants collected at various days post infection. Example data for one subject is shown in Figure 5A. Overall, infection of unstimulated, quiescent $CD4^+$ T cells isolated from either the control or exercise session did not produce any significant amount of virus replication, nor were any differences between conditions observed. In activated $CD4^+$ T cells, the RT activity peaked on average at 10 days post infection in cells from either the control or experiment sessions (Fig. 5A), then declined due to virus-induced cell death. The average fold change in RT activity from pre-to-post exercise was calculated for each timepoint. At 3 days post infection, there was significantly greater levels of RT activity in the stimulated cells from the postexercise condition compared to resting controls ($P = 0.03$, Fig. 5B). Notably, there was no significant change in CD4 expression on cells isolated pre or post the control and exercise session at the time of viral infection ($P = 0.84$, Fig. 5C). The Bayesian threshold estimate indicates an 85.8% probability that the true parameter would be a greater than 10% increase in replication. Summary statistical data are shown in Table 1. The increased infection observed in cells obtained post exercise supports the hypothesis that there was increased metabolic activity in $CD4^+$ T cells following acute bouts of resistance exercise.

HIV-1 latent infection in quiescent $CD4^+$ T-cells is not enhanced in cells isolated after an acute bout of resistance exercise

HIV-1 preferentially infects activated $CD4^+$ T cells, but it has been shown that HIV-1 can infect quiescent cells partially activated in the G_{1b} phase of the cell cycle, or cells stimulated with various cytokines, including IL-7 or IL-13 (Unutmaz et al. 1999). These conditions are characterized by increased metabolic activity and levels of RNA expression equal to levels seen in the S phase of cell division (Korin and Zack 1998; Zack et al. 2013). Given that an acute bout of resistance exercise partially increased the activation state of $CD4^+$ T cells in the absence of stimuli, we sought to investigate whether the cells isolated postexercise would support establishment of latent HIV-1 infection. To assess this, the infected quiescent cells from both control and exercise sessions were reactivated at 14 dpi by treatment with CD3/CD28/CD2 activator beads and an additional RT sample collected 3 days post stimulation (17 dpi) to measure for latent virus infection. No significantly different levels of RT activity were observed between either the control or exercise session, suggesting that exercise does not stimulate $CD4^+$ T cells sufficiently enough to support the establishment of HIV-1 latency in $CD4^+$ T cells (data not shown).

Discussion

The present study examined the effect of resistance exercise on $CD4^+$ T cell activation and utilized a viral model to indirectly assess intracellular metabolic activity via viral infection. The changes we observed in CD25 expression on non-stimulated cells suggest that resistance exercise produces an effect on the activation state of $CD4^+$ T cells in previously untrained individuals. Furthermore, the Bayesian analyses suggest a similar exercise-induced increase in CD25 expression in cells responding to stimuli. Together, these findings indicate an increase in cell activation, which is also supported by the in vitro viral model showing a significant increase in viral infection in cells obtained postexercise.

Previous work from our laboratory using an acute bout of moderate intensity aerobic and resistance exercise demonstrated increased activation and proliferation of $CD3^+$ cells following stimulation by either phytohemagglutinin (PHA) or co-stimulation through CD28 (Siedlik et al. 2017). Field studies using elite athletes in competitive trials already demonstrate evidence of increased lymphocyte proliferation following bouts of aerobic exercise (Bassit et al. 2000; Tossige-Gomes et al. 2014). To date, no studies have examined the effect of an acute bout of resistance training on T lymphocyte activation states and only a few have examined the effect of resistance training on lymphocyte proliferative capacity (Dohi et al. 2001; Koch et al. 2001; Potteiger et al. 2001). As an example, Potteiger et al. (2001) observed a statistically significant decrease in lymphocyte proliferation in untrained subjects following an acute bout of lower-limb resistance training. Notably, however, this study along with the field studies mentioned above (Bassit et al. 2000; Tossige-Gomes et al. 2014), quantified proliferation from mixed lymphocyte populations. Moreover, there was no assessment of either CD69 or CD25 expression which complicates any comparison with our results. Indeed, there is substantial ambiguity in the existing literature, which we propose is derived from variability in methods, including lymphocyte isolation protocols and the use of various mitogenic agents [Reviewed in (Siedlik et al. 2016; Campbell and Turner, 2018)]. In this project, we attempted to clarify some of the ambiguity of previous studies by focusing on a specific lymphocyte subset ($CD4^+$ T cells) and utilizing a biological model of infection to assess exercise-induced effects. The use of viral infection and replication as an outcome metric for immune function may seem counterintuitive, but reverse transcription and the process by which HIV integrates into the host genome is dependent upon the metabolic machinery of the cell, providing a unique physiological method to assess exercise-induced alterations in $CD4^+$ T cell metabolic state.

Cells isolated following exercise sessions supported enhanced replication of HIV-1, but statistical significance was observed only at the second timepoint (3 dpi). This is likely because once infection is established, HIV-1 has a logarithmic growth rate until the maximum threshold of virus replication is achieved (Ribeiro et al. 2010). In our experiments, the maximum threshold was typically achieved prior to the 10 dpi timepoint (overall mean = 9.575 $\pm$ 2.0 dpi). Given a constant MOI and no difference in cell surface expression of CD4 between the control and exercise conditions, the exponential growth rate of the viruses likely erased any differences in initial infection by 7 dpi. Nevertheless, the significant difference at 3 dpi demonstrated enhanced infection of the cells isolated postexercise. The significant increase in CD25 expression on nonstimulated cells obtained postexercise independently validated an increase in cellular activation. Combined, these data support the hypothesis that exercise induces an increase in the activation state of $CD4^+$ T cells.

A primary limitation of this study, and of research in exercise immunology in general, centers on the external validity of the results themselves; namely, there is no direct translation from the in vitro assessments to an in vivo model. This is particularly relevant for the current project given the use of virus replication as an outcome measure. A previous study by Roubenoff et al. (1999) investigated alterations in viral RNA concentrations in plasma from HIV-1 infected patients participating in a single bout of aerobic exercise. In their study, untrained, HIV-1 positive individuals completed a 15 min, 60 cm vertical step test at a cadence of 1 step/sec. They found no significant increase in HIV RNA postexercise but speculated that the lack of change might have been due to the relatively high baseline viral loads in most of the subjects (Roubenoff et al. 1999). Similar to the replication threshold we observed at 10 dpi in vitro, the authors (Roubenoff et al. 1999) suspected there was a "ceiling effect," or maximum threshold in replication, that limited exercise-induced changes. Notably, patients with undetectable levels of HIV-1 RNA at the start of the study showed increases in plasma HIV-1 RNA levels postexercise. That result is consistent with the findings of the current study, despite the fact that we assayed virus replication in cells from healthy, uninfected individuals.

Compounding concerns related to in vitro versus in vivo models, the genetic diversity, environmental exposures, and health histories of individuals generate highly varied immune states (Tsang 2015). The innate variability in immune responses in human subjects tends to lead to less conclusive results compared to animal models, curbing enthusiasm for results obtained from human research (Davis 2008). The present study identified small, transient effects representative, in scale, of exercise-induced changes in immune function. In an effort to embrace the observed variation (Gelman and Carlin 2017), the results of Bayesian analyses are provided to illustrate the probability of parameter values given the observed data. Bayesian methods provide a probability distribution for an estimate; meaning, we can assign a probability to our best estimate of the mean difference and all the possible values the parameter may take (Buchinsky and Chadha 2017). This Bayesian estimation provides more informative results about the magnitude of parameters and associated variance beyond that of traditional frequentist statistics (Kruschke 2013). Moreover, we believe that improved assessment and interpretation of variation in studies of human immune responses is needed as medicine shifts

toward personalized, precision care (Tsang 2015; Collins and Varmus 2015).

Overall, these data support the hypothesis that an acute bout of resistance exercise in untrained individuals generates an increase in $CD4^+$ T cell activation even in the absence of stimulation. We also demonstrated the use of an in vitro viral model to quantify a physiological effect, arguing for the use of other pathogens to investigate exercise-induced changes in immune cell subsets. Infectious models, when combined with other stimulation assays, may help clarify the ambiguity in the current literature regarding the effect of exercise on immunity. It is our hope, that future studies using these designs will help advance translational research in exercise immunology and ultimately lead to better informed prescription of clinical exercise.

Conflict of Interest

The authors report no conflict of interest.

References

Bassit, R. A., L. A. Sawada, R. F. Bacurau, F. Navarro, and L. F. Costa Rosa. 2000. The effect of BCAA supplementation upon the immune response of triathletes. Med. Sci. Sports Exerc. 32:1214–1219. PubMed PMID: 10912884.

Buchinsky, F. J., and N. K. Chadha. 2017. To P or Not to P: backing bayesian statistics. Otolaryngol. Head Neck Surg. 157:915–918. https://doi.org/10.1177/0194599817739260. PubMed PMID: 29192853.

Campbell, J. P., and J. E. Turner. 2018. Debunking the myth of exercise-induced immune suppression: redefining the impact of exercise on immunological health across the lifespan. Front. Immunol. 9:648. https://doi.org/10.3389/fimmu.2018.00648. PubMed PMID: 29713319; PubMed Central PMCID: PMCPMC5911985.

Chan, M. A., A. J. Koch, S. H. Benedict, and J. A. Potteiger. 2003. Influence of carbohydrate ingestion on cytokine responses following acute resistance exercise. Int. J. Sport Nutr. Exerc. Metab. 13:454–65. PubMed PMID: 14967869.

Chirathaworn, C., J. E. Kohlmeier, S. A. Tibbetts, L. M. Rumsey, M. A. Chan, and S. H. Benedict. 2002. Stimulation through intercellular adhesion molecule-1 provides a second signal for T cell activation. J. Immunol. 168:5530–5537. PubMed PMID: 12023348.

Cohen, J. 1992. A power primer. Psychol. Bull. 112:155–159. PubMed PMID: 19565683.

Collins, F. S., and H. Varmus. 2015. A new initiative on precision medicine. N. Engl. J. Med. 372:793–795. https://doi.org/10.1056/NEJMp1500523. PubMed PMID: 25635347; PubMed Central PMCID: PMCPMC5101938.

Davis, M. M. 2008. A prescription for human immunology. Immunity 29:835–838. https://doi.org/10.1016/j.immuni.2008.12.003. PubMed PMID: 19100694; PubMed Central PMCID: PMCPMC2905652.

DeBoer, J., M. S. Wojtkiewicz, N. Haverland, Y. Li, E. Harwood, E. Leshen, et al. 2018. Proteomic profiling of HIV-infected T-cells by SWATH mass spectrometry. Virology 516:246–257. https://doi.org/10.1016/j.virol.2018.01.025. PubMed PMID: 29425767; PubMed Central PMCID: PMCPMC5836514.

Dohi, K., A. M. Mastro, M. P. Miles, J. A. Bush, D. S. Grove, S. K. Leach, et al. 2001. Lymphocyte proliferation in response to acute heavy resistance exercise in women: influence of muscle strength and total work. Eur. J. Appl. Physiol. 85:367–373. PubMed PMID: 11560093.

Gelman, A., and J. Carlin. 2017. Some natural solutions to the p-value communication problem—and why they won't work. J. Am. Stat. Assoc. 112:899–901. https://doi.org/10.1080/01621459.2017.1311263.

Gowda, S. D., B. S. Stein, N. Mohagheghpour, C. J. Benike, and E. G. Engleman. 1989. Evidence that T cell activation is required for HIV-1 entry in CD4+ lymphocytes. J. Immunol. 142:773–780. PubMed PMID: 2521508.

Haff, G., and N. T. Triplett. 2016. Essentials of strength training and conditioning. 4th ed. Human Kinetics, Champaign, IL.

Koch, A. J., J. A. Potteiger, M. A. Chan, S. H. Benedict, and B. B. Frey. 2001. Minimal influence of carbohydrate ingestion on the immune response following acute resistance exercise. Int. J. Sport Nutr. Exerc. Metab. 11:149–161. PubMed PMID: 11402249.

Kohlmeier, J. E., M. A. Chan, and S. H. Benedict. 2006. Costimulation of naive human CD4 T cells through intercellular adhesion molecule-1 promotes differentiation to a memory phenotype that is not strictly the result of multiple rounds of cell division. Immunology 118:549–558. https://doi.org/10.1111/j.1365-2567.2006.02396.x. PubMed PMID: 16895560; PubMed Central PMCID: PMCPMC1782322.

Korin, Y. D., and J. A. Zack. 1998. Progression to the G1b phase of the cell cycle is required for completion of human immunodeficiency virus type 1 reverse transcription in T cells. J. Virol. 72:3161–3168. PubMed PMID: 9525642; PubMed Central PMCID: PMCPMC109773.

Kruschke, J. K. 2013. Bayesian estimation supersedes the t test. J. Exp. Psychol. Gen. 142:573–603. https://doi.org/10.1037/a0029146. PubMed PMID: 22774788.

Malek, T. R. 2008. The biology of interleukin-2. Annu. Rev. Immunol. 26:453–479. https://doi.org/10.1146/annurev.immunol.26.021607.090357. PubMed PMID: 18062768.

Manganaro, L., P. Hong, M. M. Hernandez, D. Argyle, L. C. F. Mulder, U. Potla, et al. 2018. IL-15 regulates susceptibility of CD4(+) T cells to HIV infection. Proc. Natl. Acad. Sci. USA 115:E9659–E9667. https://doi.org/10.1073/pnas.1806695115. PubMed PMID: 30257946; PubMed Central PMCID: PMCPMC6187195.

Medzhitov, R. 2007. Recognition of microorganisms and activation of the immune response. Nature 449:819–826.

https://doi.org/10.1038/nature06246. PubMed PMID: 17943118.

Mueller, D. L., M. K. Jenkins, and R. H. Schwartz. 1989. Clonal expansion versus functional clonal inactivation: a costimulatory signalling pathway determines the outcome of T cell antigen receptor occupancy. Annu. Rev. Immunol. 7:445–480. https://doi.org/10.1146/annurev.iy.07.040189.002305. PubMed PMID: 2653373.

Newton, A. H., and S. H. Benedict. 2014. Low density lipoprotein promotes human naive T cell differentiation to Th1 cells. Hum. Immunol. 75:621–628. https://doi.org/10.1016/j.humimm.2014.04.017. PubMed PMID: 24768899.

Nieman, D. C., D. A. Henson, C. S. Sampson, J. L. Herring, J. Suttles, M. Conley, et al. 1995. The acute immune response to exhaustive resistance exercise. Int. J. Sports Med. 16:322–328. https://doi.org/10.1055/s-2007-973013. PubMed PMID: 7558530.

Potteiger, J. A., M. A. Chan, G. G. Haff, S. Mathew, C. A. Schroeder, M. D. Haub, et al. 2001. Training status influences T-cell responses in women following acute resistance exercise. J. Strength Cond. Res. 15:185–191. PubMed PMID: 11710403.

Ribeiro, R. M., L. Qin, L. L. Chavez, D. Li, S. G. Self, and A. S. Perelson. 2010. Estimation of the initial viral growth rate and basic reproductive number during acute HIV-1 infection. J. Virol. 84:6096–6102. https://doi.org/10.1128/JVI.00127-10. PubMed PMID: 20357090; PubMed Central PMCID: PMCPMC2876646.

Roubenoff, R., P. R. Skolnik, A. Shevitz, L. Snydman, A. Wang, S. Melanson, et al. 1999. Effect of a single bout of acute exercise on plasma human immunodeficiency virus RNA levels. J. Appl. Physiol. 86:1197–1201. https://doi.org/10.1152/jappl.1999.86.4.1197. PubMed PMID: 10194203.

Siedlik, J. A., S. H. Benedict, E. J. Landes, J. P. Weir, J. P. Vardiman, and P. M. Gallagher. 2016. Acute bouts of exercise induce a suppressive effect on lymphocyte proliferation in human subjects: a meta-analysis. Brain Behav. Immun. 56:343–351. https://doi.org/10.1016/j.bbi.2016.04.008. PubMed PMID: 27103377.

Siedlik, J. A., J. A. Deckert, S. H. Benedict, A. Bhatta, A. J. Dunbar, J. P. Vardiman, et al. 2017. T cell activation and proliferation following acute exercise in human subjects is altered by storage conditions and mitogen selection. J. Immunol. Methods 446:7–14. https://doi.org/10.1016/j.jim.2017.03.017. PubMed PMID: 28366645.

Stevenson, M., T. L. Stanwick, M. P. Dempsey, and C. A. Lamonica. 1990. HIV-1 replication is controlled at the level of T cell activation and proviral integration. EMBO J. 9:1551–1560. PubMed PMID: 2184033; PubMed Central PMCID: PMCPMC551849.

Tanaka, H., K. D. Monahan, and D. R. Seals. 2001. Age-predicted maximal heart rate revisited. J. Am. Coll. Cardiol. 37:153–156. PubMed PMID: 11153730.

Team, R. C. 2014. R: a language and environment for statistical computing. R Foundation for Statistical Computing, Vienna, Austria.

Testi, R., J. H. Phillips, and L. L. Lanier. 1989. Leu 23 induction as an early marker of functional CD3/T cell antigen receptor triggering. Requirement for receptor cross-linking, prolonged elevation of intracellular [Ca++] and stimulation of protein kinase C. J Immunol. 142:1854–1860. PubMed PMID: 2466079.

Tossige-Gomes, R., V. O. Ottone, P. N. Oliveira, D. J. S. Viana, T. l. Araújo, F. J. Gripp, and et al. 2014. Leukocytosis, muscle damage and increased lymphocyte proliferative response after an adventure sprint race. Braz. J. Med. Biol. Res. 47:492–498. PubMed PMID: 24676476; PubMed Central PMCID: PMC4086176.

Tsang, J. S. 2015. Utilizing population variation, vaccination, and systems biology to study human immunology. Trends Immunol. 36:479–493. https://doi.org/10.1016/j.it.2015.06.005. PubMed PMID: 26187853; PubMed Central PMCID: PMCPMC4979540.

Tzachanis, D., E. M. Lafuente, L. Li, and V. A. Boussiotis. 2004. Intrinsic and extrinsic regulation of T lymphocyte quiescence. Leuk Lymphoma. 45:1959–1967. https://doi.org/10.1080/1042819042000219494. PubMed PMID: 15370239.

Unutmaz, D., V. N. KewalRamani, S. Marmon, and D. R. Littman. 1999. Cytokine signals are sufficient for HIV-1 infection of resting human T lymphocytes. J. Exp. Med. 189:1735–1746. PubMed PMID: 10359577; PubMed Central PMCID: PMCPMC2193071.

Walsh, N. P., M. Gleeson, D. B. Pyne, D. C. Nieman, F. S. Dhabhar, R. J. Shephard, et al. 2011. Position statement. Part two: maintaining immune health. Exerc. Immunol. Rev. 17:64–103 PubMed PMID: 21446353.

Walsh, N. P., M. Gleeson, R. J. Shephard, M. Gleeson, J. A. Woods, N. C. Bishop, et al. 2011. Position statement. Part one: immune function and exercise. Exerc. Immunol. Rev. 17:6–63 PubMed PMID: 21446352.

Yusuf, I., and D. A. Fruman. 2003. Regulation of quiescence in lymphocytes. Trends Immunol. 24:380–386. PubMed PMID: 12860529.

Zack, J. A., S. J. Arrigo, S. R. Weitsman, A. S. Go, A. Haislip, and I. S. Chen. 1990. HIV-1 entry into quiescent primary lymphocytes: molecular analysis reveals a labile, latent viral structure. Cell 61:213–222. PubMed PMID: 2331748.

Zack, J. A., A. M. Haislip, P. Krogstad, and I. S. Chen. 1992. Incompletely reverse-transcribed human immunodeficiency virus type 1 genomes in quiescent cells can function as intermediates in the retroviral life cycle. J. Virol. 66:1717–1725. PubMed PMID: 1371173; PubMed Central PMCID: PMCPMC240919.

Zack, J. A., S. G. Kim, and D. N. Vatakis. 2013. HIV restriction in quiescent CD4(+) T cells. Retrovirology. 10:37. https://doi.org/10.1186/1742-4690-10-37. PubMed PMID: 23557201; PubMed Central PMCID: PMCPMC3626626.

ADVANCED SCIENCE Open Access
www.advancedscience.com

Modularly Programmable Nanoparticle Vaccine Based on Polyethyleneimine for Personalized Cancer Immunotherapy

*Jutaek Nam, Sejin Son, Kyung Soo Park, and James J. Moon**

Nanoparticles (NPs) can serve as a promising vaccine delivery platform for improving pharmacological property and codelivery of antigens and adjuvants. However, NP-based vaccines are generally associated with complex synthesis and postmodification procedures, which pose technical and manufacturing challenges for tailor-made vaccine production. Here, modularly programmed, polyethyleneimine (PEI)-based NP vaccines are reported for simple production of personalized cancer vaccines. Briefly, PEI is conjugated with neoantigens by facile coupling chemistry, followed by electrostatic assembly with CpG adjuvants, leading to the self-assembly of nontoxic, sub-50 nm PEI NPs. Importantly, PEI NPs promote activation and antigen cross-presentation of antigen-presenting cells and cross-priming of neoantigen-specific $CD8^+$ T cells. Surprisingly, after only a single intratumoral injection, PEI NPs with optimal PEGylation elicit as high as ≈30% neoantigen-specific $CD8^+$ T cell response in the systemic circulation and sustain elevated $CD8^+$ T cell response over 3 weeks. PEI-based nanovaccines exert potent antitumor efficacy against pre-established local tumors as well as highly aggressive metastatic tumors. PEI engineering for modular incorporation of neoantigens and adjuvants offers a promising strategy for rapid and facile production of personalized cancer vaccines.

1. Introduction

Therapeutic cancer vaccination aims to activate and augment antitumor T cell immunity by providing antigenic and costimulatory signals to professional antigen-presenting cells (APCs).[1] In particular, neoantigens, produced by genetic alterations occurring in a tumor- and patient-specific manner, can be highly immunogenic as neoantigens are entirely absent in normal cells, thus bypassing central T cell tolerance.[2] Thus, amplifying neoantigen-specific T cells using cancer vaccines offers a promising strategy for improving immunogenicity and selectivity of cancer vaccines.[3] Indeed, neoantigen vaccines based on peptides have recently generated promising clinical outcomes in small cohorts of patients.[4] Although these initial clinical trials provide strong rationale for further development of neoantigen cancer vaccines, these initial studies employing free soluble vaccines exhibited limited efficiency at generating neoantigen-specific T cells, potentially due to rapid clearance of free antigens upon in vivo administration and poor codelivery of antigens and adjuvants to APCs.[5]

Nanoparticle (NP)-based delivery systems have several advantages for cancer vaccination, including improved pharmacological properties, targeted delivery, and controlled and localized release of immunomodulatory agents for efficient modulation of specific immune cells.[6] Various functional NPs based on liposomes, polymers, lipoprotein nanodiscs, and inorganic NPs have been employed to improve innate immune stimulation and induction of antitumor T cell responses,[7] including personalized neoantigen cancer vaccines.[8] However, many NP-based vaccines generally involve complex synthesis steps and postmodification of NPs, thus presenting technical and manufacturing challenges. On the other hand, it is desirable to streamline the manufacturing process of neoantigen-based vaccines so that simple, scalable, affordable production with short turnaround time is feasible for practical neoantigen-based cancer vaccination in the clinic.[9]

Here, we designed a programmable neoantigen cancer vaccine that allows simple and facile modular assembly of defined antigens and adjuvants by exploiting the versatile functionality of polyethyleneimine (PEI) (**Figure 1**). Furthermore, we sought to perform systemic investigation on PEI-based vaccine system for promoting cellular uptake of neoantigens, activation of APCs, and cross-priming of neoantigen-specific T cell responses. Our

Dr. J. Nam, Dr. S. Son
Department of Pharmaceutical Sciences
Biointerfaces Institute
University of Michigan
Ann Arbor, MI 48109, USA
K. S. Park
Department of Biomedical Engineering
Biointerfaces Institute
University of Michigan
Ann Arbor, MI 48109, USA
Prof. J. J. Moon
Department of Pharmaceutical Sciences
Department of Biomedical Engineering
Biointerfaces Institute
University of Michigan
Ann Arbor, MI 48109, USA
E-mail: moonjj@umich.edu

The ORCID identification number(s) for the author(s) of this article can be found under https://doi.org/10.1002/advs.202002577

DOI: 10.1002/advs.202002577

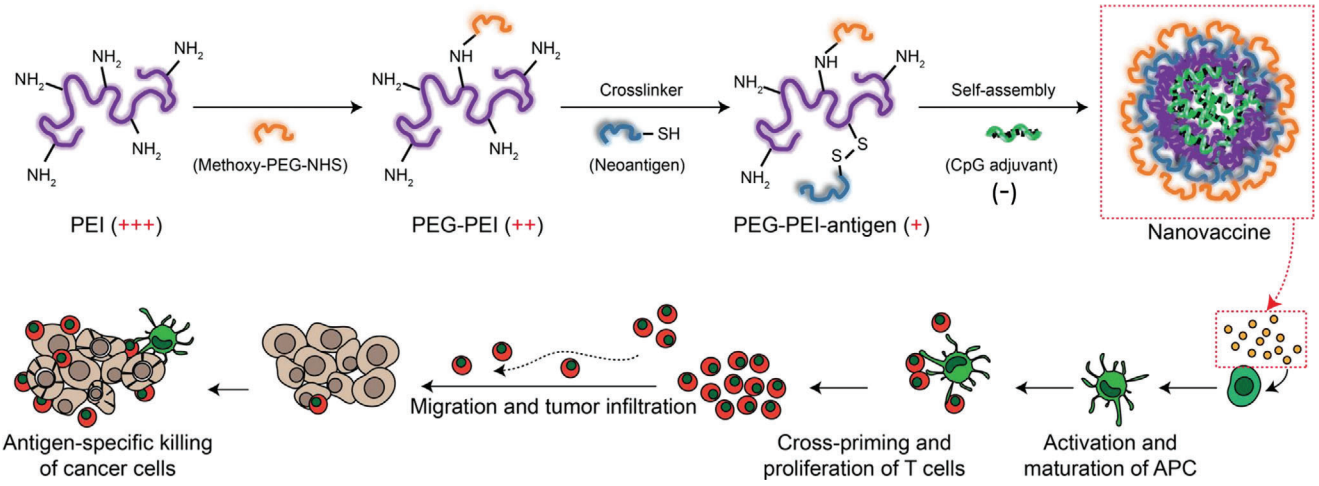

Figure 1. Schematic illustration of PEI-based nanovaccine. PEI was sequentially modified with PEG and neoantigens via amide and disulfide bond, respectively. Then, polycationic PEI conjugates were self-assembled with polyanionic CpG adjuvants through electrostatic interaction to form neoantigen nanovaccine. Diverse types of antigens and adjuvants can be incorporated into the complex allowing flexible and modular design for personalized cancer vaccines. The nanovaccine can increase the cellular uptake of neoantigens and adjuvants by APCs and promote activation and antigen cross-presentation to effectively cross-prime antigen-specific T cells for robust antitumor immunity and antitumor efficacy.

vaccine consists of PEI-antigen conjugates and CpG adjuvants that form compact nano-condensates through electrostatic interaction between polycationic PEI and polyanionic CpG. PEI-antigen is composed of neoantigen peptides conjugated to PEI via a disulfide bond that can be readily cleaved in the highly reductive intracellular environment, thereby promoting cross-presentation by APCs.[8b,d] Subsequently, PEI-antigen conjugates are incubated with CpG to self-assemble into nano-sized particles for efficient codelivery of antigens and adjuvants to APCs – a prerequisite step for optimal T cell priming.[10] Our approach to exploit the intrinsic charge property can avoid complex chemical and structural modifications and preserve immunological activities of antigens and adjuvants to achieve maximum potency.[11] Importantly, we show polyethyleneglycol (PEG) modification as a simple yet powerful strategy to improve the PEI-based nanovaccine for cellular uptake, activation, and antigen cross-presentation of APCs, while eliminating inherent cytotoxicity associated with PEI. The optimized nanovaccines elicited robust priming of antigen-specific $CD8^+$ T cells and exerted strong antitumor efficacy against pre-established local and metastatic tumors, demonstrating their potential for personalized cancer immunotherapy.

2. Results

2.1. PEGylation Reduces Cytotoxicity of PEI–Adpgk Conjugates and Produces Sub-50 nm CpG Complex

We prepared PEI-antigen conjugates by employing an amine-to-sulfhydryl cross-linker that bridges PEI and cysteine-modified peptides through a reducible disulfide bond. As for the choice of antigen, we employed Adpgk peptide which is a neoantigen identified in murine MC38 colon carcinoma.[3b] Specifically, the primary amine of PEI was grafted with the cross-linker to create pyridyldithiol functional groups to which CSS-Adpgk was conjugated to form PEI–Adpgk via disulfide linkage. The feeding amount of the cross-linker and CSS-Adpgk was varied to adjust the density of Adpgk peptide, and the PEI–Adpgk conjugates were analyzed by gel permeation chromatography (GPC) (**Figure 2**A). PEI–Adpgk conjugates displayed strong absorption peaks for Adpgk peptide at ≈15 min, which was absent in plain PEI (labeled as PEI–Adpgk(0)). When the conjugates were treated with dithiothreitol (DTT) reducing agent, the elution time of PEI–Adpgk conjugates was delayed by ≈0.9 min, and their peaks coeluted with free CSS-Adpgk + DTT. These results demonstrated successful conjugation of Adpgk peptide via reduction-sensitive bond, which would allow for the release of intact peptides in a reducing environment. We prepared PEI–Adpgk conjugates with Adpgk/PEI molar ratios of 2, 13, and 30, as determined from the standard curve of CSS-Adpgk + DTT and concentration of Adpgk released from DTT treatment of PEI–Adpgk (Figure S1, Supporting Information). We could not obtain higher Adpgk conjugation as it caused precipitation due to poor solubility in aqueous medium. Since APCs are the first line of immune cells that vaccine formulations should engage for priming antitumor T cell response, we examined PEI–Adpgk conjugates for potential cytotoxicity in bone marrow-derived dendritic cells (BMDCs) (Figure 2B). As PEI is known to be cytotoxic,[12] BMDCs incubated with plain PEI and PEI–Adpgk conjugates exhibited similar levels of cytotoxicity although we observed slightly reduced cytotoxicity for PEI–Adpgk conjugates with Adpgk/PEI ratio ≥ 13.

We sought to reduce the cytotoxicity of PEI–Adpgk by employing PEGylation. PEG–PEI–Adpgk conjugates were synthesized by unsaturated conjugation of methoxy poly(ethyleneglycol) propionic acid *N*-hydroxysuccinimide (methoxy-PEG-NHS) to a portion of the primary amine of PEI, followed by the cross-linker and CSS-Adpgk conjugation as above. For the systemic investigation, we varied the degree of PEGylation by adjusting the stoichiometry of PEG:PEI to 5:1, 10:1, 15:1, or 20:1. The efficiency of PEG conjugation was nearly 100% for all cases as calculated from the unreacted free amine groups quantified using 2,4,6-trinitrobenzene sulfonic acid (data not shown).[13] PEG–PEI–Adpgk conjugates

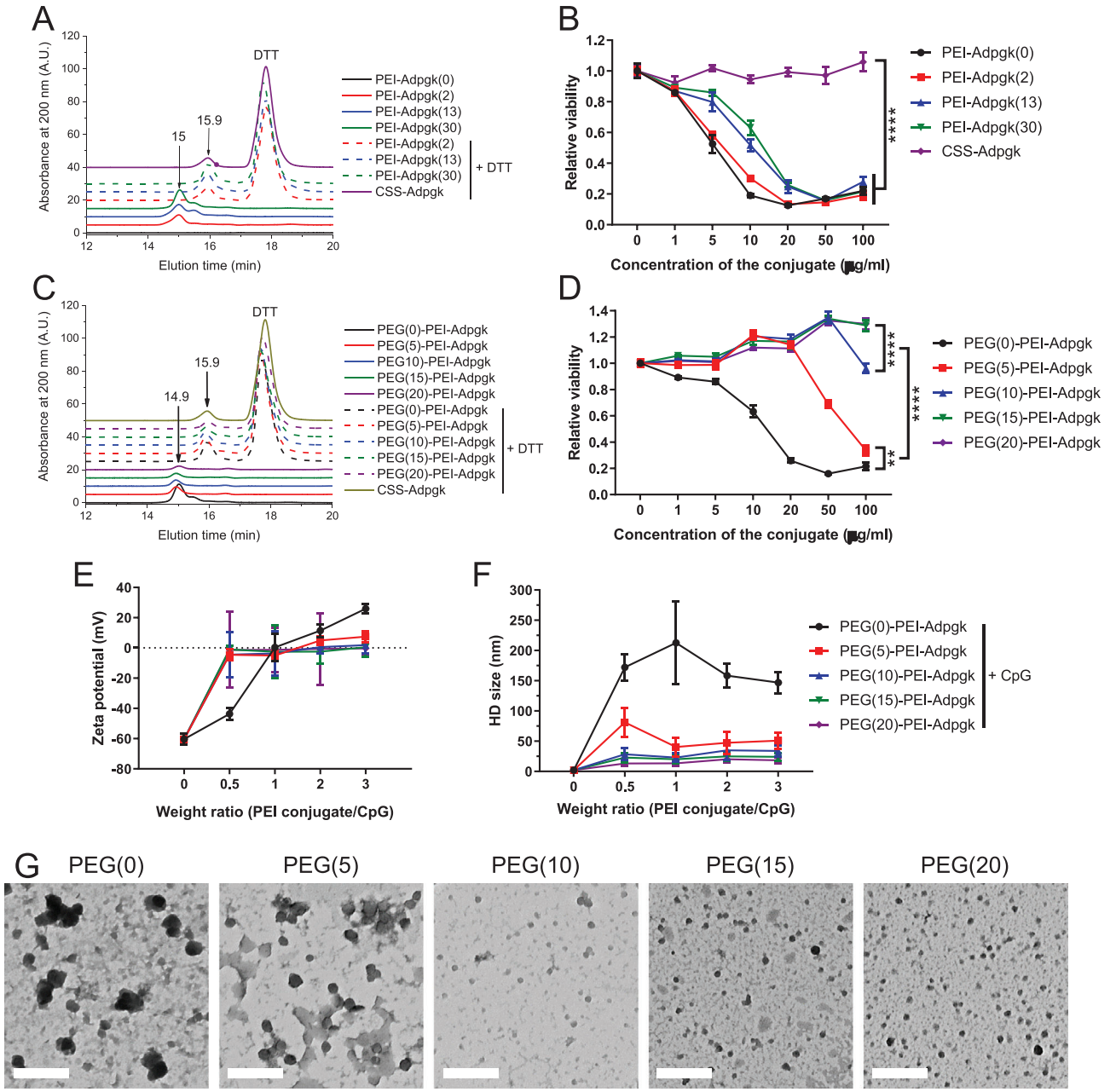

Figure 2. Synthesis and characterization of PEI conjugates and CpG-containing nanovaccines. A–D) GPC spectra of A) PEI–Adpgk conjugates and C) PEG–PEI–Adpgk conjugates measured before and after 10×10^{-3} M DTT treatment, and B, D) their dose-dependent cytotoxicity toward BMDCs assessed after 24 h incubation. The number denotes number of conjugated Adpgk per PEI for PEI–Adpgk conjugates and number of grafted PEG per PEI for PEG-PEI–Adpgk conjugates. E) Zeta potential and F) hydrodynamic size of nanovaccines formed by adding CpG to PEG–PEI–Adpgk conjugates with varying weight ratio. G) TEM images of nanovaccines formulated at a weight ratio of 2 taken after 2% uranyl acetate staining for visualization of their morphology. Scale bars = 200 nm. The data show mean ± s.d. ($n = 5$). $^{**}P < 0.01$ and $^{****}P < 0.0001$, analyzed by two-way ANOVA with Bonferroni multiple comparisons post-test.

were also confirmed using GPC spectra, which showed similar ≈1 min peak shift after DTT treatment (Figure 2C), indicating stable conjugation of Adpgk peptides via disulfide linkage. The ratio of Adpgk:PEI was calculated to be 46, 43, 37, and 33 for PEG(5)-, PEG(10)-, PEG(15)-, PEG(20)-PEI–Adpgk conjugates, respectively. The more PEG grafted, the smaller number of Adpgk was conjugated to PEI, probably due to the steric hindrance of PEG. PEGylation dramatically improved biocompatibility of PEI–Adpgk conjugates with PEG/PEI ≥ 15 exhibiting no cytotoxicity up to 100 μg mL^{-1} and rather promoting cellular proliferation to some extent (Figure 2D). PEGylation was mainly responsible for the reduced cytotoxicity although Adpgk conjugation also partially contributed to it (Figure S2, Supporting Information).

We next investigated PEG–PEI–Adpgk conjugates formulated with CpG. The cationic PEI in PEG–PEI–Adpgk can allow electrostatic assembly and condensation of anionic CpG, confining antigens and adjuvants into nanoparticles (NPs). NPs were formulated by rapid mixing and 1 min incubation of CpG with PEG–PEI–Adpgk conjugates at weight ratios of PEG–PEI–Adpgk/CpG ranging 0.5–3. CpG had a zeta potential of −60 mV from its phosphorothioate backbone units; as the feed amount of PEG–PEI–Adpgk increased, the zeta potential of PEG–PEI–Adpgk/CpG NPs gradually increased toward more positive values (Figure 2E). As CpG was added to PEG(0)–PEI–Adpgk and PEG(5)–PEI–Adpgk, they underwent complete charge conversion to positive at weight ratio > 1, while the conjugates with PEG ≥ 10 remained nearly neutral. These results suggest charge compensation of CpG by PEG–PEI–Adpgk conjugates by electrostatic assembly and passivation of their surface by the nonionic PEG layer. Complete CpG condensation appeared to occur at the PEG–PEI–Adpgk/CpG weight ratio of 2, based on the zeta potential measurement. As shown by the dynamic light scattering (DLS) measurements, the hydrodynamic (HD) size of NPs generally did not change at PEG–PEI–Adpgk/CpG weight ratio ≥ 2, and at the weight ratio of 2, PEG(0)-, PEG(5)-, PEG(10)-, PEG(15)-, and PEG(20)-PEI–Adpgk conjugates formed NPs with HD size of 158 ± 19, 47 ± 18, 35 ± 16, 25 ± 7, and 20 ± 6 nm, respectively (Figure 2F). The negative correlation between PEG density and HD size suggests that PEG passivation promotes formation of small NPs by enhancing their colloidal stability, which is in line with previous reports.[14] We confirmed NP formation with transmission electron microscopy (Figure 2G), which showed the size profiles in alignment with the DLS measurements.

Overall, PEGylation significantly reduced cytotoxicity of PEI–Adpgk conjugates and stabilized their CpG nanocomplex, thereby generating sub-50 nm NPs with a nearly neutral surface charge. The approach presented here allows the synthesis of well-defined PEI-antigen conjugates using facile conjugation chemistry. Subsequently, NPs can be readily produced in a few minutes by simple mixing and brief incubation with molecularly-defined adjuvants. Thus, the PEI-based NP system offers a promising manufacturing strategy for on-demand production of personalized cancer vaccines with a quick turnaround. Based on the zeta potential and HD size measurements, we chose NPs formed at the PEG–PEI–Adpgk:CpG weight ratio of 2:1 for the subsequent studies.

2.2. PEGylation Enhances Cellular Uptake of CpG Nanocomplex and Promotes Activation and Antigen Presentation of BMDCs In Vitro

Next, we sought to investigate how PEGylation impacts on the interactions between nanovaccines and BMDCs. PEG–PEI–Adpgk conjugates and CpG were separately tagged with distinct fluorophores, formulated into NPs, incubated with BMDCs, and visualized to track cellular uptake of each components over time. The doses of PEG–PEI–Adpgk and CpG were fixed at 2 and 1 μg mL^{-1}, respectively. PEGylation decreased cellular uptake of PEI–Adpgk conjugates (without CpG), likely due to the antifouling and stealth feature of PEG (**Figure 3**A).[15] CpG-mediated NP complexation decreased cellular uptake of PEG–PEI–Adpgk conjugates, compared with their respective free polymer form (Figure 3B), and in particular, PEG(0)–PEI–Adpgk exhibited the greatest extent of decrease than others (Figure 3C). Nevertheless, compared with soluble Adpgk + CpG, the nanovaccine formulation markedly enhanced cellular uptake of CpG (Figure 3D), with 30–40-fold increase by PEG(5) NPs; 15–30-fold increase by PEG(10) and PEG(15) NPs; and 2–3-fold increase by PEG(0) and PEG(20) NPs (Figure 3E). Confocal microscopy images taken after 24 h incubation confirmed significant cellular uptake of both PEI–Adpgk conjugates and CpG for PEG(5), PEG(10), and PEG(15) NPs (Figure 3F). In addition, we observed colocalization of PEI–Adpgk conjugates and CpG in the endolysosomal compartments.

Having shown the robust uptake of nanovaccine, we next investigated activation and antigen presentation of BMDCs. We examined nanovaccine-mediated activation of Toll-like receptor (TLR)-9 using a HEK-Blue TLR-9 reporter cell line. When incubated with HEK-Blue TLR-9 cells, PEG–PEI–Adpgk conjugates induced only baseline signal, whereas CpG promoted strong activation of HEK-Blue TLR-9 cells, indicating TLR-9 activation by CpG (**Figure 4**A, B). Whereas PEG(0) NPs showed only a baseline response, PEGylation of NPs significantly elevated TLR9 activation, with PEG ≥ 10 inducing stronger response than free CpG.

Next, we examined how NP formulation impacts antigen presentation by BMDCs. To study this, we employed a model antigen, SIINFEKL peptide, which is an immunodominant MHC-I epitope from ovalbumin. PEG-PEI-SIINFEKL conjugates were synthesized and confirmed using GPC analysis as in Figure 2 (Figure S3, Supporting Information). SIINFEKL nanovaccines formulated with CpG at a weight ratio of 2 were incubated with BMDCs for 24 h, and BMDCs were analyzed for maturation and antigen presentation. Upregulation of CD40, CD80, CD86 costimulatory marker on BMDCs (Figure 4C; Figure S4, Supporting Information) followed a similar pattern as PEG density-dependent increase in TLR-9 activation (Figure 4B), suggesting CpG-mediated BMDC activation. In addition, PEG density also affected antigen presentation on BMDCs, as measured by monoclonal antibody against SIINFEKL/H-$2k^b$ (pMHC) complex (Figure 4D). NPs with higher PEG density generally increased antigen presentation, with PEG(15) NPs inducing 8.4-fold higher pMHC level than soluble SIINFEKL + CpG (Figure 4D). Confocal microscopy also confirmed robust pMHC display on BMDCs treated with PEG(15) NPs, compared with soluble SIINFEKL + CpG control (Figure 4E). In addition, pMHC was mainly localized on the cell surface without much overlap with late endosomes/lysosomes stained with lysosomal associated membrane protein 1 (LAMP-1) (Figure 4E). As PEI-antigen conjugates and CpG were mainly localized in endo-lysosomes (Figure 3F), these results suggest that the nanovaccine promotes intracellular delivery of antigens and CpG and the subsequent steps of cross-presentation, including the intracellular processing of peptide antigen, MHC-loading of epitopes, and trafficking of pMHC to the cell surface.[16] Without CpG, PEG-PEI-SIINFEKL conjugates in the form of free polymers exhibited decreased CD80, CD86, CD40, and pMHC expression as the PEG density was increased (Figure S5, Supporting Information), possibly due to the decreased cellular uptake. This is an opposite trend from the case of nanovaccines, which suggests a unique beneficial role of PEGylation for nanovaccine. Overall, PEGylation on PEI-antigen/CpG

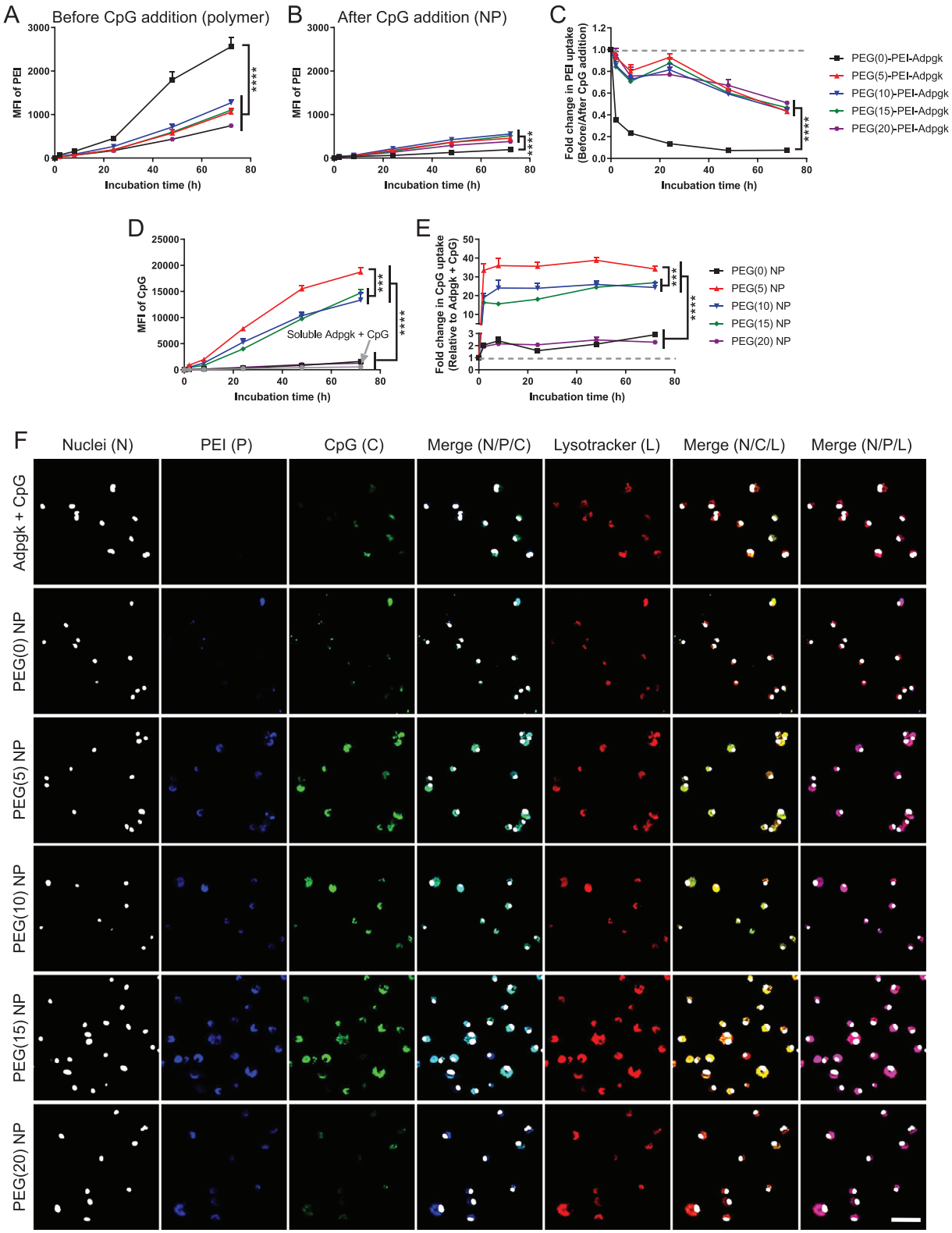

Figure 3. Uptake of nanovaccines by BMDCs. A–C) Time lapse uptake of PEG–PEI–Adpgk conjugates in the form of A) free polymer or B) their nanovaccines formulated by adding CpG measured over 3 days, and C) corresponding fold change in the uptake of PEG–PEI–Adpgk conjugates after CpG addition. D) Time lapse uptake of CpG and E) corresponding fold change in CpG uptake by nanovaccines, compared to soluble Adpgk + CpG. F) Confocal microscope images of BMDCs after 24 h incubation with soluble Adpgk + CpG or nanovaccine samples. Scale bar = 50 µm. The data show mean ± s.d. ($n = 6$). ***$P < 0.001$ and ****$P < 0.0001$, analyzed by two-way ANOVA with Bonferroni multiple comparisons post-test.

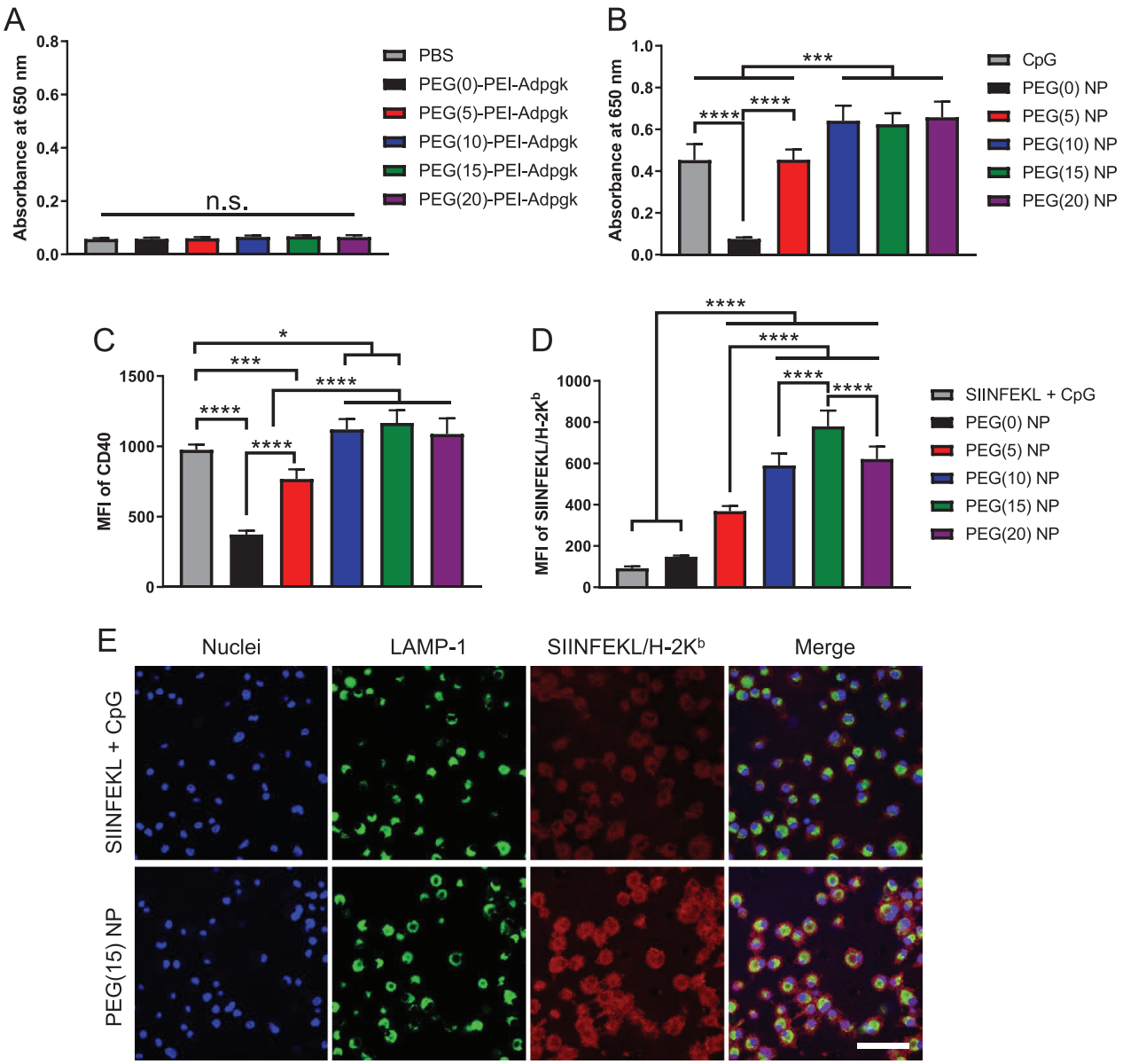

Figure 4. Induction of TLR9-mediated immune stimulation and antigen cross-presentation by nanovaccines. A,B) HEK-Blue TLR9 cells were incubated with A) free polymer form of PEG–PEI–Adpgk conjugates or B) their nanovaccines with CpG, and induction of TLR9 signaling cascade was quantified using 650 nm absorbance. Upregulation of C) CD40 and D) SIINFEKL/H-2K^b expression by BMDCs after 24 h incubation with SIINFEKL + CpG or SIINFEKL nanovaccines. E) Confocal microscope images of BMDCs incubated with SIINFEKL + CpG or PEG(15) NP of SIINFEKL nanovaccine. Scale bar = 50 μm. The data show mean ± s.d. (n = 6). *P < 0.05, ***P < 0.001, and ****P < 0.0001, analyzed by one-way ANOVA with Bonferroni multiple comparisons post-test.

nanovaccines plays a vital role in cellular uptake, adjuvant activity, and antigen cross-presentation, and high PEG density are generally favored for activation of DCs.

2.3. PEGylation Reduces Tumor Retention of Nanovaccine but Elicits Strong Immune Activation in Local Tumor-Draining Lymph Nodes In Vivo

Next, we investigated PEGylation-dependent cellular uptake of nanovaccines in vivo. Tumor tissue consists of a variety of cells tightly organized in a confined volume, and thus provides a suitable biological model for studying complex cellular interactions. Adpgk nanovaccine was tested in a murine tumor model of MC38 colon carcinoma.[3b] We established MC38 colon carcinoma subcutaneously on the right flank of C57BL/6 mice, and vaccines composed of Adpgk peptides and Alexa Fluor 647 (AF647)-tagged CpG were administered directly into tumors. The fluorescence intensity of AF647-CpG measured ex vivo after 24 h revealed that PEG(0) and PEG(5) NPs enhanced tissue retention of CpG (**Figure 5**A), probably due to positive surface charges (Figure 2E). Flow cytometry-based analysis of tumor tissues indicated that

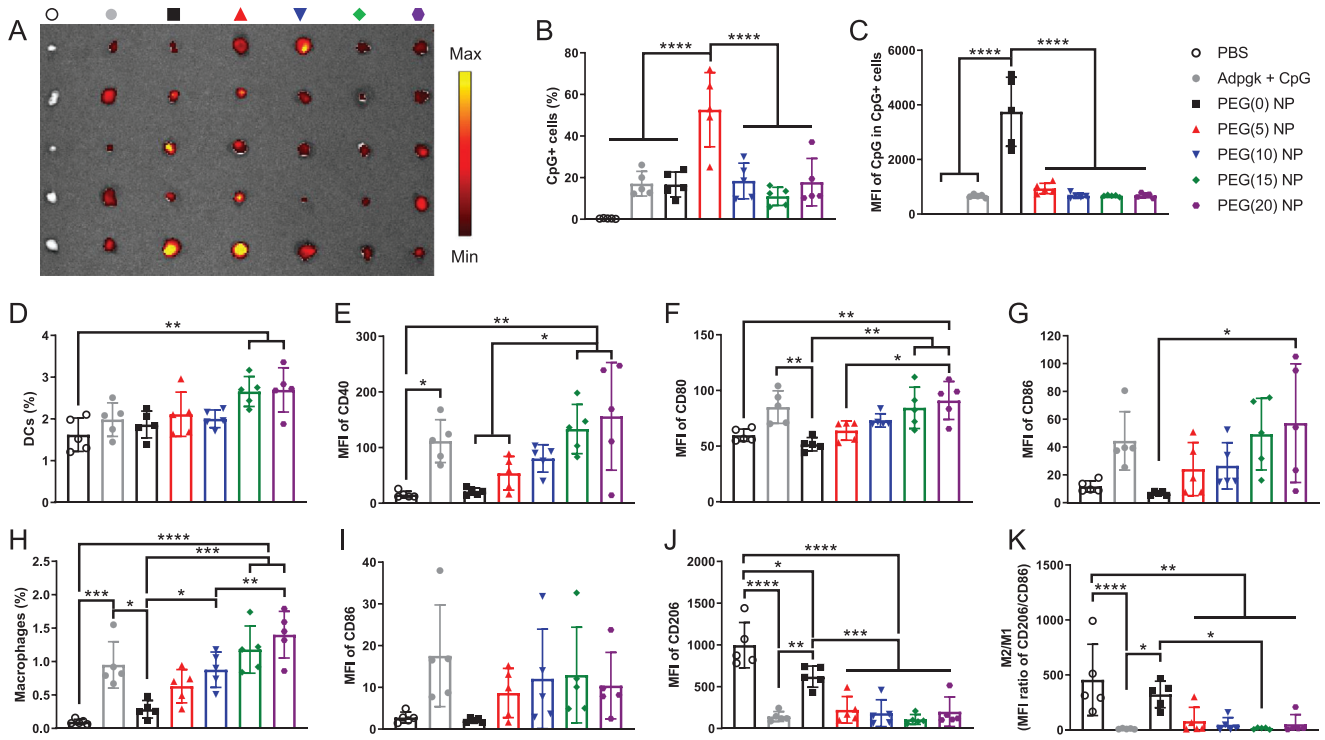

Figure 5. Tumor retention of the nanovaccine and immune activation in tumor-draining LNs. A) Tumor retention of vaccines composed of various forms of Adpgk peptides and AF647-CpG was visualized using ex vivo IVIS imaging after 24 h of intratumoral injection. Quantitative analysis of B) CpG+ cells and C) corresponding MFI of CpG in CpG+ cells in tumors. D–K) Tumor-draining inguinal LNs were analyzed for the number and activation of D-G) DCs and H–K) macrophages. The data show mean ± s.d. ($n = 5$). *$P < 0.05$, **$P < 0.01$, ***$P < 0.001$, and ****$P < 0.0001$, analyzed by one-way ANOVA with Bonferroni multiple comparisons post-test.

PEG(5) NPs were broadly distributed in a larger population of cells, whereas cellular uptake of PEG(0) NPs was mainly restricted to a small subset of cells that internalized NPs to a greater extent (Figure 5B,C). PEG(0) NPs appeared to be rapidly captured by cells at the injection site with limited distribution in the tumor tissues, whereas PEG(5) NPs exhibited increased distribution within the tumor tissues, probably due to the PEG passivation layer. CpG was mainly internalized by tumor cells and macrophages regardless of the formulations (Figure S6, Supporting Information).

Tumor-draining lymph nodes (TDLNs) are critical sites where T-cells are primed for immune activation against tumors.[17] Therefore, we analyzed DCs and macrophages in inguinal TDLNs after intratumoral administration of NPs. First, we confirmed that AF647 conjugation did not compromise the adjuvanticity of CpG using BMDCs in vitro (Figure S7, Supporting Information). PEG(15) and PEG(20) NPs enriched DCs in TDLNs and elevated their expression of CD40, CD80, and CD86 costimulatory markers (Figure 5D–G). In contrast, PEG(0), PEG(5), and PEG(10) NPs induced weaker activation of DCs in TDLNs (Figure 5D–G), suggesting that PEG density on NPs plays a crucial role in DC activation in TDLNs. Similar PEG-dependency was observed for the number of macrophages in TDLNs (Figure 5H), with PEG(15) and PEG(20) NPs significantly increasing macrophages compared with PEG(0) NPs. Compared with PBS and PEG(0) NP, PEGylated NPs as well as the soluble vaccine group upregulated CD86 and downregulated CD206 on macrophages in TDLNs (Figure 5I,J), resulting in a decreased ratio of M2/M1-like macrophages (Figure 5K).[18] We observed similar activation of DCs and macrophages in tumor-draining axillary LNs, but not in contralateral non-tumor-draining inguinal or axillary LNs (Figures S8 and S9, Supporting Information). These results show that a high degree of PEGylation potentiates the performance of nanovaccines upon cellular entry despite the reduction in direct cellular association, which is in agreement with in vitro results.

2.4. Antitumor Immune Response of Nanovaccine against Pre-Established Local Tumor

Having shown the robust activation of DCs and macrophages in TDLNs, we next examined the potency of nanovaccines for priming antitumor T cell response. C57BL/6 mice were subcutaneously inoculated with MC38 cells, administered with Adpgk nanovaccines or soluble Adpgk + CpG on day 9 via intratumoral injection, and analyzed for antitumor immune responses (**Figure 6**A). PEGylated nanovaccines induced robust priming of antigen-specific $CD8^+$ T cells in the systemic circulation, as measured by Adpgk tetramer staining of peripheral blood mononuclear cells (PBMCs) after 7 days of vaccination (Figure 6B). Surprisingly, with only a single injection, PEG(15) and PEG(20) NPs elicited potent neoantigen-specific $CD8^+$ T cell responses against Adpgk, with 5–6-fold higher tetramer+ $CD8^+$ T cells than soluble

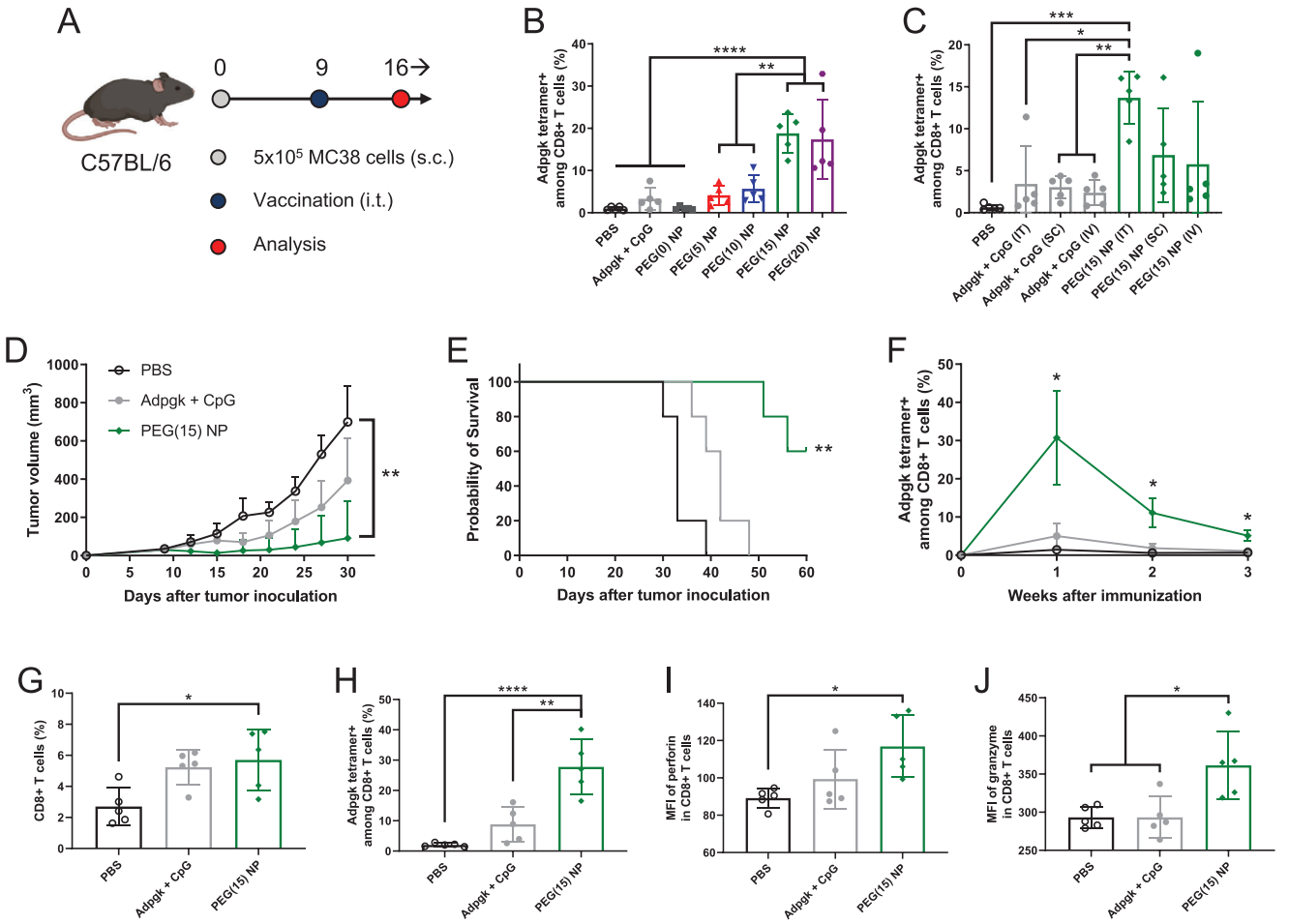

Figure 6. Antitumor immune response of nanovaccine against pre-established local tumors. A) Schematic of treatment regimen. B,C) Adpgk-specific CD8$^+$ T cells in blood were analyzed after B) intratumoral injection of various vaccine formulations or C) administration of Adpgk + CpG versus PEG(15) NP via different routes of vaccination. MC38 tumor-bearing mice were treated by intratumoral administration of Adpgk + CpG versus PEG(15) NP on day 9, and D) tumor growth and E) animal survival were monitored. F) Adpgk-specific CD8$^+$ T cells in blood observed over 3 weeks after single immunization. Tumor microenvironment analysis for the frequency of G) CD8$^+$ T cells and H) Adpgk-specific CD8$^+$ T cells, mean fluorescence intensity (MFI) of I) perforin and J) granzyme in total CD8$^+$ T cells. The data show mean ± s.d. (n = 5). *P < 0.05, **P < 0.01, ***P < 0.001, and ****P < 0.0001, analyzed by one-way (B,C,G,H,I,J) or two-way (D,F) ANOVA with Bonferroni multiple comparisons post-test, or by E) log-rank (Mantel–Cox) test.

Adpgk + CpG (19 ± 4.5 and 17 ± 9.4% vs 3.3 ± 2.5%, $P < 0.0001$, Figure 6B). In contrast, PEG(5) and PEG(10) NPs induced comparable CD8$^+$ T cell responses with soluble Adpgk + CpG, while PEG(0) NP had barely detectable response (Figure 6B).

Based on strong CD8$^+$ T cell response induced by PEG(15) NPs, we focused on PEG(15) NPs and examined how the route of immunization impacts T cell responses. After 9 days of MC38 tumor inoculation, tumor-bearing mice were administered with PEG(15) NPs via intratumoral, subcutaneous (s.c.), or intravenous (i.v.) routes, which resulted in elicitation of 14 ± 3.1, 6.9 ± 5.6, and 5.8 ± 7.4% Adpgk-specific CD8$^+$ T cell response, respectively, on day 16 (Figure 6C). In contrast, soluble Adpgk + CpG induced only 2–4% CD8$^+$ T cell responses regardless of the injection routes. Intratumoral vaccination can be a promising cancer immunotherapy as it can elicit strong antitumor immunity without overt systemic exposure of the vaccines. In fact, there are currently a number of clinical trials evaluating direct intratumoral injection of immunotherapies.[19] Based on these results and considerations, we chose intratumoral administration with PEG(15) NPs for the subsequent antitumor efficacy studies.

C57BL/6 mice were inoculated with MC38 tumor cells on day 0, and a single intratumoral injection of PEG(15) NP was given on day 9. PEG(15) NP effectively suppressed tumor growth (Figure 6D) and eliminated established tumors in 60% mice, leading to significant survival benefit compared with other groups ($P < 0.01$, Figure 6E). In contrast, soluble Adpgk + CpG had only a modest effect with all treated mice succumbing to tumors before day 50. Importantly, a single intratumoral administration of PEG(15) NP led to potent, systemic antitumor CD8$^+$ T cell response, achieving up to ≈30% Adpgk-tetramer+ CD8$^+$ T cell response and sustaining elevated CD8$^+$ T cell response over 3 weeks ($P < 0.05$, Figure 6F), whereas the soluble vaccine group induced weak and transient CD8$^+$ T cell response.

Systemically activated CD8$^+$ T cells need to migrate and infiltrate into the tumor bed in order to recognize and eradicate cancer cells.[20] To investigate tumor homing and cytotoxic activity of

CD8$^+$ T cells, we analyzed the tumor microenvironment after 7 days of PEG(15) NP treatment. PEG(15) NPs promoted tumor infiltration of CD8$^+$ T cells (Figure 6G), with significantly increased frequency of Adpgk-specific CD8$^+$ T cells (28 ± 9.0%), representing 14- and 3.2-fold increases over PBS and soluble Adpgk + CpG, respectively (Figure 6H). Although soluble Adpgk + CpG slightly elevated the frequency of CD8$^+$ T cells in the tumor microenvironment, only a small subset of intratumoral CD8$^+$ T cells was specific to Adpgk peptide, with no statistical difference from that of PBS-treated mice (Figure 6G,H). Intratumoral CD8$^+$ T cells primed with PEG(15) NPs had high expression levels of perforin and granzyme (Figure 6I,J), indicating their cytotoxic potential. On the other hand, we observed minimal activation of CD4$^+$ T cells and NK cells (Figure S10, Supporting Information). Taken together, these results demonstrate that the nanovaccines can induce a robust and durable antitumor response by promoting clonal expansion and tumor infiltration of antitumor CD8$^+$ T cells.

2.5. Nanovaccine against Highly Aggressive and Metastatic Tumor Model

Finally, we sought to evaluate the therapeutic potential of the nanovaccines using B16F10 melanoma, which is a highly aggressive model with poor immunogenicity. To mimic late stage, advanced cancer, we established B16F10 melanoma in both s.c. flank and lung tissues; C57BL/6 mice were inoculated with 3×10^5 B16F10 cells at s.c. flank as well as 4×10^5 B16F10 cells via i.v. administration, leading to the establishment of s.c. flank tumor and lung metastatic nodules (**Figure 7**A). Antitumor efficacy of nanovaccines was examined against both local tumors and disseminated metastases after the vaccine formulations were administered directly into the s.c. flank tumors only. As this model is highly aggressive, we vaccinated animals three times on days 7, 10, and 13. In addition, we utilized recently reported neoantigens identified in B16F10 cells, namely MHC I-restricted M27 and MHC II-restricted M30 neoepitopes, in order to study the effect of combining MHC-I epitope with MHC-II epitope.[3a] PEG(15)-PEI-M27 and PEG(15)-PEI-M30 were synthesized following the established protocol and confirmed using high-performance liquid chromatography (Figure S11, Supporting Information). CpG was added to PEG(15)-PEI-M27 or the mixture of PEG(15)-PEI-M27 and PEG(15)-PEI-M30 conjugates, leading to the formation of PEI-M27 NP and PEI-M27/M30 NP, respectively. Both PEI NPs exhibited similar HD size and zeta potential with nearly neutral surface charge; HD size was measured as 29 ± 8.6 nm and 27 ± 8.2 nm, and zeta potential 6.0 ± 4.7 mV and −1.7 ± 3.9 mV for PEI-M27 NP and PEI-M27/M30 NP, respectively.

Both PEI-M27 NP and PEI-M27/M30 NP treatment groups potently inhibited the growth of primary s.c. flank tumors compared with PBS ($P < 0.01$, Figure 7B) although their antitumor effects were not statistically significant from the soluble vaccine group, probably due to the aggressive nature of this B16F10 model. Importantly, PEI-M27/M30 NP treatment exerted potent systemic antitumor efficacy against B16F10 metastasis, leading to a significantly decreased number of lung metastatic nodules by day 17 (Figure 7C,D). In contrast, all other treatment groups had similar number of lung metastatic nodules as the PBS control. Analysis of splenocytes using interferon (IFN)-γ enzyme-linked immunospot (ELISPOT) assay showed that PEI-M27 NP and PEI-M27/M30 NP significantly enhanced antigen-specific T cell responses against MHC-I-restricted M27 and MHC-II-restricted M30 neoepitopes (Figure 7C,E,F). Soluble formulations induced markedly lower antigen-specific T cell responses. These results suggested that CD8$^+$ T cell response against M27 neoepitope was largely sufficient for suppressing local B16F10 tumors, whereas systemic inhibition of metastasis required both antitumor CD8$^+$ and CD4$^+$ T cells. Interestingly, soluble-M27/M30 treatment induced splenomegaly indicative of systemic inflammation,[5a] whereas PEI-M27/M30 NP and all other treatments showed no change, compared to the PBS control (Figure 6G).

Overall, these results demonstrate that nanovaccines tailored for eliciting a broad spectrum of T cell responses against multiple neoepitopes could effectively treat highly aggressive local and metastatic tumors, while mitigating acute systemic side effects associated with soluble vaccine treatment.

3. Discussion

PEI has been widely exploited as a gene transfection agent as it can form positively charged nanoscale complex with DNA or RNA oligonucleotides to promote their cellular uptake and expression.[21] In addition, PEI can stimulate immune activation by triggering release of "danger signals" or "damage-associated molecular patterns" as the result of cellular stress and damage caused by its cytotoxic actions.[12,22] The ability of PEI to induce inherent immune stimulation and efficient cellular transfection encouraged its development for vaccine applications associated with the delivery of protein- or DNA-based antigens. However, previous studies mostly utilized PEI-based vaccines for treating infectious disease with antibody response,[23] while a handful of cancer applications indicated sub-optimal intrinsic adjuvanticity of PEI for eliciting antitumor T cell response.[24] This has been attributed in part to type 2 T helper cell (Th2)-biased immune activation by PEI, which triggers inflammasome activation and humoral immunity rather than cellular immunity—a crucial criterion for successful cancer vaccination.[23a,b] In addition, transfection of host bystander cells and subsequent cytotoxicity by PEI have been reported to activate T cells against self-antigens, potentially causing immune-related adverse events.[22b,25] In this work, we sought to take advantage of the versatile functionality of PEI for delivery of antigens and adjuvants, while eliminating inherent cytotoxicity of PEI that has hampered cancer vaccine applications. Here, we have shown that PEGylation of PEI formulations significantly decreased cytotoxicity of PEI, while also improving the performance of PEI to deliver exogenous Th1-favored CpG adjuvant along with neoantigens in a spatiotemporally concerted manner. The optimized PEI-based nanovaccines generated robust antigen-specific T cells with a magnitude significantly greater than previously reported PEI-based vaccines,[23–24] suggesting new engineering opportunities of PEI-based vaccines for personalized cancer immunotherapy.

PEG conjugation completely abolished cytotoxicity of PEI at stoichiometry of PEG/PEI ≥ 15, which is in line with previous reports.[14a,26] In addition, PEG can serve as a uncharged spacer unit that provides steric stabilization, decreases nonspecific cellular uptake, and improves in vivo performance for PEI and its

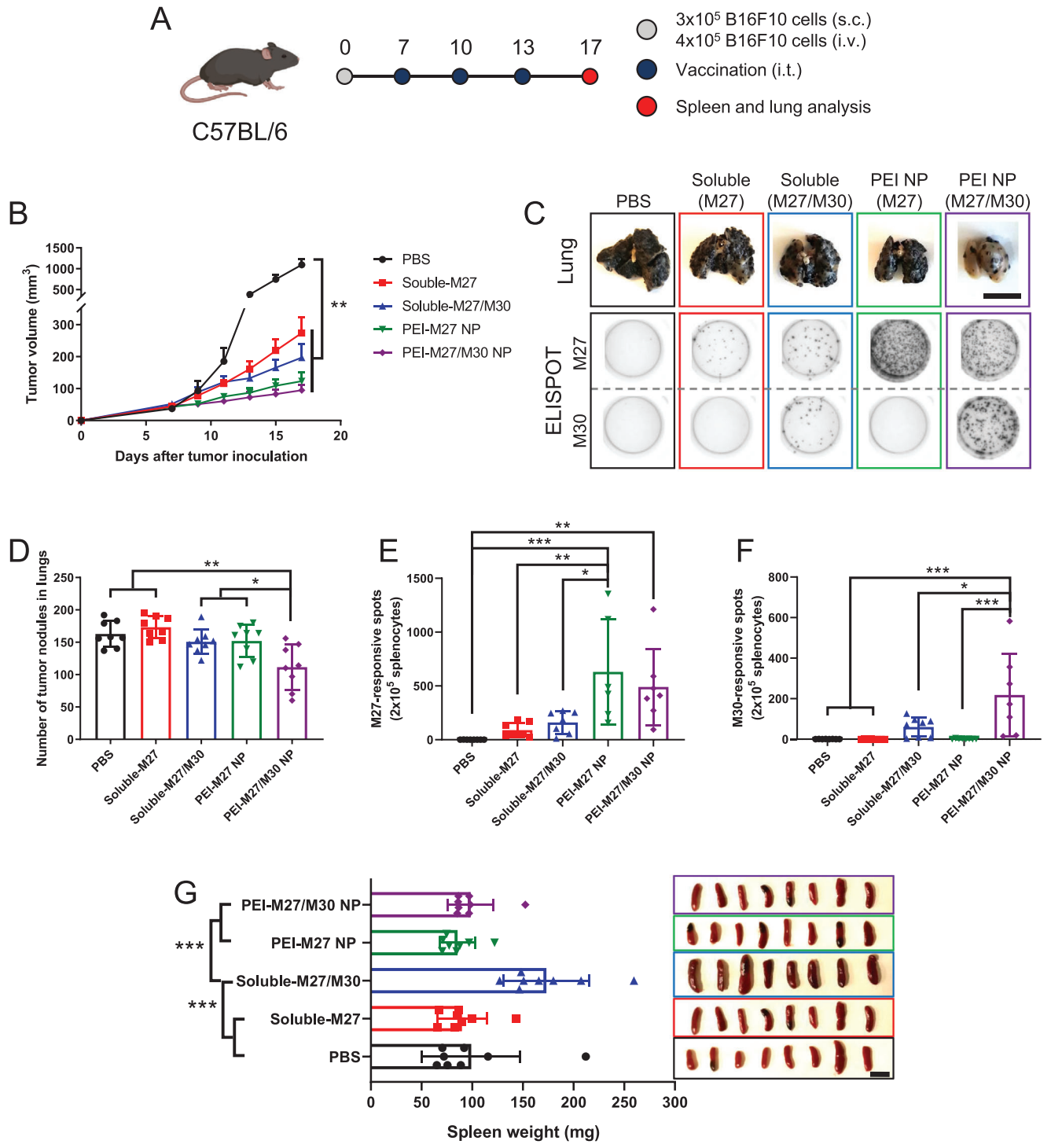

Figure 7. Antitumor immune response of nanovaccine against highly aggressive, disseminated B16F10 melanoma. A) Schematic of treatment regimen. B) Tumor growth curves of subcutaneous flank B16F10 tumors. C) Representative images of lungs and ELISPOT wells. ELISPOT assay was performed after restimulation of splenocytes with M27 or M30. Quantitative analysis of D) lung tumor nodules and ELISPOT counts against E) M27 or F) M30 performed on day 17. G) Weight and images of spleens for assessement of splenomegaly. Scale bars = 1 cm. The data show mean ± s.d. (n = 8). *P < 0.05, **P< 0.01, and ***P < 0.001, analyzed by D–G) one-way or B) two-way ANOVA with Bonferroni multiple comparisons post-test.

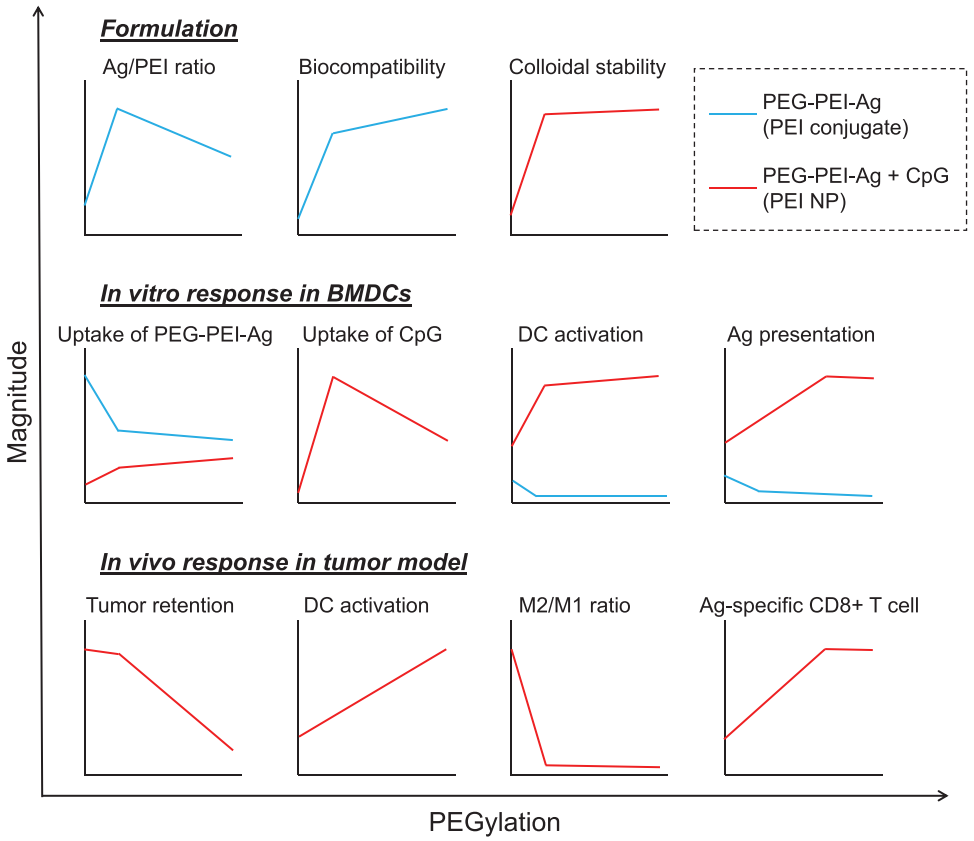

Figure 8. Summary of the impact of PEGylation on PEG-PEI-Ag formulation, in vitro DC activation, and in vivo immune activation.

nano-complex.[27] PEGylation allowed for the formation of sub-50 nm small NPs that significantly enhanced uptake of antigen and adjuvant by APCs. In particular, the uptake of CpG was greatly improved by the nanovaccine formulation, which could be attributed to gaining positive charges from the PEI-antigen conjugate; in return, this caused decreased cellular uptake of PEI-antigen conjugate with the loss of positive charges. Nonetheless, compared with non-PEGylated PEI-antigen/CpG nanocomplex, PEGylated PEI-antigen/CpG nanovaccines increased uptake of both antigen and adjuvant, presumably due to PEG-mediated surface passivation and enhanced colloidal stability. More importantly, the degree of PEGylation had a significant impact on immunological activity of nanovaccines, with higher PEG generally potentiating the vaccine efficacy regardless of the extent of cellular uptake. In vitro, this was clearly demonstrated with PEG(20) NP. Compared with NP formed with lower PEG densities, PEG(20) NP induced the least cellular uptake of PEI-antigen and adjuvant (Figure 3); nevertheless, PEG(20) NP promoted robust TLR-9 signaling (Figure 4B), upregulation of costimulatory markers (Figure 4C), and antigen cross-presentation by DCs (Figure 4D). A similar observation was made in our in vivo studies. Activation of DCs and macrophages in TDLNs (Figure 5D–K) was increased with higher degree of PEGylation although PEGylation reduced cellular association of NPs in the tumor tissues (Figure 5A–C). PEG can not only passivate the surface of nanovaccines but also insert a charge-inert layer during the assembly of PEI-antigen and CpG that weakens electrostatic interaction. We speculate that PEGylation serves multi-purposes; surface-displayed PEG reduces nonspecific cellular uptake while inner PEG layer is thought to facilitate dissociation of the nanocomplexes in the sub-cellular compartments. Efficient liberation of compactly packed nanocomplexes within target cellular compartments is a prerequisite for immune activation, serving as a crucial factor that governs the efficacy of nanovaccines and antitumor T cell responses.[28] Nonetheless, there exists an optimal level of PEGylation for balancing cellular uptake and unpacking of nanocomplexes, as demonstrated by comparable in vitro and in vivo immune activation and T cell responses induced by PEG(15) NP and PEG(20) NP (Figures 4–6) despite significant lower cellular uptake of PEG(20) NP (Figure 3). In contrast, cellular uptake was directly associated with the activity of non-CpG-complexed free PEI-antigen polymers, with PEGylation decreasing cellular uptake and subsequent activation and antigen presentation of BMDCs in vitro (Figure 3A; Figure S5, Supporting Information). Overall, these results suggest that immunological activity of nanovaccine is mainly limited by steric restriction of antigens and adjuvants, which could be improved by PEGylation that facilitates unpacking and liberation of antigens and adjuvants from the nanocomplex. The impact of PEGylation on the various aspects of formulation and performance of PEI-based vaccine is summarized in **Figure 8**.

The optimized nanovaccines allowed a greater amount of antigens and adjuvants to gain entry into cells than soluble vaccines, suggesting that the NP formulation promotes endocytosis/

phagocytosis by DCs.[29] We found that nanovaccines were located in endo-lysosomal compartments (Figure 3F), leading to efficient triggering of the TLR-9 signaling pathway and licensing of DCs for antitumor T cell responses (Figure 4).[30] PEI has been known to mediate endosomal escape and cytosolic drug delivery by trapping endosomal protons, termed proton sponge effect.[31] We speculate that the amount of PEI used for in vitro study (2 μg mL^{-1}) was not sufficient to induce endosomal rupture via proton sponge effect. Nonetheless, we observed efficient cross-presentation of endo-lysosomally delivered antigens (Figure 4D,E). Thus, PEI NP-mediated synchronous delivery of antigen and CpG to the endo-lysosomal compartment could efficiently license DCs for cross-priming of T cells. We speculate that PEI NP-mediated antigen processing and MHC class I presentation occurs in endocytic compartments via vacuolar pathways,[32] which could be further augmented by endosomal TLR signaling[10a] and phagosomal MHC I delivery.[33] Indeed, clonal expansion of antigen-specific $CD8^+$ T cells elicited by nanovaccines of varying PEG density (Figure 6B) followed the pattern of activation and maturation of DCs examined in vitro (Figure 4C) and in vivo (Figure 5E–G), supporting the link between DCs and T cells. Soluble vaccine induced significantly lower antigen-specific $CD8^+$ T cells than the nanovaccine (Figures 6 and 7) despite substantial induction of costimulatory markers on DCs (Figure 5). This suggests that soluble vaccines, which suffer from limited codelivery of antigens and adjuvants to the endo-lysosomes (Figure 3D–F), have a poor antigen cross-presentation as a major limitation for cancer vaccines (Figure 4D).[10] We speculate that antigen availability may also be linked to the superiority of intratumoral vaccination to other administration routes (Figure 6C). Serving as an in situ antigen source, tumor tissue could supply endogenous tumor antigens that could be captured by or drained together with the vaccines after intratumoral injection, increasing antigen availability for vaccine-primed DCs.[34] Intratumoral injection of nanovaccines can also offer safe cancer immunotherapy by mitigating the systemic inflammation associated with the soluble vaccine (Figure 7G). With the optimal formulation and administration route, the nanovaccine developed in this study elicited remarkable $CD8^+$ T cell responses and exerted robust antitumor efficacy in multiple murine tumor models, including advanced metastatic melanoma.

4. Conclusion

We have developed a personalized cancer vaccine based on PEI that allows nanoscale assembly of neoantigens and adjuvants with facile chemical modification and simple electrostatic interaction. The nanovaccine promoted activation and antigen cross-presentation of APCs with efficient codelivery of immunologically active neoantigens and adjuvants, eliciting robust antitumor T cell immunity and antitumor efficacy against pre-established local and metastatic tumors. Our approach allows modular incorporation of neoantigens and ajuvants for rapid and facile production of potent cancer nanovaccines. Our approach outlined here may offer a promising strategy for personalized cancer vaccination.

5. Experimental Section

Reagents and Instruments: Polyethyleneimine (PEI, branched, M_w 25000), 3-(2-pyridyldithio)propionic acid *N*-hydroxysuccinimide ester (SPDP) were obtained from Sigma-Aldrich. Methoxy poly(ethyleneglycol) propionic acid *N*-hydroxysuccinimide (Methoxy-PEG-NHS, M_w 5000) was purchased from Nanocs. CpG1826 was obtained from Integrated DNA Technology. Antigen peptides used in this study were synthesized by Genemed Synthesis, which include epitopes of ovalbumin peptide SIINFEKL and CSSSIINFEKL, neo-epitopes of MC38 colon carcinoma ASMTNMELM (Adpgk) and CSSASMTNMELM (CSS-Adpgk), neo-epitopes of B16F10 melanoma LCPGNKYEM (M27), VDWENVSPELNSTDQ (M30), and CSSVDWENVSPELNSTDQ (CSS-M30). All other reagents were received from Fisher scientific unless otherwise indicated. UV–Vis absorption and fluorescence spectra were obtained using BioTek synergy neo microplate reader. GPC and HPLC were performed using Shimadzu HPLC system equipped with TSKgel G3000SWxl column (Tosoh Bioscience LLC) and Jupiter® C18 LC Column (Phenomenex), respectively. TEM images were acquired using JEOL 1400-plus. Hydrodynamic size and zeta potential were measured using Zetasizer Nano ZSP (Malvern Panalytical). Flow cytometry was performed using ZE5 Cell Analyzer (Bio-Rad) and the data were analyzed using FlowJo 10.5 software.

Preparation of PEI Conjugates and Nanovaccines: For PEI–Adpgk, 10 mg of PEI dissolved in 1 mL DMSO was mixed with SPDP crosslinker and stirred for 3 h, followed by the addition of CSS-Adpgk. The amount of SPDP/CSS-Adpgk was 1.3/1.1, 3.2/2.9, 6.4/5.8 μmol for PEI–Adpgk(2), PEI–Adpgk(13), PEI–Adpgk(30), respectively. After overnight reaction, PEI–Adpgk(2) remained dispersed while PEI–Adpgk(13) and PEI–Adpgk(30) formed off-white particulates. To get rid of unreacted SPDP and CSS-Adpgk, the crude mixture of PEI–Adpgk(2) was dialyzed 3 times against deionized (DI) water using Amicon ultra 10 kDa M_w cutoff centrifugal filters, while PEI–Adpgk(13) and PEI–Adpgk(30) were washed 3 times with DMSO by successive centrifugations. For PEG-PEI-antigen, PEI was first conjugated with Methoxy-PEG-NHS at varying stoichiometry, followed by antigen conjugation using SPDP crosslinker. Briefly, 5 mg of PEI dissolved in 1 mL DMSO was reacted overnight with 5, 10, 15, 20 mg of Methoxy-PEG-NHS for PEG(5)-PEI, PEG(10)-PEI, PEG(15)-PEI, PEG(20)-PEI, respectively. The conjugation was quantified by measuring primary amine contents of PEI using 2,4,6-trinitrobenzene sulfonic acid according to the manufacturer's instruction. Then, SPDP/antigens were reacted as above with their amounts at 6.4/5.8 μmol. Antigen peptides employed for PEG-PEI-antigen conjugates include CSS-Adpgk, CSSSIINFEKL, M27, and CSS-M30. In some cases, 130 μg of Alexa Fluor® 488 NHS Ester (AF488-NHS, Invitrogen) was added along with SPDP for fluorophore labeling of PEI. The crude mixtures were remained dispersed and purified by 3 rounds of dialysis using Amicon ultra 10 kDa M_w cutoff centrifugal filters. The final products were freeze-dried and then re-dispersed in DI water at 5 or 2 mg mL^{-1}. For fluorophore labeling of CpG, 5′ phosphate group of CpG was first tethered with ethylenediamine via the 1-ethyl-3-(3-dimethylaminopropyl)carbodiimide coupling reaction in methyl imidazole buffer, followed by reaction with Alexa Fluor® 647 NHS Ester (AF647-NHS, Invitrogen) as described before.[35] For the construction of nanovaccine, 15 μg of CpG dispersed in 50 μl PBS was quickly added to 7.5, 15, 30, or 45 μg of PEI conjugates diluted in 50 μl PBS for weight ratio of PEI conjugate/CpG 0.5, 1, 2, 3, repectively. The solutions were vigorously mixed for 1 min at room temperature and stored at 4 °C before use.

In Vitro Cell Experiments: BMDCs were collected from C57BL/6 mice and maintained in the medium of RPMI 1640 supplemented 10% fetal bovine serum, 1% penicillin–streptomycin, 20 ng mL^{-1} granulocyte macrophage colony-stimulating factor (Genscript), and 50×10^{-6} M β-mercaptoethanol according to the literature.[36] Immature BMDCs were plated at a density of 1×10^5 cells/well in 96 well plates and incubated overnight at 37 °C under 5% CO_2. For the cytotoxicity study, BMDCs were incubated with PEI–Adpgk conjugates or CSS-Adpgk for 24 h, with the dose at 1, 5, 10, 20, 50, 100 μg mL^{-1}. Then, Cell Counting Kit-8 solution was added to each well of the plate according to manufacturer's instruction (Dojindo Laboratories, Japan). After 2 h, absorbance at 450 nm was measured using a microplate reader to calculate relative viability as

the ratio of the absorbance to the nonsample treated cells. For the cellular uptake study, BMDCs were incubated with PEI–Adpgk/AF488 conjugates or their NPs with CpG-AF647 at dose of 20 μg mL^{-1} PEI conjugates (10 μg mL^{-1} for free Adpgk) and/or 10 μg mL^{-1} CpG. At the indicated time points, cells were collected, washed with FACS buffer (1% BSA in PBS), and then subjected to flow cytometry for measuring fluorescence signals. To visualize cellular localization, BMDCs were grown onto 12 mm glass coverslips in 24 well plates at a density of 5×10^5 cells/well and treated with samples as above for 24 h. Cells were further incubated with Hoechst 33342 (5 μg mL^{-1}, Invitrogen) and Lysotracker Red DND-99 (100 nM, Invitrogen) for 30 min for the staining of nuclei and endolysosomes, respectively. Then, cells were fixed with 4% formaldehyde in PBS and mounted on slide glass using ProLong™ Diamond Antifade Mountant (Invitrogen) for confocal microscopy (Nikon A1Rsi). For TLR-9 signaling study, HEK-blue TLR-9 cells (Invivogen) were treated with PEI–Adpgk conjugates or their NPs at the dose of 2 μg mL^{-1} PEI conjugates and 1 μg mL^{-1} CpG in HEK-Blue Detection medium. After 8 h, absorbance at 650 nm was measured using a microplate reader to analyze induction of TLR-9 signaling in the cells, with the correction of the sample effect by subtracting the absorbance of samples without TLR-9 cells. For the analysis of activation and antigen cross-presentation, BMDCs were incubated with PEI-SIINFEKL conjugates or their NPs for 24 h, with the dose at 2 μg mL^{-1} PEI conjugates or free SIINFEKL and 1 μg mL^{-1} CpG. Cells were collected, washed with FACS buffer, incubated with CD16/32 FcR blocking antibody (Invitrogen, No. 14016186) for 10 min, and then stained with antibody-fluorophore conjugates including CD80-FITC (BD Biosciences, No. 553768), CD86-PE/Cy7 (BD Biosciences, No. 560582), CD40-APC (Invitrogen, No. 17040182) and SIINFEKL/H-$2k^b$-PE (Invitrogen, No. 12574382) for 30 min at room temperature. After wasing with FACS buffer, cell were analyzed using flow cytometry. To visualize antigen cross-presentation, BMDCs were grown onto 12 mm glass coverslips in 24 well plates at a density of 5×10^5 cells/well, treated with samples for 24 h, and further incubated with Hoechst 33342 for 30 min. Then, cells were incubated with CD16/32 FcR blocking antibody, permeabilized with Cytofix/Cytoperm Fixation/Permeabilization Solution (BD Biosciences), and antibody-stained with SIINFEKL/H-$2k^b$-biotin (Invitrogen, No. 13574381) and LAMP1-AF488 (Invitrogen, No. 53107182). After further staining with streptavidin-AF594 (Molecular Probes, No. S32356), cells were washed with PBS and mounted on slide glass using ProLong™ Diamond Antifade Mountant for confocal microscopy.

In Vivo Tumor Retention and Lymph Node Draining Studies: Animals were cared for following the federal, state, and local guidelines. The University of Michigan, Ann Arbor is an AAALAC international accredited institution, and all work conducted on animals was in accordance with and approved by the Institutional Animal Care and Use Committee (IACUC) with the protocol # PRO00008587. Female C57BL/6 mice (5–6 weeks) were purchased from Jackson Laboratory (USA). C57BL/6 mice were subcutaneously inoculated with 5×10^5 MC38 cells into the right flank and randomly sorted for treatment after 9 days when tumor size reached approximately 5 mm. The mice were administered intratumorally with 50 μl PBS solution of Adpgk vaccine formulations with CpG-AF647 at the dose of 30 μg PEI–Adpgk conjugates (equivalent of 10 μg for free Adpgk) and 15 μg CpG. For the analysis of tumor retention, tumors were excised 24 h after sample administration and their fluorescence intensity was measured using IVIS optical imaging system (Caliper Life Sciences). For uptake in a cellular level, tumors were cut into small pieces, incubated with 1 mg mL^{-1} of collagenase type IV and 0.1 mg mL^{-1} of DNase I in RPMI for 30 min at 37 °C, and filtered through a 70-μm strainer. The obtained single cell suspension was washed with FACS buffer, and their fluorescence signal was measured using flow cytometry. For the analysis of DCs and macrophages in lymph node, inguinal and axillary lymph nodes were collected 24 h after sample administration, ground with the rubber end of a syringe, and filtered through a 70-μm strainer. The cell suspension was washed with FACS buffer, incubated with CD16/32 FcR blocking antibody, and stained with the following antibody-fluorophore conjugates; CD80-FITC (BD Biosciences, No. 553768), CD40-PE (Invitrogen, No. 12040183), CD86-PE/Cy7 (BD Biosciences, No. 560582), CD11c-APC (BioLegend, No. 117309) for CD11c+ DCs, and CD11b-PE (Invitrogen, No. 12011282), F4/80-APC (BioLegend, No. 123116), CD86-PE/Cy7 (BD Biosciences, No. 560582), CD206-APC/Cy7 (BioLegend, No. 321120) for CD11b+F4/80+ macrophages. All flow cytometry was performed after suspending cells in DAPI solution for counting only DAPI-negative live and intact cells.

In Vivo Cancer Therapy: For MC38 tumor study, C57BL/6 mice were subcutaneously inoculated with 5×10^5 MC38 cells into the right flank and randomly sorted for treatment after 9 days. The mice were intratumorally administered with 50 μl PBS solution of Adpgk vaccine formulations at the dose of 30 μg PEI–Adpgk conjugates (equivalent of 10 μg for free Adpgk) and 15 μg CpG. In some cases, samples were administered into tail-base subcutaneous site for subcutaneous injection or tail-vein for intravenous injection (100 μl in PBS). For analysis of neoantigen-specific $CD8^+$ T cells in systemic circulation, submandibular bleeding was performed at the indicated time points and PBMCs were collected after removing red blood cells using ACK lysis buffer. PBMCs were incubated with CD16/32 FcR blocking antibody and then stained with Adpgk peptide-MHC tetramer tagged with PE (H-$2D^b$-restricted ASMTNMELM, NIH Tetramer Core Facility) and anti-CD8-APC (BD Biosciences, No. 553035). For analysis of tumor infiltrating lymphocytes, tumor tissues were collected 7 days after sample administration, cut into small pieces, treated with 1 mg mL^{-1} of collagenase type IV and 0.1 mg mL^{-1} of DNase I in RPMI for 30 min at 37 °C, and filtered through a 70-μm strainer. Then, the cell suspension was washed with FACS buffer, incubated with CD16/32 FcR blocking antibody, and stained with the following antibody-fluorophore conjugates; Perforin-FITC (Invitrogen, No. 11939280), Granzyme-PE/Cy7 (Invitrogen, No. 25889882), CD45-PerCP/Cy5.5 (Invitrogen 45045182), Adpgk peptide-MHC tetramer-PE, CD8-APC for $CD8^+$ T cells, Perforin-FITC, Granzyme-PE/Cy7, CD45-PerCP/Cy5.5, NK1.1-PE (Invitrogen, 12594182) for NK cells, and CD45-PerCP/Cy5.5, Foxp3-PE/Cy7 (Invitrogen, No. 25577382) CD4-APC (Invitrogen, No. 17004282) for $CD4^+$ T cells and $CD4^+$Foxp3+ Tregs. Flow cytometry was performed after suspending cells in DAPI solution and gating out DAPI-positive populations. For B16F10 tumor study, C57BL/6 mice were injected with 3×10^5 B16F10 cells subcutaneously into the right flank and 4×10^5 B16F10 cells intravenously into tail vein, for locally established tumors and lung metastasis, respectively. The subcutaneous tumors were subjected to intratumoral administration of samples in 50 μl PBS, with the dose at 15 μg PEI-M27 conjugate (equivalent of 3.5 μg for free M27) and 7.5 μg CpG for M27 vaccine and 15 μg PEI-M27 conjugate, 15 μg PEI-M30 conjugate (equivalent of 5.5 μg for free M30), and 15 μg CpG for M27/M30 vaccine. Animals were randomly sorted on day 7 and received samples every 3 days for total 3 times, followed by euthanization on day 17 for the analysis of splenocyte ELISPOT and lung metastasis. For ELISPOT assay, spleens were ground with the rubber end of a syringe, filtered through a 70-μm strainer, and treated with ACK lysis buffer for removing red blood cells. The obtained splenocytes were plated at 2×10^5 cells/well in 96-well PVDF plates pre-coated with IFN-γ antibody (BD Biosciences), and re-stimulated overnight with 10 μg mL^{-1} of M27 or M30 peptide. Then, the wells were sequentially treated with biotinylated-secondary antibody, streptavidin alkaline phosphatase, and AEC Substrate (BD Biosciences). The developed spots were counted using AID iSpot Reader (AID GmbH, Germany). For the analysis of lung metastasis, lungs were excised, fixed overnight in 4% formaldehyde, and then B16F10 lung tumor nodules were enumerated manually. The sizes of locally established tumors were measured twice a week using a digital caliper, and the tumor volume was estimated by ellipsoidal calculation as $V = (\text{width})^2 \times \text{length} \times 1/2$. The mice were euthanized when the tumors reached the maximum permitted size (1.5 cm in any dimension) or ulcerations occurred.

Statistical Analysis: For animal studies, the mice were randomized to match similar average volume of the locally established tumors. The data show mean ± s.d. (n = 5–8). Data were approximately normally distributed and variance was similar between the groups. Statistical analysis was performed with Prism 8.1.0 software (GraphPad Software) by one-way or two-way ANOVA with Bonferroni multiple comparisons post-test. Statistical significance for survival curve was calculated by the log-rank (Mantel–Cox) test. All data were included for the statistical analysis with the significance indicated as $*P < 0.05$, $**P < 0.01$, $***P < 0.001$, and $****P < 0.0001$.

Supporting Information

Supporting Information is available from the Wiley Online Library or from the author.

Acknowledgements

J.N. and S.S. contributed equally to this work. This work was supported in part by NIH (Grant Nos. R01EB022563, R01AI127070, R01CA210273, R01DK125087, and U01CA210152), MTRAC for Life Sciences Hub, and Emerald Foundation. J.J.M. was supported by DoD/CDMRP Peer Reviewed Cancer Research Program (Grant No. W81XWH-16-1-0369) and NSF CAREER Award (Grant No. 1553831). K.S.P. acknowledges financial support from the UM TEAM Training Program (DE007057 from NIDCR). The authors acknowledge the NIH Tetramer Core Facility (contract HHSN272201300006C) for provision of MHC-I tetramers. Opinions interpretations, conclusions, and recommendations are those of the author and are not necessarily endorsed by the Department of Defense. The authors thank Marisa Aikins for critical review of the manuscript.

Conflict of Interest

The authors declare no conflict of interest.

Keywords

cancer vaccines, immunotherapy, nanoparticles, neoantigens

Received: July 8, 2020
Revised: October 30, 2020
Published online: January 6, 2021

[1] S. H. van der Burg, R. Arens, F. Ossendorp, T. van Hall, C. J. M. Melief, *Nat. Rev. Cancer* **2016**, *16*, 219.

[2] a) T. N. Schumacher, R. D. Schreiber, *Science* **2015**, *348*, 69; b) L. Scheetz, K. S. Park, Q. Li, P. R. Lowenstein, M. G. Castro, A. Schwendeman, J. J. Moon, *Nat. Biomed. Eng.* **2019**, *3*, 768.

[3] a) S. Kreiter, M. Vormehr, N. van de Roemer, M. Diken, M. Löwer, J. Diekmann, S. Boegel, B. Schrörs, F. Vascotto, J. C. Castle, A. D. Tadmor, S. P. Schoenberger, C. Huber, Ö. Türeci, U. Sahin, *Nature* **2015**, *520*, 692; b) M. Yadav, S. Jhunjhunwala, Q. T. Phung, P. Lupardus, J. Tanguay, S. Bumbaca, C. Franci, T. K. Cheung, J. Fritsche, T. Weinschenk, Z. Modrusan, I. Mellman, J. R. Lill, L. Delamarre, *Nature* **2014**, *515*, 572.

[4] a) P. A. Ott, Z. Hu, D. B. Keskin, S. A. Shukla, J. Sun, D. J. Bozym, W. Zhang, A. Luoma, A. Giobbie-Hurder, L. Peter, C. Chen, O. Olive, T. A. Carter, S. Li, D. J. Lieb, T. Eisenhaure, E. Gjini, J. Stevens, W. J. Lane, I. Javeri, K. Nellaiappan, A. M. Salazar, H. Daley, M. Seaman, E. I. Buchbinder, C. H. Yoon, M. Harden, N. Lennon, S. Gabriel, S. J. Rodig, D. H. Barouch, J. C. Aster, G. Getz, K. Wucherpfennig, D. Neuberg, J. Ritz, E. S. Lander, E. F. Fritsch, N. Hacohen, C. J. Wu, *Nature* **2017**, *547*, 217; b) U. Sahin, E. Derhovanessian, M. Miller, B.-P. Kloke, P. Simon, M. Löwer, V. Bukur, A. D. Tadmor, U. Luxemburger, B. Schrörs, T. Omokoko, M. Vormehr, C. Albrecht, A. Paruzynski, A. N. Kuhn, J. Buck, S. Heesch, K. H. Schreeb, F. Müller, I. Ortseifer, I. Vogler, E. Godehardt, S. Attig, R. Rae, A. Breitkreuz, C. Tolliver, M. Suchan, G. Martic, A. Hohberger, P. Sorn, J. Diekmann, J. Ciesla, O. Waksmann, A.-K. Brück, M. Witt, M. Zillgen, A. Rothermel, B. Kasemann, D. Langer, S. Bolte, M. Diken, S. Kreiter, R. Nemecek, C. Gebhardt, S. Grabbe, C. Höller, J. Utikal, C. Huber, C. Loquai, Ö. Türeci, *Nature* **2017**, *547*, 222; c) N. Hilf, S. Kuttruff-Coqui, K. Frenzel, V. Bukur, S. Stevanović, C. Gouttefangeas, M. Platten, G. Tabatabai, V. Dutoit, S. H. van der Burg, P. thor Straten, F. Martínez-Ricarte, B. Ponsati, H. Okada, U. Lassen, A. Admon, C. H. Ottensmeier, A. Ulges, S. Kreiter, A. von Deimling, M. Skardelly, D. Migliorini, J. R. Kroep, M. Idorn, J. Rodon, J. Piró, H. S. Poulsen, B. Shraibman, K. McCann, R. Mendrzyk, M. Löwer, M. Stieglbauer, C. M. Britten, D. Capper, M. J. P. Welters, J. Sahuquillo, K. Kiesel, E. Derhovanessian, E. Rusch, L. Bunse, C. Song, S. Heesch, C. Wagner, A. Kemmer-Brück, J. Ludwig, J. C. Castle, O. Schoor, A. D. Tadmor, E. Green, J. Fritsche, M. Meyer, N. Pawlowski, S. Dorner, F. Hoffgaard, B. Rössler, D. Maurer, T. Weinschenk, C. Reinhardt, C. Huber, H.-G. Rammensee, H. Singh-Jasuja, U. Sahin, P.-Y. Dietrich, W. Wick, *Nature* **2019**, *565*, 240; d) D. B. Keskin, A. J. Anandappa, J. Sun, I. Tirosh, N. D. Mathewson, S. Li, G. Oliveira, A. Giobbie-Hurder, K. Felt, E. Gjini, S. A. Shukla, Z. Hu, L. Li, P. M. Le, R. L. Allesøe, A. R. Richman, M. S. Kowalczyk, S. Abdelrahman, J. E. Geduldig, S. Charbonneau, K. Pelton, J. B. Iorgulescu, L. Elagina, W. Zhang, O. Olive, C. McCluskey, L. R. Olsen, J. Stevens, W. J. Lane, A. M. Salazar, H. Daley, P. Y. Wen, E. A. Chiocca, M. Harden, N. J. Lennon, S. Gabriel, G. Getz, E. S. Lander, A. Regev, J. Ritz, D. Neuberg, S. J. Rodig, K. L. Ligon, M. L. Suvà, K. W. Wucherpfennig, N. Hacohen, E. F. Fritsch, K. J. Livak, P. A. Ott, C. J. Wu, D. A. Reardon, *Nature* **2019**, *565*, 234.

[5] a) H. Liu, K. D. Moynihan, Y. Zheng, G. L. Szeto, A. V. Li, B. Huang, D. S. Van Egeren, C. Park, D. J. Irvine, *Nature* **2014**, *507*, 519; b) G. Zhu, G. M. Lynn, O. Jacobson, K. Chen, Y. Liu, H. Zhang, Y. Ma, F. Zhang, R. Tian, Q. Ni, S. Cheng, Z. Wang, N. Lu, B. C. Yung, Z. Wang, L. Lang, X. Fu, A. Jin, I. D. Weiss, H. Vishwasrao, G. Niu, H. Shroff, D. M. Klinman, R. A. Seder, X. Chen, *Nat. Commun.* **2017**, *8*, 1954.

[6] J. Nam, S. Son, K. S. Park, W. Zou, L. D. Shea, J. J. Moon, *Nat. Rev. Mater.* **2019**, *4*, 398.

[7] a) G. M. Lynn, R. Laga, P. A. Darrah, A. S. Ishizuka, A. J. Balaci, A. E. Dulcey, M. Pechar, R. Pola, M. Y. Gerner, A. Yamamoto, C. R. Buechler, K. M. Quinn, M. G. Smelkinson, O. Vanek, R. Cawood, T. Hills, O. Vasalatiy, K. Kastenmüller, J. R. Francica, L. Stutts, J. K. Tom, K. A. Ryu, A. P. Esser-Kahn, T. Etrych, K. D. Fisher, L. W. Seymour, R. A. Seder, *Nat. Biotechnol.* **2015**, *33*, 1201; b) A.de Titta, M. Ballester, Z. Julier, C. Nembrini, L. Jeanbart, A. J. van der Vlies, M. A. Swartz, J. A. Hubbell, *Proc. Natl. Acad. Sci. USA* **2013**, *110*, 19902; c) J. J. Moon, H. Suh, A. Bershteyn, M. T. Stephan, H. Liu, B. Huang, M. Sohail, S. Luo, S. H. Um, H. Khant, J. T. Goodwin, J. Ramos, W. Chiu, D. J. Irvine, *Nat. Mater.* **2011**, *10*, 243.

[8] a) L. M. Kranz, M. Diken, H. Haas, S. Kreiter, C. Loquai, K. C. Reuter, M. Meng, D. Fritz, F. Vascotto, H. Hefesha, C. Grunwitz, M. Vormehr, Y. Hüsemann, A. Selmi, A. N. Kuhn, J. Buck, E. Derhovanessian, R. Rae, S. Attig, J. Diekmann, R. A. Jabulowsky, S. Heesch, J. Hassel, P. Langguth, S. Grabbe, C. Huber, Ö. Türeci, U. Sahin, *Nature* **2016**, *534*, 396; b) R. Kuai, L. J. Ochyl, K. S. Bahjat, A. Schwendeman, J. J. Moon, *Nat. Mater.* **2017**, *16*, 489; c) G. M. Lynn, C. Sedlik, F. Baharom, Y. Zhu, R. A. Ramirez-Valdez, V. L. Coble, K. Tobin, S. R. Nichols, Y. Itzkowitz, N. Zaidi, J. M. Gammon, N. J. Blobel, J. Denizeau, P. de la Rochere, B. J. Francica, B. Decker, M. Maciejewski, J. Cheung, H. Yamane, M. G. Smelkinson, J. R. Francica, R. Laga, J. D. Bernstock, L. W. Seymour, C. G. Drake, C. M. Jewell, O. Lantz, E. Piaggio, A. S. Ishizuka, R. A. Seder, *Nat. Biotechnol.* **2020**, *38*, 320; d) C. Xu, J. Nam, H. Hong, Y. Xu, J. J. Moon, *ACS Nano* **2019**, *13*, 12148.

[9] U. Sahin, Ö. Türeci, *Science* **2018**, *359*, 1355.

[10] a) J. M. Blander, R. Medzhitov, *Nat. Immunol.* **2006**, *7*, 1029; b) S. Nierkens, M. H. den Brok, R. P. M. Sutmuller, O. M. Grauer, E. Bennink, M. E. Morgan, C. G. Figdor, T. J. M. Ruers, G. J. Adema, *Cancer Res.* **2008**, *68*, 5390.

[11] a) E. R. Kandimalla, L. Bhagat, D. Yu, Y. Cong, J. Tang, S. Agrawal, *Bioconjugate Chem.* **2002**, *13*, 966; b) M. R. Putta, F.-G. Zhu, D. Wang, L. Bhagat, M. Dai, E. R. Kandimalla, S. Agrawal, *Bioconjugate Chem.* **2010**, *21*, 39.

[12] S. M. Moghimi, P. Symonds, J. C. Murray, A. C. Hunter, G. Debska, A. Szewczyk, *Mol. Ther.* **2005**, *11*, 990.
[13] S. L. Snyder, P. Z. Sobocinski, *Anal. Biochem.* **1975**, *64*, 284.
[14] a) H. Petersen, P. M. Fechner, A. L. Martin, K. Kunath, S. Stolnik, C. J. Roberts, D. Fischer, M. C. Davies, T. Kissel, *Bioconjugate Chem.* **2002**, *13*, 845; b) M. Ogris, G. Walker, T. Blessing, R. Kircheis, M. Wolschek, E. Wagner, *J. Controlled Release* **2003**, *91*, 173; c) M. Ogris, S. Brunner, S. Schüller, R. Kircheis, E. Wagner, *Gene Ther.* **1999**, *6*, 595; d) M. Kursa, G. F. Walker, V. Roessler, M. Ogris, W. Roedl, R. Kircheis, E. Wagner, *Bioconjugate Chem.* **2003**, *14*, 222.
[15] a) J. S. Suk, Q. Xu, N. Kim, J. Hanes, L. M. Ensign, *Adv. Drug Delivery Rev.* **2016**, *99*, 28; b) J. Nam, N. Won, J. Bang, H. Jin, J. Park, S. Jung, S. Jung, Y. Park, S. Kim, *Adv. Drug Delivery Rev.* **2013**, *65*, 622.
[16] F. Veglia, V. A. Tyurin, D. Mohammadyani, M. Blasi, E. K. Duperret, L. Donthireddy, A. Hashimoto, A. Kapralov, A. Amoscato, R. Angelini, S. Patel, K. Alicea-Torres, D. Weiner, M. E. Murphy, J. Klein-Seetharaman, E. Celis, V. E. Kagan, D. I. Gabrilovich, *Nat. Commun.* **2017**, *8*, 2122.
[17] L. Jeanbart, M. Ballester, A. de Titta, P. Corthésy, P. Romero, J. A. Hubbell, M. A. Swartz, *Cancer Immunol. Res.* **2014**, *2*, 436.
[18] a) S. Aras, M. R. Zaidi, *Br. J. Cancer* **2017**, *117*, 1583; b) J. M. Jaynes, R. Sable, M. Ronzetti, W. Bautista, Z. Knotts, A. Abisoye-Ogunniyan, D. Li, R. Calvo, M. Dashnyam, A. Singh, T. Guerin, J. White, S. Ravichandran, P. Kumar, K. Talsania, V. Chen, A. Ghebremedhin, B. Karanam, A. Bin Salam, R. Amin, T. Odzorig, T. Aiken, V. Nguyen, Y. Bian, J. C. Zarif, A. E. de Groot, M. Mehta, L. Fan, X. Hu, A. Simeonov, N. Pate, M. Abu-Asab, M. Ferrer, N. Southall, C.-Y. Ock, Y. Zhao, H. Lopez, S. Kozlov, N. de Val, C. C. Yates, B. Baljinnyam, J. Marugan, U. Rudloff, *Sci. Transl. Med.* **2020**, *12*, eaax6337; c) T. M. Raimondo, D. J. Mooney, *Proc. Natl. Acad. Sci. USA* **2018**, *115*, 10648; d) Q. Li, A. Shen, Z. Wang, *RSC Adv.* **2020**, *10*, 16537.
[19] a) A. Marabelle, L. Tselikas, T. de Baere, R. Houot, *Ann. Oncol.* **2017**, *28*, xii33; b) M. A. Aznar, N. Tinari, A. J. Rullán, A. R. Sánchez-Paulete, M. E. Rodriguez-Ruiz, I. Melero, *J. Immunol.* **2017**, *198*, 31.
[20] D. S. Chen, I. Mellman, *Immunity* **2013**, *39*, 1.
[21] a) O. Boussif, F. Lezoualc'h, M. A. Zanta, M. D. Mergny, D. Scherman, B. Demeneix, J. P. Behr, *Proc. Natl. Acad. Sci. USA* **1995**, *92*, 7297; b) U. Lungwitz, M. Breunig, T. Blunk, A. Göpferich, *Eur. J. Pharm. Biopharm.* **2005**, *60*, 247.
[22] a) C. Shen, J. Li, Y. Zhang, Y. Li, G. Shen, J. Zhu, J. Tao, *Int. J. Nanomed.* **2017**, *12*, 5443; b) K. Regnström, E. G. E. Ragnarsson, M. Köping-Höggård, E. Torstensson, H. Nyblom, P. Artursson, *Gene Ther.* **2003**, *10*, 1575.
[23] a) F. Wegmann, K. H. Gartlan, A. M. Harandi, S. A. Brinckmann, M. Coccia, W. R. Hillson, W. L. Kok, S. Cole, L.-P. Ho, T. Lambe, M. Puthia, C. Svanborg, E. M. Scherer, G. Krashias, A. Williams, J. N. Blattman, P. D. Greenberg, R. A. Flavell, A. E. Moghaddam, N. C. Sheppard, Q. J. Sattentau, *Nat. Biotechnol.* **2012**, *30*, 883; b) N. C. Sheppard, S. A. Brinckmann, K. H. Gartlan, M. Puthia, C. Svanborg, G. Krashias, S. C. Eisenbarth, R. A. Flavell, Q. J. Sattentau, F. Wegmann, *Int. Immunol.* **2014**, *26*, 531; c) E. V. Grant, M. Thomas, J. Fortune, A. M. Klibanov, N. L. Letvin, *Eur. J. Immunol.* **2012**, *42*, 2937; d) M. Bivas-Benita, L. Bar, G. O. Gillard, D. R. Kaufman, N. L. Simmons, A.-H. Hovav, N. L. Letvin, *J. Virol.* **2010**, *84*, 5764; e) M. Rodrigo Garzón, P. Berraondo, J. Crettaz, L. Ochoa, M. Vera, J. J. Lasarte, A. Vales, N. Van Rooijen, J. Ruiz, J. Prieto, J. Zulueta, G. González-Aseguinolaza, *Vaccine* **2005**, *23*, 1384; f) B.-S. Shim, S.-M. Park, J.-S. Quan, D. Jere, H. Chu, M. K. Song, D. W. Kim, Y.-S. Jang, M.-S. Yang, S. H. Han, Y.-H. Park, C.-S. Cho, C.-H. Yun, *BMC Immunol.* **2010**, *11*, 65.
[24] a) Y.-F. Ma, Y.-W. Yang, *Eur. J. Pharm. Sci.* **2010**, *40*, 75; b) Z. Sun, B. Liu, X. Ruan, Q. Liu, *Mol. Med. Rep.* **2014**, *10*, 2657.
[25] a) R. N. Palumbo, X. Zhong, C. Wang, *J. Controlled Release* **2012**, *157*, 86; b) R. M. Steinman, M. C. Nussenzweig, *Proc. Natl. Acad. Sci. USA* **2002**, *99*, 351.
[26] H. Petersen, P. M. Fechner, D. Fischer, T. Kissel, *Macromolecules* **2002**, *35*, 6867.
[27] M. Jäger, S. Schubert, S. Ochrimenko, D. Fischer, U. S. Schubert, *Chem. Soc. Rev.* **2012**, *41*, 4755.
[28] N. P. Gabrielson, D. W. Pack, *Biomacromolecules* **2006**, *7*, 2427.
[29] C. C. Norbury, *Immunology* **2006**, *117*, 443.
[30] a) T. Kawai, S. Akira, *Immunity* **2011**, *34*, 637; b) L. A. J. O'Neill, D. Golenbock, A. G. Bowie, *Nat. Rev. Immunol.* **2013**, *13*, 453.
[31] a) S. Yang, S. May, *J. Chem. Phys.* **2008**, *129*, 185105; b) A. Akinc, M. Thomas, A. M. Klibanov, R. Langer, *The J. Gene Med.* **2005**, *7*, 657.
[32] O. P. Joffre, E. Segura, A. Savina, S. Amigorena, *Nat. Rev. Immunol.* **2012**, *12*, 557.
[33] P. Nair-Gupta, A. Baccarini, N. Tung, F. Seyffer, O. Florey, Y. Huang, M. Banerjee, M. Overholtzer, P. A. Roche, R. Tampé, B. D. Brown, D. Amsen, S. W. Whiteheart, J. M. Blander, *Cell* **2014**, *158*, 506.
[34] S. Nierkens, M. H. den Brok, T. Roelofsen, J. A. L. Wagenaars, C. G. Figdor, T. J. Ruers, G. J. Adema, *PLoS One* **2009**, *4*, 8368.
[35] J. Nam, S. Son, J. J. Moon, *Cell Mol. Bioeng.* **2017**, *10*, 341.
[36] M. B. Lutz, N. Kukutsch, A. L. J. Ogilvie, S. Rößner, F. Koch, N. Romani, G. Schuler, *J. Immunol. Methods* **1999**, *223*, 77.

Build the *best* panels

with our brightest and biggest range of dyes.

StarBright Dyes for flow cytometry

StarBright Dyes are unique fluorescent nanoparticles conjugated to Bio-Rad's highly validated immunology antibodies. Developed specifically for flow cytometry, StarBright Dyes have narrow excitation and emission spectra and give you exceptional brightness without the need for a special buffer. StarBright Dyes are currently available for use with violet, blue, and ultraviolet lasers.

Explore StarBright Dyes at bio-rad-antibodies.com/StarBrightDyes

#ScienceForward

BIO-RAD